

平成 26 年度 博士学位論文

Study of Terahertz Sensing Applications
using Metal Structures

(金属構造体を用いたテラヘルツ
センシング応用に関する研究)

名古屋大学大学院工学研究科

電子情報システム専攻

管 宇

(GUAN Yu)

Table of Contents

Chapter 1 Introduction.....	1
1.1 Research background and motivation	1
1.1.1 Terahertz regime	1
1.1.2 THz applications and motivation of this work	1
1.2 Compositions of the doctoral thesis.....	4
Chapter 2 Experimental systems for terahertz wave generation and detection.....	10
2.1 Description of terahertz time-domain spectroscopy (THz-TDS)	10
2.1.1 Development of THz-TDS	10
2.1.1 Photoconductive generation and detection of THz pulse	12
2.1.3 THz-TDS with transmission geometry.....	17
2.1.4 THz-TDS with reflection geometry.....	19
2.2 Study of cross-polarization effect of parabolic mirrors applied in the THz setup	23
2.2.1 Motivation and research approaches	23
2.2.2 Analytical simulations and measurements in real-field.....	24
2.2.3 Conclusion.....	37
2.3 Summary.....	38
Chapter 3 Terahertz component analysis using metal mesh structure.....	40
3.1 Metal mesh structure	40
3.2 Transmission properties of metal mesh	41
3.2.1 Transmittance enhancement and abnormal decline	41
3.2.2 Dependence between dip and incident angle of THz wave.....	43
3.2.3 Dependence between dip and polarization direction of THz wave	44
3.3 Several theories for transmission spectrum of metal mesh	45
3.3.1 Surface plasmon polariton	45
3.3.2 Diffracted evanescent wave model.....	48
3.3.3 Diffracted interference of adjacent square opening in (1, 1) direction.....	51
3.4 Measurements of the human skin samples using metal mesh sensor.....	53
3.4.1 Introduction of sample and motivation.....	54
3.4.2 Sample preparation	56
3.4.3 Lipid substance sensing measurements	59
3.4.4 Protein denaturation sensing measurements.....	63
3.5 Summary.....	67

Table of Contents

Chapter 4 Identification over obstacles using terahertz tags/barcodes.....	71
4.1 Introduction of background and motivation	71
4.2 Surface metal antenna array	72
4.2.1 Definition.....	72
4.2.2 Design and simulation results of “clock” shaped mode	74
4.2.3 Experimental measurements of “clock” shaped mode	80
4.2.4 Discussion.....	85
4.3 Concealed THz barcode identification system using THz-TDS.....	86
4.3.1 Sample preparation	88
4.3.2 Experimental setups and conditions	89
4.3.3 Measurements of single-side printed barcodes.....	90
4.3.4 Measurements of double-side printed barcodes	92
4.3.5 Theoretic analysis of double-side printed barcode system.....	96
4.3.6 Discussion.....	102
4.4 Summary.....	103
Chapter 5 Terahertz interferometry by applying metal meshes.....	109
5.1 Theoretical Background	109
5.1.1 Multiple beam interference.....	109
5.1.2 Sandwich structure of metal meshes	113
5.2 Metal mesh interferometer measurements using THz-TDS	115
5.3 Summary.....	120
Chapter 6 Summary	121
Presentation and Publication	123
Acknowledgment.....	125

Chapter 1 Introduction

1.1 Research background and motivation

1.1.1 Terahertz regime

The Terahertz Regime is conventionally regarded as a narrow band of spectrum in the part of far-infrared (FIR) region sandwiched between the microwaves and infrared waves. Although the strict definition of upper and lower frequency limits of THz range in electromagnetic spectrum is not unified and varied by a little bit from different research groups or people with different academic background, it is usually considered lying in the gap from 0.1 THz to 10 THz (wavelength between 30 μm and 3 mm), bridging the classic Electronics and Optics [1].

Reviewing back into the history of mankind exploring the infrared range, it is not until the mid of last century by the development of new spectroscopic techniques, particularly after the introduction of Fourier-transform spectroscopy that the research related to far-infrared range began to spread. Since the introduction of Terahertz Time-domain Spectroscopy (THz-TDS) with steady performance of acquiring THz pulses' amplitude and phase information in late 1980's, grew from work at AT&T Bell Labs and the IBM T. J. Watson Research Center [2-4], and the establishment of injection-seeded THz-wave parametric generator (is-TPG) representing the broadband tunable source using the nonlinear optical crystal [5], the study regarding THz waves have been found an remarkably increasing in the number of applications in various fields of research [6-10]. Scientific community has accepted it as a latest frontier of the exploring in FIR region with many attractive advantages.

1.1.2 THz applications and motivation of this work

Compared to the visible light, the ability of THz wave to penetrate many packaging materials, such as paper and cardboard, semiconductors, textiles, plastics, wood,

ceramics, dried or frozen materials, and so on, allows the implement of the applications of nondestructive and noninvasive inspections over the soft materials of such kind [11-18]; additionally, the moderate transmittance of THz radiation makes it easier to visualize the 3D internal structure inside the objects made by soft materials using THz computed tomography (CT) technique, which is beyond the capability of X-Ray CT [19-21]. Although the sensitive measurements of 3D images can be expected, we must point out that there are still some issues needed to be well addressed due to the factor that it is easier for THz radiation to express scattering and diffraction compared to the X-ray. Compared to the millimeter wave on the other side of spectrum which is also able to “see” through packaging obstacles, imaging measurements utilizing THz radiation can have favorable spatial resolution due to the order of its wavelength (around a few hundred micrometers). Thus, THz imaging applications have been greatly expected. Furthermore, THz radiation is non-ionizing and therefore it is considered to be not dangerous for human beings. The frequency of the intermolecular vibration of organic/bio-molecule or the hydration-induced absorption [22-24], rotational excitation of gas molecule [25-26], and lattice vibration/ plasma oscillation [27-28] are also located in terahertz region. These advantages make THz sensing techniques great potential for the medical and security relevant imaging. An example of this kind of imaging technique is shown in Figure 1-1.

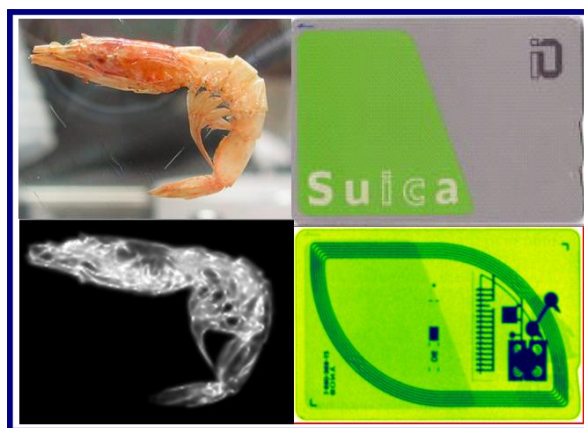


Figure 1-1. 2D THz imaging to acquire the inside information of objects

On the other hand, challenges still remain setting barriers for applications of THz technique, such as that the direct measurements of sample can't provide enough sensitivity in some situations. A good example is the stationary ink measurements as shown in Figure 1-2 [29].

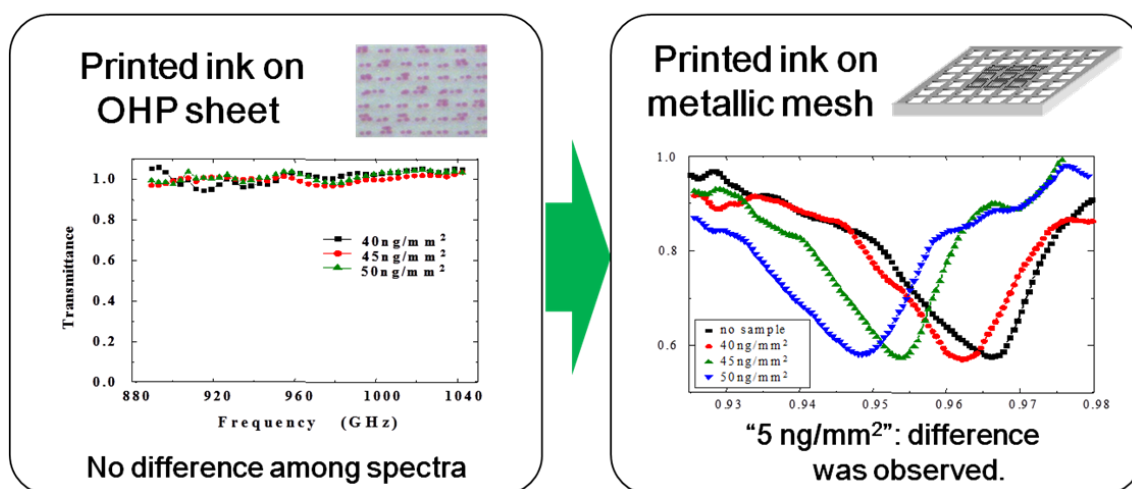


Figure 1-2. An example of lack of sensitivity of direct THz spectroscopy

A commercial inkjet print was applied to quantitatively control the amount of ink printed onto the substrate. A 0.1-mm-thick polyethylene terephthalate (PET) film was applied as the substrate. Samples of identical substrate coated by ink with three different densities were measured directly using THz radiation. No difference can be observed in the transmission spectra. Thus, the sensitivity of the direct measurements wasn't enough. However, by printing the ink onto a metal structure usually referred as metallic mesh, the THz transmission spectra clearly show the difference of the samples. The image with dimensions of such metal structure is presented in Figure 1-3. It is a thin film of metal embedded with periodic square openings.

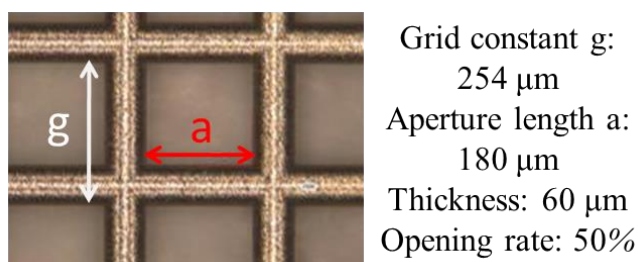


Figure 1-3. Image of the metal mesh applied for the ink measurement

With its unique transmission characteristics in THz region, measurements applying metallic mesh greatly improve the sensitivity for THz sensing applications. Such transmission characteristics of metal meshes, which have been investigated since the 1960s, are similar to those of far-infrared band-pass filters [30-31]. Metal mesh transmission properties depend on geometric parameters, e. g. the shape and size of the

openings and the grid constant [32]. Although the mechanism of the spectral characteristic remained unclear, the metal mesh has been applied as filter in many research fields [33-41]. Recently, rapid improvements in processing techniques have made it easy to inexpensively manufacture such filters with arbitrary properties [42-43]. In 1998, Ebbesen et al. reported the optical transmission anomaly of a thin metal layer covered by a periodic array of subwavelength cylindrical holes [44]. Because of this anomaly, a far higher ratio of light relative to the opening ratio could pass through the periodic subwavelength hole arrays. At the time, it was thought to occur due to the excitation of surface plasmons (SPs). However, in 2004, Thio and Lezec proposed a diffracted evanescent wave model to explain this anomaly successfully. In addition, Sharrazin claimed that the transmission behavior corresponding to Fano's profile correlated with a resonant response of the eigenmodes coupled with non-homogeneous diffraction orders [45-46]. Our laboratory has previously reported that the "dip" in the metal mesh transmission spectrum, which appears in a lower frequency region than the lowest orders of the SPP (Surface Plasmon Polariton) and Rayleigh anomaly modes, occurs due to the interference between diffraction orders from adjacent diagonal apertures [47].

Inspired by the measurements shown in Figure 1-2, this work is focusing on the development of THz sensing applications using different metal structures.

1.2 Compositions of the doctoral thesis

This thesis contains six chapters. The simple description is outlined as follows:

Chapter 1 discusses the background and motivation of my research.

Chapter 2 introduces the principle of experimental setup that we applied for the measurements; Study of cross-polarization effect of parabolic mirrors is also presented in this chapter.

Chapter 3 demonstrates the application of Terahertz component analysis using metal mesh structure by conducting the measurements of human skin.

Chapter 4 firstly demonstrates experimental measurements along with simulation results of a "clock" shaped metal structure for the application of THz identification. Next, a fully printable barcode structure is proposed for

achieving low-cost THz identification over obstacles (EMS envelope) using THz-TDS. Experimental measurements and theoretical analysis are presented and discussed to prove its validity.

Chapter 5 includes the measurements of terahertz interferometry by using metal meshes.

Chapter 6 is the summary of this thesis.

Reference

- [1] Kai-Erik Peiponen, J. Axel Zeitler, Makoto Kuwata-Gonokami, “Terahertz spectroscopy and imaging”, *Springer Series in Optical Sciences* 171, 2013
- [2] Auston, D. H., Cheung, K. P., Valdmanis, J. A. & Kleinman, D. A. Cherenkov radiation from femtosecond optical pulses in electro-optic media. *Phys. Rev. Lett.* 53, pp. 1555–1558 (1984).
- [3] Ch. Fattinger and D. Grischkowsky, “Point source terahertz optics.” *Appl. Phys. Lett.* 53, pp. 1480–1482 (1988).
- [4] P. R. Smith, D. H. Auston, M. C. Nuss, “Subpicosecond photoconducting dipole antennas”, *IEEE J. Quantum Elec.* 24, 255-260, (1989)
- [5] K. Kawase, H. Minamide, K. Imai, J. Shikata, and H. Ito, *Applied Physic Letters*, 80, 195 (2002).
- [6] D. Mittleman, R. Jacobsen, and M. C. Nuss, “T-Ray Imaging”, *J. Selected Topics Quantum Electron.* Vol. 2, No.3 pp. 679-692 (1996)
- [7] P. H. Siegel, “Terahertz Technology”, *IEEE Trans. Microwave Theory Tech.*, Vol. 50, No.3 pp. 910-928 (2002)
- [8] B. S. Ferguson, S. H. Wang, D. Gray, D. Abbot, and X.-C. Zhang, “T-ray computed tomography”, *Opt. Lett.* Vol. 27, Issue 15, pp. 1312-1314 (2002)
- [9] T. Kiwa, M. Tonouchi, M. Yamashita, and K. Kawase, “Laser terahertz-emission microscope for inspecting electrical faults in integrated circuits”, *Optics Lett.* Vol. 28, No. 21, pp. 2058-2063 (2003)
- [10] H. Hirori, K. Yamashita, M. Nagai, and K. Tanaka, “Attenuated Total Reflection Spectroscopy in Time Domain Using Terahertz Coherent Pulses”, *Jpn. J. Appl. Phys.* Vol. 43, L1287 (2004)
- [11] B. Hu, M. C. Nuss, “Imaging with terahertz waves”, *Opt. Lett.* Vol.20, Issue 16, pp. 1716-1718 (1995)
- [12] D. Mittleman, M. Gupta, R. Neelamani, R. Baraniuk, J. Rudd, M. Koch, “Recent advances in terahertz imaging”, *Appl. Phys. B Laser Opt.* 68, pp. 1085-1094 (1999)
- [13] R. M. Woodward, B. E. Cole, V. P. Wallace, R. J. Pye, D. D. Arnone, E. H. Linfield, and M. Pepper, “Terahertz pulse imaging in reflection geometry of human skin cancer and skin tissue”, *Phys. Med. Biol.* Vol. 47, No. 21, pp. 3853-3863 (2002)
- [14] K. Kawase, Y. Ogawa, Y. Watanabe, H. Inoue, “Non-destructive terahertz imaging

- of illicit drugs using spectral fingerprints”, *Opt. Express*, Vol. 11, Issue 20, pp. 2549-2554 (2003)
- [15] A. Dobroiu, M. Yamashita, Y. Ohshima, C. Otani, K. Kawase, “Terahertz imaging system based on a backward-wave oscillator”, *Appl. Opt.*, Vol. 43, Issue 30, pp. 5637-5646 (2004)
- [16] H. Zhong, J. Xu, X. Xie, T. Yuan, R. Reightler, E. Madaras, and X.-C. Zhang, “Nondestructive defect identification with terahertz time-of-flight tomography”, *IEEE Sensors J.*, Vol. 5, Issue 2, pp. 203-208 (2005)
- [17] Y. C. Shen and P. F. Taday, “Development and Application of Terahertz pulsed Imaging for Nondestructive Inspection of Pharmaceutical Tablet”, *IEEE J. Sel. Top. Quantum Electron.* Vol. 14 Issue 2, pp. 407-415 (2008)
- [18] K. Fukunaga, N. Sekine, I. Hosako, N. Oda, H. Yoneyama, and T. Sudoh, “Real-time terahertz imaging for art conservation science”, *J. Euro. Opt. Soc. – Rapid. Pub.* Vol. 3, 08027 (2008)
- [19] B. Ferguson, S. Wang, D. Gray, D. Abbot, X. -C. Zhang, “T-ray computed tomography”, *Opt. Lett.* 27, 1312 (2002)
- [20] B. Ferguson, S. Wang, D. Gray, D. Abbott and X.-C. Zhang, “Towards functional 3D T-ray imaging”, *Phys. Med. Biol.* Vol. 47, No. 21, pp. 3735-3742 (2002)
- [21] S. Wang, B. Ferguson, D. Abbott, X.-C. Zhang, “T-ray imaging and tomography”, *Journal of Biological Physics*, Vol. 29, Issue 2-3, pp. 247-256 (2003)
- [22] A. G. Markelz, A. Roitberg, and E. J. Heilweil, “Pulsed terahertz spectroscopy of DNA, bovine serum albumin and collagen between 0.1 and 2.0 THz”, *Chem. Phys. Lett.* Vol. 320, Issue 1-2, pp. 42-48 (2000)
- [23] C. F. Zhang, E. Tarhan, A. K. Ramdas, A. M. Weiner, and S. M. Durbin, “Broadened Far-Infrared Absorption Spectra for Hydrated and Dehydrated Myoglobin”, *J. Phys. Chem. B* Vol. 108, pp. 10077-10082 (2004)
- [24] C. F. Zhang, and S. M. Durbin, “Hydration-Induced Far-Infrared Absorption Increase in myoglobin”, *J. Phys. Chem. B* Vol. 110, pp. 23607-23613 (2006)
- [25] H. Harde, S. Keiding, and D. Grischkowsky, “THz commensurate echoes: Periodic rephrasing of molecular transitions in free-induction decay”, *Phys. Rev. Lett.* Vol. 66, 1834 (1991)
- [26] R. H. Jacobsen, D. M. Mittleman, and M. C. Nuss, “Chemical recognition of gases

- and gas mixtures with terahertz waves”, *Opt. Lett.* 21, 2011 (1996)
- [27] T. Dekorsy, H. Auer, C. Waschke, H. J. Bakker, H. G. Roskos, and H. Kurz, “Emission of Submillimeter Electromagnetic Waves by Coherent Phonons”, *Phys. Rev. Lett.* 74, 738 (1995)
- [28] M. Tani, R. Fukasawa, H. Abe, S. Matsuura, K. Sakai, and S. Nakashima, “Terahertz radiation from coherent phonons excited in semiconductors”, *J. Appl. Phys.* 83, 2473 (1998)
- [29] 加藤英志, “テラヘルツ波による金属二次元開口アレイを用いたセンシングに関する研究”, 博士学位論文, pp. 59-69, 名古屋大学工学研究科 (2009)
- [30] R. Ulrich, “Far-Infrared Properties of Metallic Mesh and its Complementary Structure”, *Infrared Phys.* 7, 37 (1967).
- [31] K. Sakai, T. Fukui, Y. Tsunawaki, H. Yoshinaga, “Metallic Mesh Bandpass Filters and Fabry-Perot Interferometer for the Far Infrared”, *Jpn. J. Appl. Phys.* 8, 1046-1055 (1969).
- [32] K. Sakai, T. Yoshida, “Single mesh narrow bandpass filters from the infrared to the submillimeter region”, *Infrared Phys.* 18, 137-140 (1978).
- [33] K. F. Renk and L. Genzel, “Interference Filters and Fabry-Perot Interometers for the Far Infrared”, *Appl. Opt.* Vol. 1, Issue 5, pp. 643-648 (1962)
- [34] R. Ulrich, K. F. Renk, and L. Genzel, “Tunable Submillimeter Interferometers of the Fabry-Perot Type”, *IEEE Trans. Microwave Theory Tech.* Vol. 11, Issue 5, pp. 363-371 (1963)
- [35] R. D. Rawcliffe, and C. M. Randall, *Appl. Opt.* “Metal Mesh Interference Filters for the Far Infrared”, Vol. 6, Issue. 8, pp. 1353-1358 (1967)
- [36] D. A. Weitz, W. J. Skocpol, and M. Tinkham, “Capacitive-mesh output couplers for optically pumped far-infrared lasers”, *Opt. Lett.* Vol. 3, Issue 1, pp. 13-15 (1978)
- [37] V. P. Tomaselli, D. C. Edewaard, P. Gillan, and K. D. Moller, “Far-infrared bandpass filters from cross-shaped girds”, *Appl. Opt.* Vol. 20, Issue 8, pp. 1361-1366 (1981)
- [38] W. G. Chambers, T. J. Parker, and A. E. Costley: *Infrared and Millimeter Waves* 16, K. J. Button ed., Academic Press, Orlando, 77 (1986)
- [39] K. Sakai and L. Genzel, *Review of Infrared and Millimeter Waves*, K. J. Button ed., Plenum Press, New York, 155 (1983)

- [40] J. C. Vardaxoglou: Frequency Selective Surfaces: Analysis and Design: Research Studies Press (1997)
- [41] B. A. Munk, Frequency Selective Surface: Theory and Design, Wiley Interscience (2000)
- [42] F. Miyamaru, M. Tanaka, M. Hangyo, “Effect of hole diameter on terahertz surface-wave excitation in metal-hole arrays”, *Phys. Rev. B* 74, 153416 (2006).
- [43] S. A. Kuznetsov, V. V. Kubarev, P. V. Kalinin, N. A. Vinokurov, *Conference Digest of the IRMMW-THz2007*, 303 (2007).
- [44] T. W. Ebbesen, H. J. Lezec, H. F. Ghaemi, T. Thio, P. A. Wolff, “Extraordinary optical transmission through subwavelength hole arrays”, *Nature* 391, 667-669 (1998).
- [45] H. J. Lezec, T. Thio, “Diffracted evanescent wave model for enhanced and suppressed optical transmission through subwavelength hole arrays”, *Opt. Exp.* 12, 3629-3651 (2004).
- [46] M. Sarrazin, J. P. Vigneron, J-M. Vigoureux, “Role of Wood anomalies in optical properties of thin metallic films with a bidimensional array of subwavelength holes”, *Phys. Rev. B* 67, 085414 (2003).
- [47] S. Yoshida, K. Suizu, E. Kato, Y. Nakagomi, Y. Ogawa, K. Kawase, “A high-sensitivity terahertz sensing method using a metallic mesh with unique transmission properties”, *J. Molecular Spectroscopy*, 256, 146-151 (2009).

Chapter 2 Experimental systems for terahertz wave generation and detection

Firstly, the demonstration of “terahertz time-domain spectroscopy”, shorten for “THz-TDS”, as the experimental setup is presented in this chapter, which was applied for the measurements discussed in later chapters. Next, I am going to explain the principle of “THz-TDS” which uses photoconductive antenna (PC antenna) for emission and detection of the pulsed THz radiation. At last, the study of the cross-polarization effect of parabolic mirrors is included in this chapter. As the parabolic mirror is a widely used element in THz experimental setup, author wish this study presented in section 2 can provide an instructive guide for helping researchers improving the accuracy of the measurements related to polarization in THz region.

2.1 Description of terahertz time-domain spectroscopy (THz-TDS)

2.1.1 Development of THz-TDS

The terahertz spectral range is considered to be one of the least explored regions of the electromagnetic spectrum. Since the latter half of the last century, many technologies have been developed to cover the study of terahertz regime. A technology known as Fourier-Transform IR-spectroscopy [1] has been widely used to measure the optical parameters of liquids, solids and gases above approximately 3 THz. However, it is difficult to apply such spectroscopy in the lower THz region, which is more commonly studied at the present (a few hundred gigahertzes to 3 terahertz as mentioned in Chapter 1) due to the weak intensity of common THz sources and the need of helium-cooled bolometer as the detector of the signal covered in thermal background radiation. An alternative method is the backward wave oscillator (BWO) [2] as a tunable

source. But the narrow band of the output spectra of the typical BWO system and the relatively short life time has limited its applications.

In 1989, Van Exter, Fattinger and Grischkowsky [3] presented a refined dipole photon antenna with a coplanar transmission line, introduced by Ketchenet et al. [4], to match the pulse generated in the gap with the propagating modes, and showed an electromagnetic wave system covering GHz and THz frequency range by applying off-axis parabolic mirrors and with lens for focusing light onto the photoconductive dipole. Furthermore, they characterized their electromagnetic wave system carefully and showed the system is practical for many spectroscopic applications, which is now known as “terahertz time-domain spectroscopy” (THz-TDS) [5, 6]. The basic optical design of a THz-TDS with photoconductive antenna (PC antenna) as emitter and detector is shown in Figure 2-1. The emitter for pumping THz signal is either mechanically or electrically chopped. Partially isolated pumping light (gating light), after adding well-distributed time delay, synchronously gate the detector. Thus, emitted THz pulse is sampled point by point as a function of the delay time. After applying Fourier transformation, the frequency spectrum of THz pulse can be acquired as shown in Figure 2-2. Although THz output emitted by the THz-TDS is restricted to several terahertz, with recent progress of short-pulse laser technology, it is possible to extend the spectral range to over 60 THz [7].

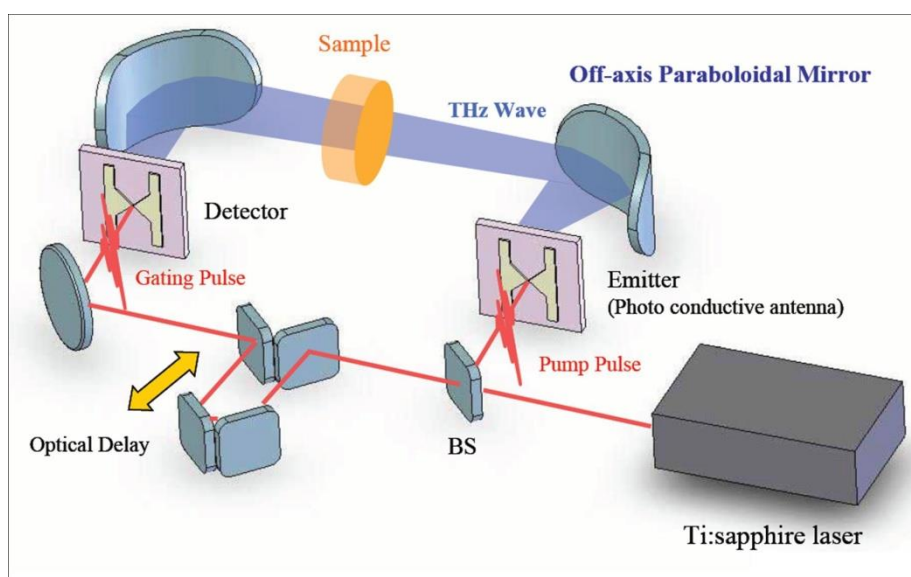


Figure 2-1. A typical optical design of THz-TDS

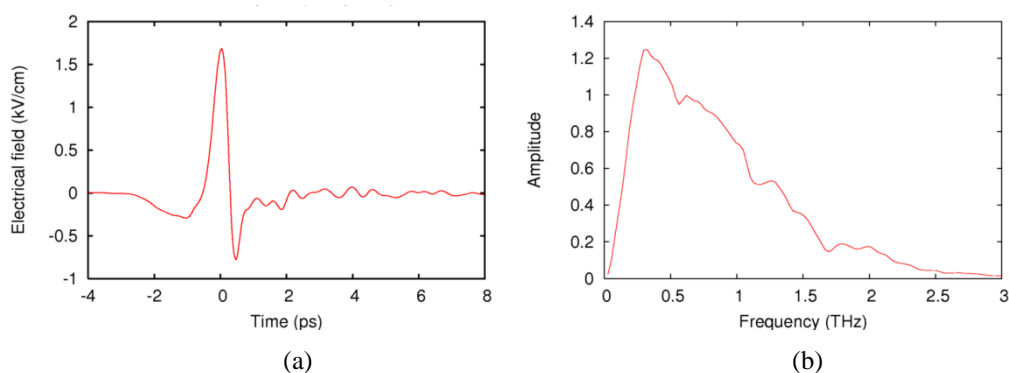


Figure 2-2. Typical THz pulse measured by THz-TDS: (a) Pulse in time domain spectra
(b) Pulse in frequency domain spectra

Compared with the Fourier transform spectroscopy (FTS) that detects the THz beam in power, THz-TDS achieves a direct measure of the amplitude and phase of the electric field of pulsed THz beam. Additionally, the second important advantage is that with a steady femtosecond laser applied as pump and probe light, the THz wave signal is observed with higher signal-to-noise ratio by THz-TDS than by FTS along with the fact that the former system uses a detector operating at room temperature [7].

2.1.1 Photoconductive generation and detection of THz pulse

In our experimental setup, two commercially available PC antennas were used to generate and detect the THz wave pulse respectively.

A PC antenna for THz wave generation and detection consists of a highly resistive direct semiconductor thin film with two electric contact pads. The film is made in most cases using an III-V compound semiconductor like GaAs. It is epitaxially grown on a semi-insulating GaAs substrate (SI-GaAs), which is also a highly resistive material. The important difference between the SI-GaAs substrate and the film is the relaxation time of the excited carriers. For example in a SI-substrate the carrier lifetime is about 500 ps, but in the film it is shorter than 1 ps [8]. Besides that, a high mobility and high threshold of breakdown voltage is also required.

Figure 2-3 shows the common pulsed THz wave generation from the PC antenna. When PC antenna works as a generator, the physical properties is described based on the Hertzian dipole shown in the right side of Figure 2-3. When the PC gap is irradiated by femtosecond laser pulses with its intensity larger than the energy bandgap of the

semiconductor, free electrons (holes) are excited in the conduction band. The carriers are obligatorily driven by and in phase of the bias field, then decay with a time constant determined by the carrier's lifetime afterwards, generating a pulsed photocurrent in the gap region of antenna. It can emit a sub-picosecond EM transient, i.e. THz wave signal because that the current modulation occurs in the sub-picosecond time frame.

For the mode of elementary Hertzian dipole antenna in free space, the radiated electric field $E(r, t)$ at a distance r (much larger than the wavelength of the radiation) and time t are described as [6]:

$$E(r, t) = \frac{l_e}{4\pi\epsilon_0 c^2 r} \frac{\partial J(t)}{\partial t} \sin \theta \propto \frac{\partial J(t)}{\partial t}, \quad (2-1)$$

where $J(t)$ is the current in the dipole, l_e is the effective length of the dipole, ϵ_0 is the dielectric constant of the vacuum, c is the velocity of light in the vacuum, and θ is an angle from the direction of the dipole.

Equation (2-1) describes a fact: the radiation amplitude is proportional to the time derivative of the transient photocurrent $\partial J(t) / \partial t$ and the effective antenna length l_e .

The photocurrent density is described as [6]:

$$j(t) \propto I(t) \otimes [n(t)q\nu(t)], \quad (2-2)$$

where \otimes presents the convolution product, $I(t)$ is the profile of optical intensity, and q , $n(t)$, and $\nu(t)$ are the charge, the density and the velocity of photo-carriers, respectively.

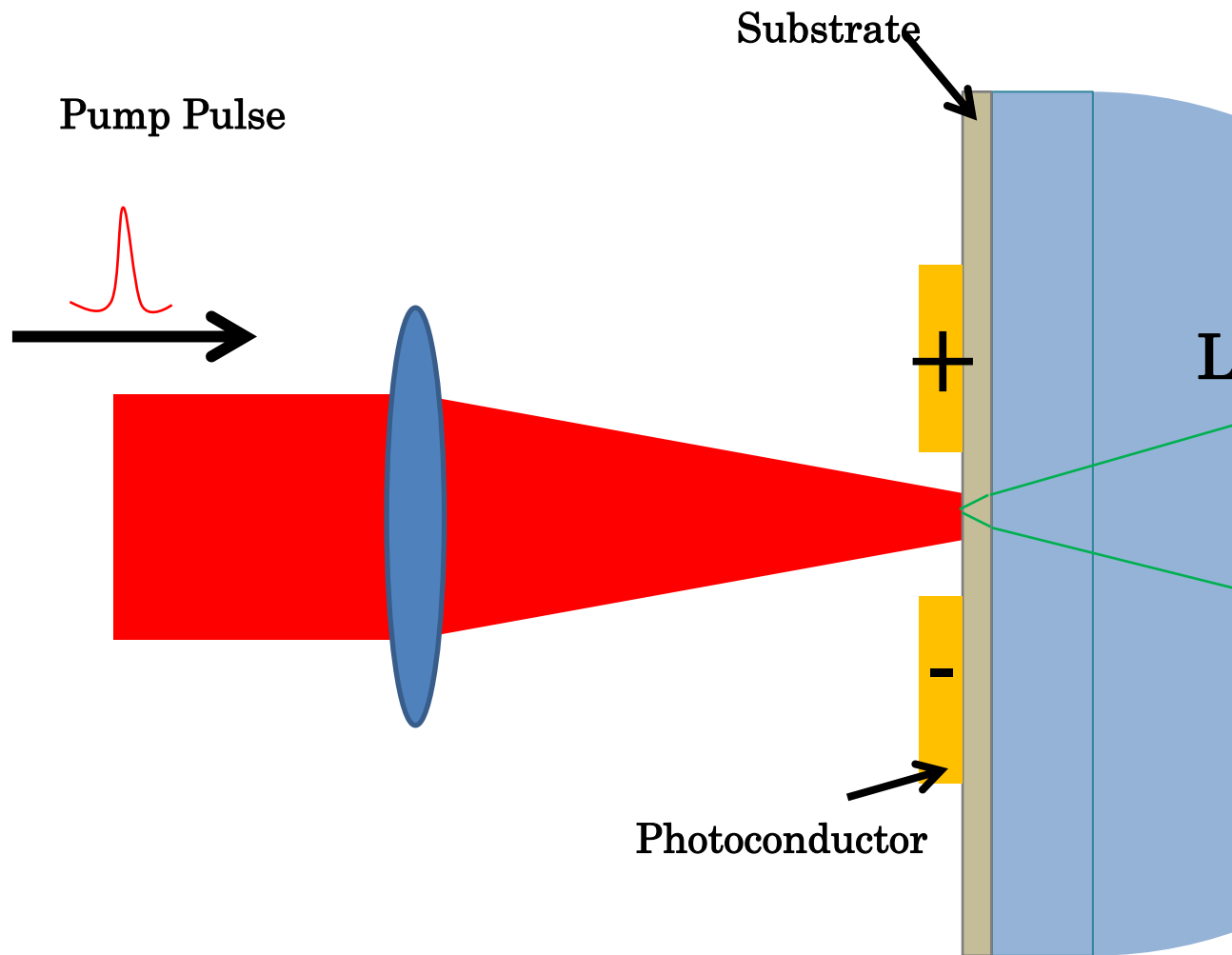
The mechanics of photo-generated free carriers in a semiconductor is well described by the classical Drude model. According to such model, the average velocities of free carriers shall obey the differential equation as [6]:

$$\frac{d\nu(t)}{dt} = -\frac{\nu(t)}{\tau} + \frac{q}{m} E(t), \quad (2-3)$$

where τ is the momentum relaxation time and m is the effective mass of the carrier. The current density $n(t)q\nu(t)$ represents the impulse response of the PC antenna, i.e., the response to a delta-function-like optical pumping. Figure 2-4 shows a standard shape of the photocurrent density in the function of time from emitter and that the corresponding THz wave propagated in far field, and the light pulse is considered to have the Gaussian distribution.

The process of generated THz pulse emitted from the substrate side is

demonstrated in Figure 2-3 left (side view). It is based on the antenna theory that shows that a dipole antenna on the surface of dielectric material emits roughly $\epsilon^{3/2} / 2$ times more power to the dielectric material than to the air, where ϵ is the relative dielectric constant of the substrate [9, 10].



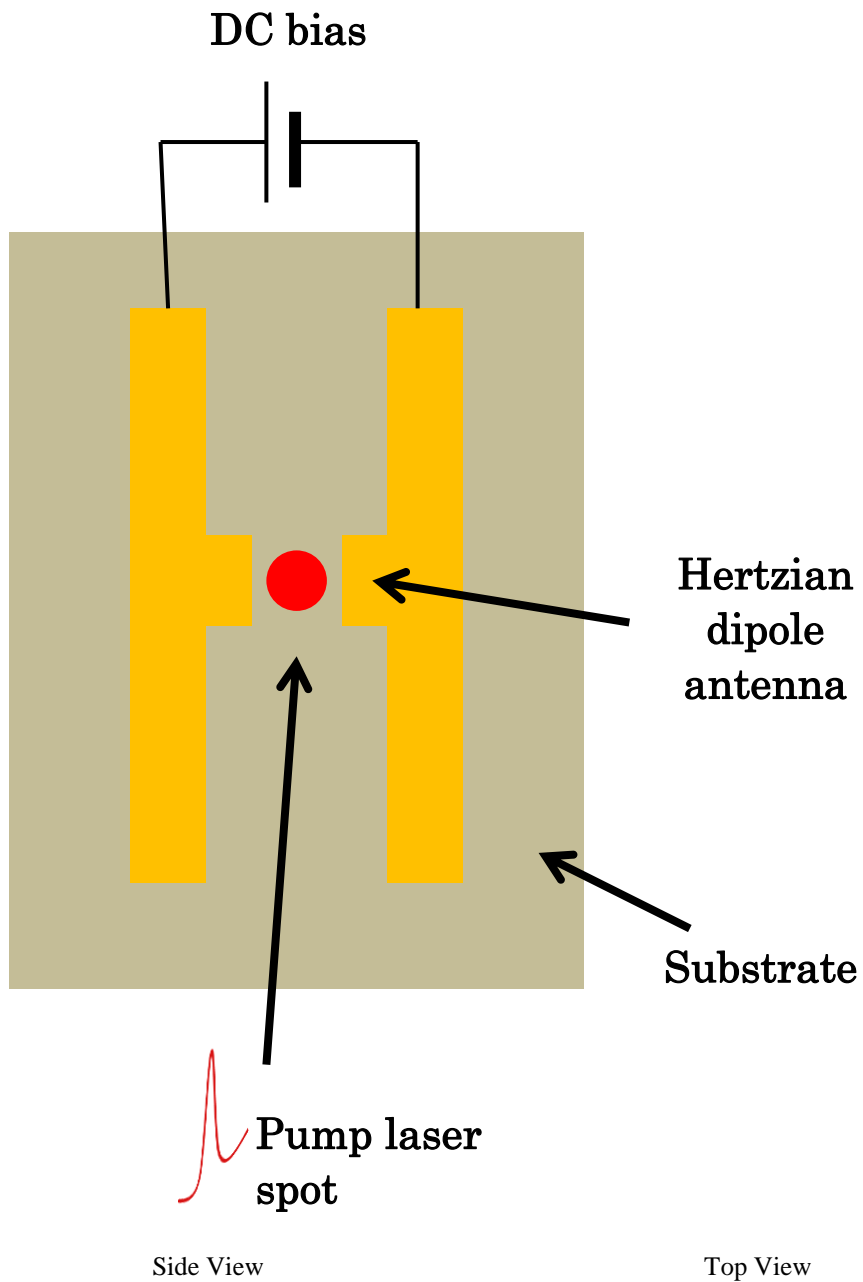


Figure 2-3. Common pulsed THz wave generation from a PC antenna excited by femtosecond light pulse

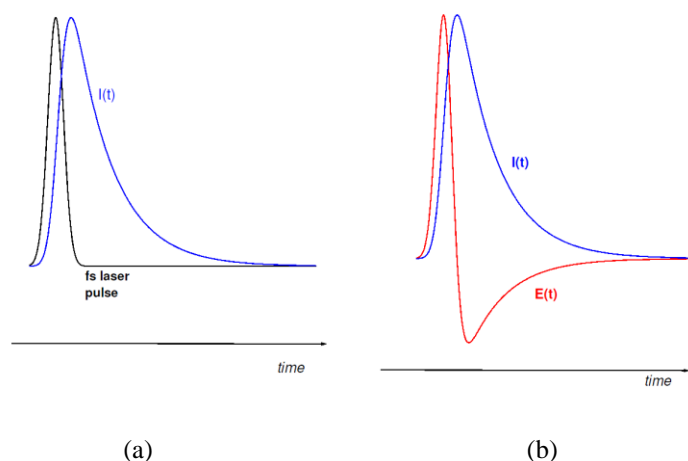


Figure 2-4. THz pulse generation in a PC antenna. (a) fs laser pulse induces a transient current.
 (b) The induced current leads to radiation of a THz transient.

When a PC antenna works as a detector, the incoming femtosecond laser pulses divided partially from the pumping pulses by a beam splitter is focused between protruding parts of the electrodes, which will inject free carriers leading to a drop of the resistance across the antenna. The electric field of the focused incident THz radiation induces a transient bias voltage across the 5 μm gap between the two arms of this detecting antenna. Thus when the laser pulse coincides spatially and temporally with the THz field, a photocurrent is induced which is proportional to the incident electric field. Whiling time delay stage operating, the incoming pulses which is narrow in comparison to the emitted THz pulse, acts as a gated sampling signal for recording the waveform of THz pulse point by point. Figure 2-5 shows this mapping procedure [11].

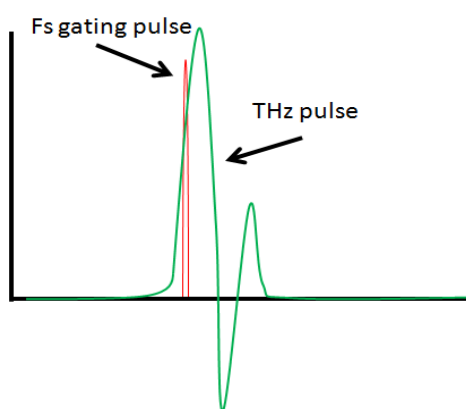


Figure 2-5. How the THz pulse is mapped by the gating fs laser pulse

The transient photocurrent $j(\tau)$ (where τ is the delay time), is a convolution of the electric field of THz pulse “ $E(t)$ ”, and the detector response “ $D(t)$ ”, as given in Equation (2-4):

$$j(\tau) = \frac{1}{T} \int_0^T E(t)D(t-\tau)dt, \quad (2-4)$$

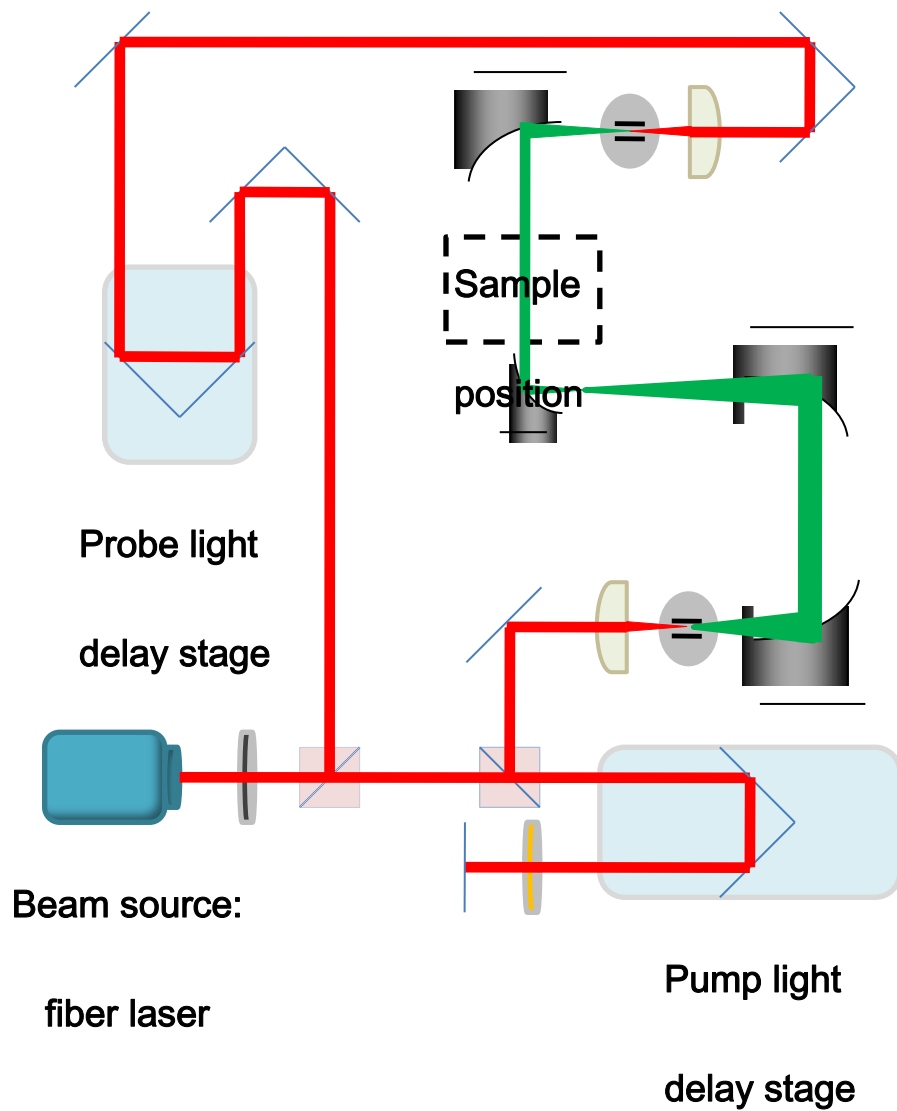
If the detector response were a delta function, the time domain signal would be equal to the electric field. But as long as our analysis is performed by dividing the sample signal with the reference signal in the frequency domain, where the time domain convolution becomes a product leaving only the ratio of the electric fields, it is not necessary to aware of the exact form of $D(t)$ [11].

2.1.3 THz-TDS with transmission geometry

Experimental data of Chapter 3 of this thesis was obtained by using a THz-TDS setup with transmission geometry, shown in Figure 2-6.

A femtosecond fiber laser with two wavelength models of 780 nm and 1650 nm (we used a combination of three dielectric multilayer mirrors as a frequency filter to block the output of 1650 nm mode, which aren't presented in Figure 2-6) with the pulse width of approximate 100 fs and a repetition rate of 76 MHz. The average output power is 28 mW for pumping and gating the PC antennas.

The laser pulse was divided into pump pulse and probe pulse by a cube beam splitter, and then focused onto the antenna chips by lenses ($f=18$ mm). After THz pulses were emitted, they were collected and collimated by a silicon lens attached to the back side of the chip. Without the silicon lens, multiple reflections in the semiconductor material would considerably limit the efficient emission from the antenna [12, 13]. Then a set of off-axis parabolic mirrors are placed to guide and re-focus THz pulse onto the detector. The beam diameter around the optical path that we put samples in was larger than 10 mm up to about 14 mm. Additionally, because that the size of samples measured in Chapter 3 were limited to 10 mm, we set an aperture in the path of THz wave to restrict THz beam of 7 mm.



Graphic symbol

- | | | | |
|---|---------------|---|---------------------|
|  | Beam splitter |  | $\frac{\lambda}{4}$ |
|  | Plus lens |  | wavelength plate |
|  | PC antenna |  | Paraboloidal mirror |
|  | THz wave |  | Incident wave |

Figure 2-6. Scheme of THz-TDS in transmission geometry that was used in this research

The length of time delay stage in our setup is up to 400 mm resulted to a very long scanning range, which according to the theory of Fourier Transformation, high resolution in frequency spectrum is possible (up to 0.25 GHz by our THz-TDS setup). Considering the duration of one measurement, we have set stage to scan 8192 points with the step length of 8 μm , leading to a frequency resolution as 1.1 GHz.

Two PC antennas applied in our THz-TDS setup were manufactured by Hamamatsu Photonics K. K. The reference signal of THz pulse generated and acquired by our transmission setup is shown in Figure 2-7.

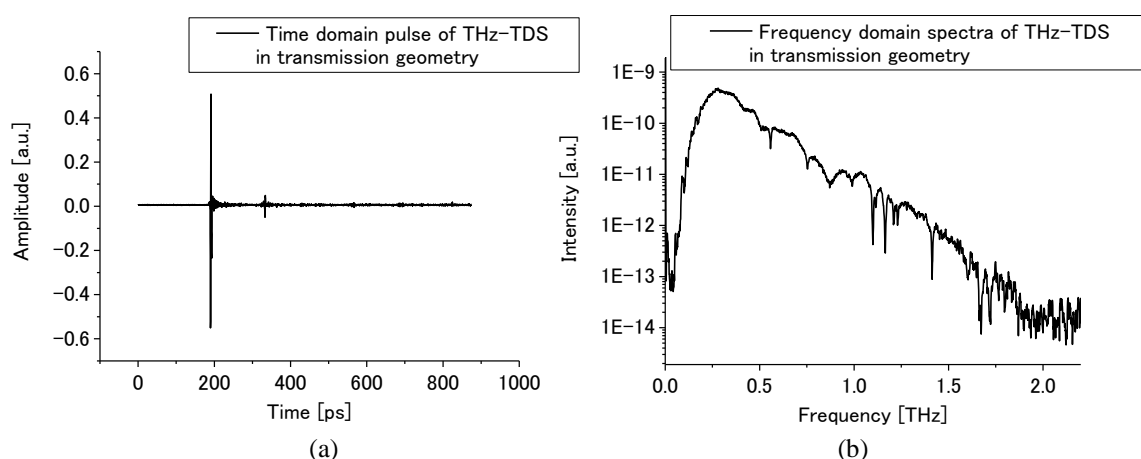


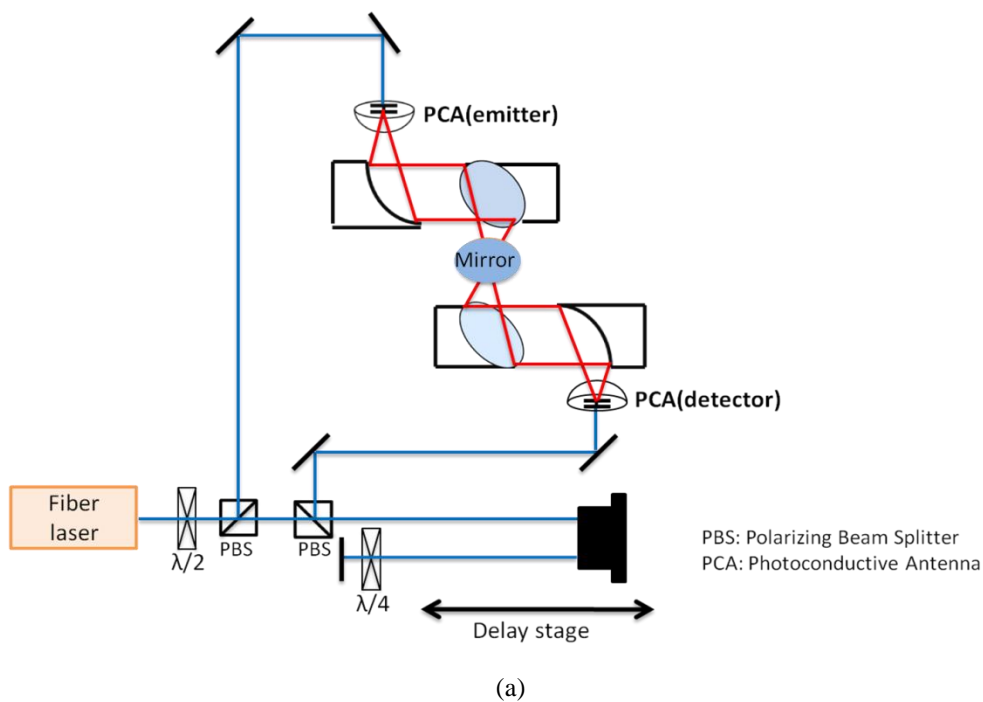
Figure 2-7. Reference pulse of THz-TDS in transmission geometry

2.1.4 THz-TDS with reflection geometry

Experimental Data of section 2 from Chapter 5 was obtained by using the THz-TDS setups with reflection geometry, shown in Figure 2-8 (a) and (b). Experimental Data of section 2 from Chapter 4 was also acquired by applying the setup shown in Figure 2-8 (b). Experimental Data of section 3-4 from Chapter 4 was achieved by another THz-TDS with reflection geometry as shown in Figure 2-8 (c).

For the setup (a), the femtosecond laser is same to the one described in Section 2.13. After THz pulse was generated by PC antenna, it was guided by off-axis parabolic mirror and then reflected by a flat Aluminum mirror which was considered as the reference. The THz beam in this setup incident onto the sample with a glancing incident

angle. By using another two off-axis parabolic mirrors, pulse was re-focused onto the gap detector's chip. We operated this setup with the same PC antennas manufactured by Hamamatsu Photonics K. K. We acquired the frequency resolution of 1.1 GHz for the measurements in Chapter 5, while it was set to 10 GHz for the measurements in Chapter 4. The reference pulse of the setup presented in Figure 2-8 (a) is shown in Figure 2-9 (a). For the setup of Figure 2-8 (b), THz wave pulse generated by PC antenna goes into a parabolic mirror where it is collimated, and then one piece of wire grid polarizer reflect beam to pass through another piece of it with a 45 degrees variation.



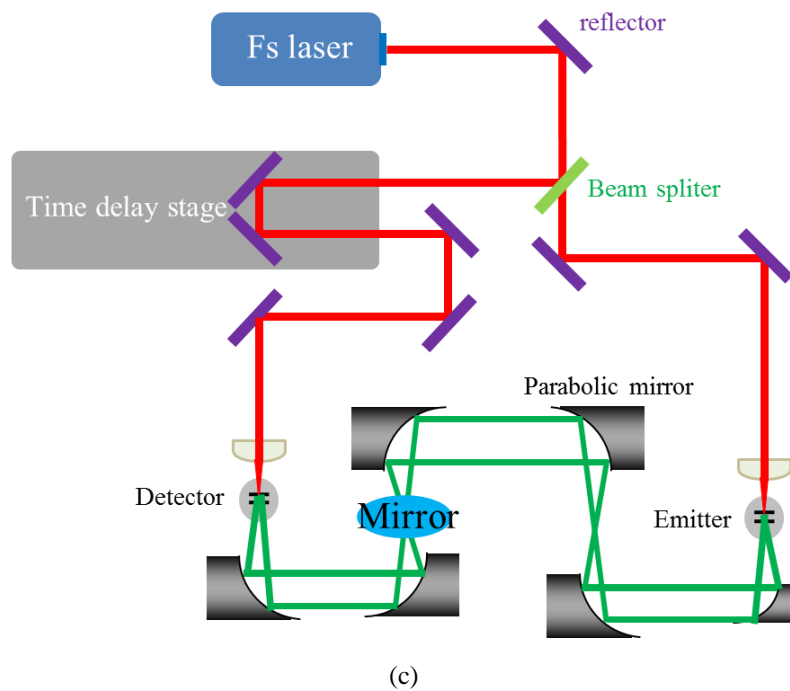
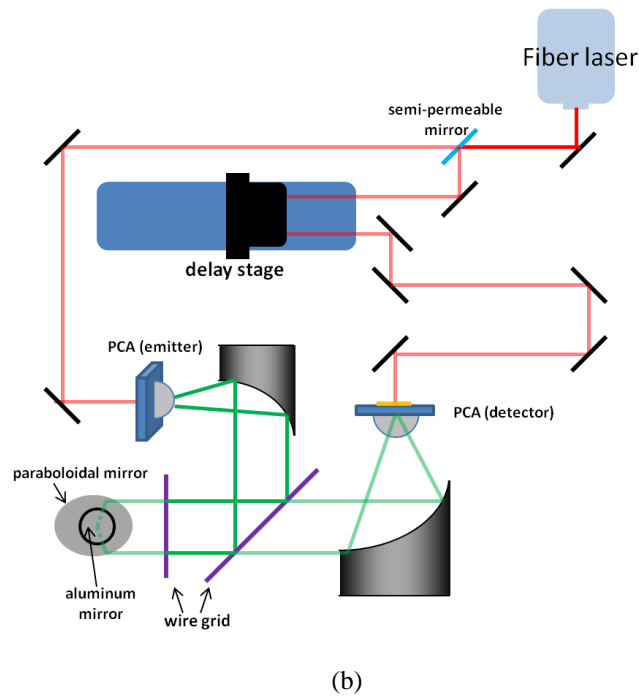


Figure 2-8. Three setups of THz-TDS with reflection geometry

It makes the beam reflected from mirror to get through the first piece of polarizer and get collected by another PC antenna. This setup allows a vertical incidence of THz beam onto the samples. The reference pulse generated and obtained by it is shown in

Figure 2-9 (b). For the setup shown in Figure 2-8 (c), the THz radiation was soft focused using a parabolic mirror with an effective focal length of 4 inches and incident onto sample at 20° angle (an aluminum plate mirror is replacing the sample as shown in Figure 2-8 (c)).

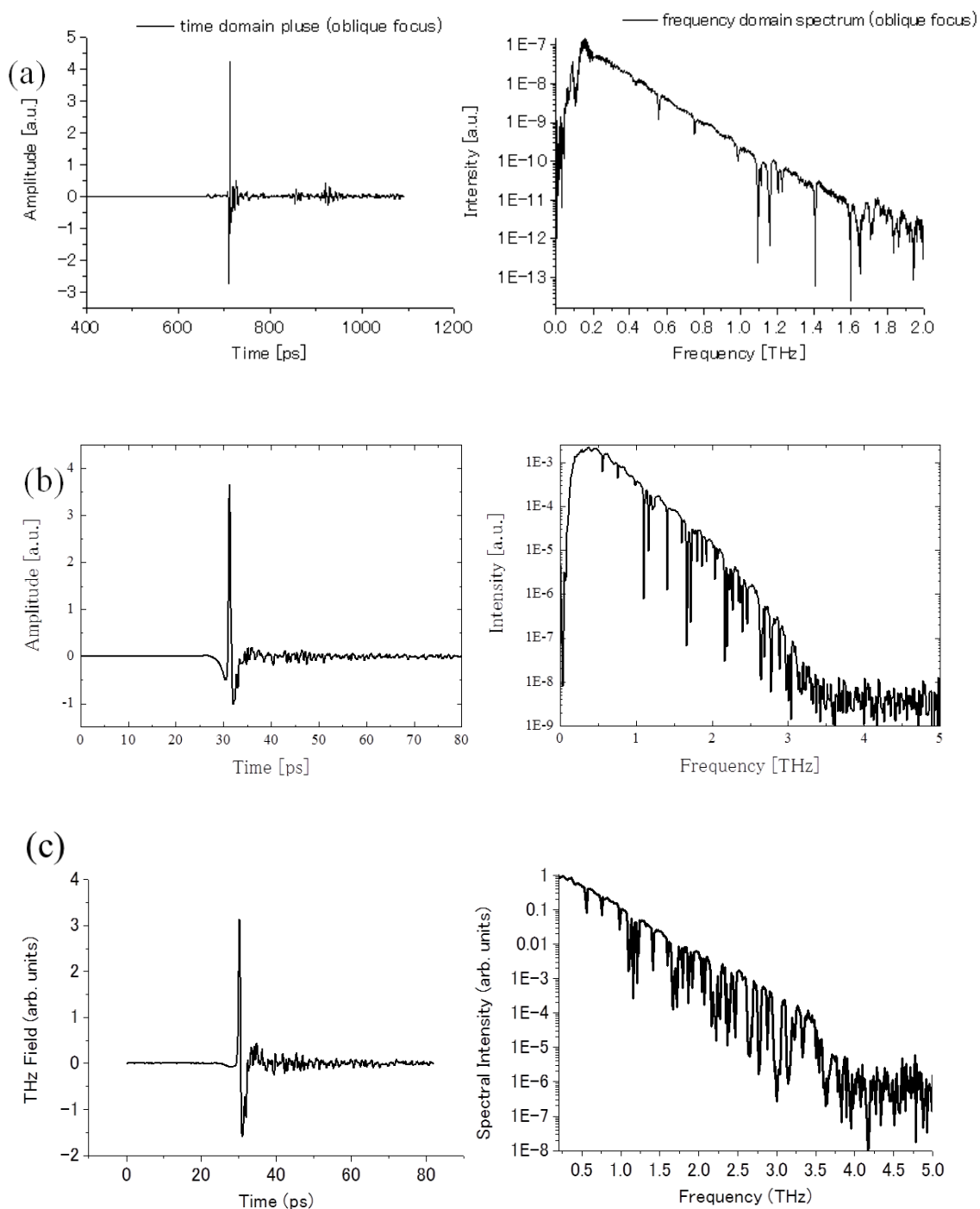


Figure 2-9. Reference Pulse of THz-TDS with reflection geometry.

- (a) Setup of Figure 2-8 (a) (oblique focus)
- (b) Setup of Figure 2-8 (b) (vertical focus)
- (c) Setup of Figure 2-8 (c) (oblique focus)

2.2 Study of cross-polarization effect of parabolic mirrors applied in the THz setup

2.2.1 Motivation and research approaches

Parabolic mirror also known as the parabolic reflector is a commonly used optical element in THz experimental setup all over the world. The ability of focusing any collimated beam which is parallel incident along its axis to a certain point, or the opposite process that any beam irradiate from its focal point can be collimated into a given direction brings great convenient for the alignment of an optical setup. The simple theory behind it can be easily found in many textbook, articles on internet or even elaborating videos were uploaded for people who may concern. The basic of such theory will be skipped and not be presented here. However, the simplicity of parabolic mirror may have mislead many researchers including me to consider it as a “perfect” optical element, which could cause the misuse and blind us for concealing the real result in the measurements of a setup including it. Such an example is presented in Figure 2-13.

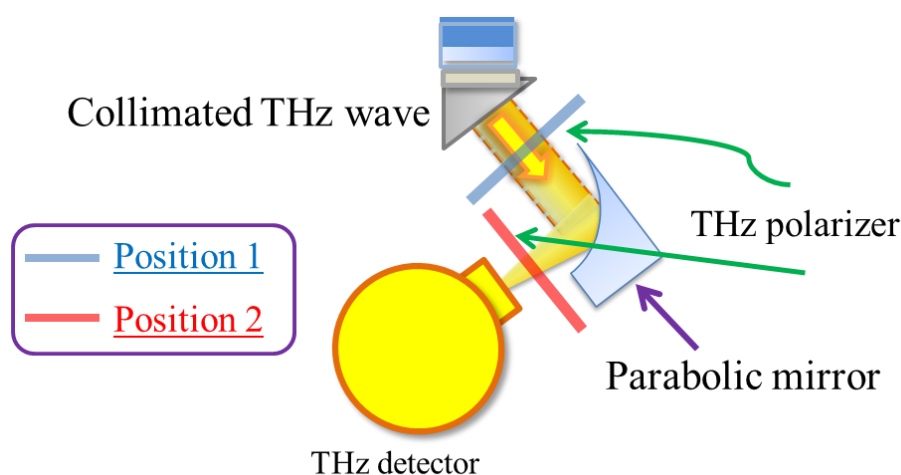


Figure 2-13. Setup for testifying polarization of emitted THz wave applying a parabolic mirror

Omitting non-crucial details, collimated THz radiation was emitted from a source and focused by a parabolic mirror into the THz detector. An inspection of the polarization status of the THz radiation was required. Thus a THz polarizer was inserted into the optical path, which only allows radiation to pass with a certain polarization direction. By placing this polarizer in different locations such as being described in Figure 2-13 as position 1 and 2, different results were acquired which is presented in Figure 2-14. A polarization-irrelevant detector named as bolometer [14] was applied for measuring the energy of THz radiation. It shouldn't affect the results of polarization measurements.

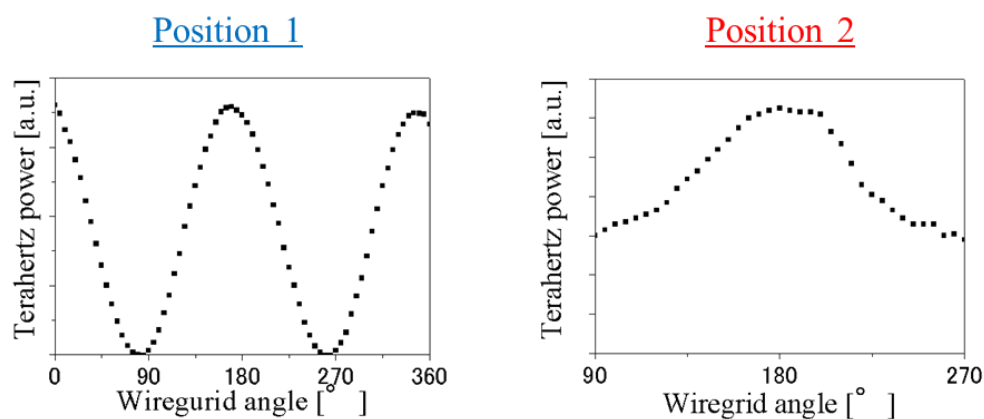


Figure 2-14. Results of the measurements for inspecting polarization of THz radiation

The result of position 1 indicated that the polarization of emitted THz radiation was linearly polarized, while the result of position 2 suggested it should be elliptically polarized. The possible explanation for this contradictory lies in the parabolic mirror the system applied. Inspired by these results, I started a study of cross polarization effect of parabolic mirror. The conclusion will be presented in later section and author hope that it can provide an improvement for the experiments involving the polarization study applying a setup with parabolic mirror. Additionally, it shall be an instructive guide for the researchers who encounter with similar problems.

A mathematical model was established and well explained in the following section, along with the experimental results to proof its validity.

2.2.2 Analytical simulations and measurements in real-field

Electromagnetic wave reflected from a parabolic mirror is essentially no different with it being reflected from a plane mirror, because that according to the knowledge of calculus, the curved surface of parabolic mirror can be equivalent into a huge amount of continuous plane mirror with infinitely small area. Let's consider a simple reflection model as shown in Figure 2-15 firstly.

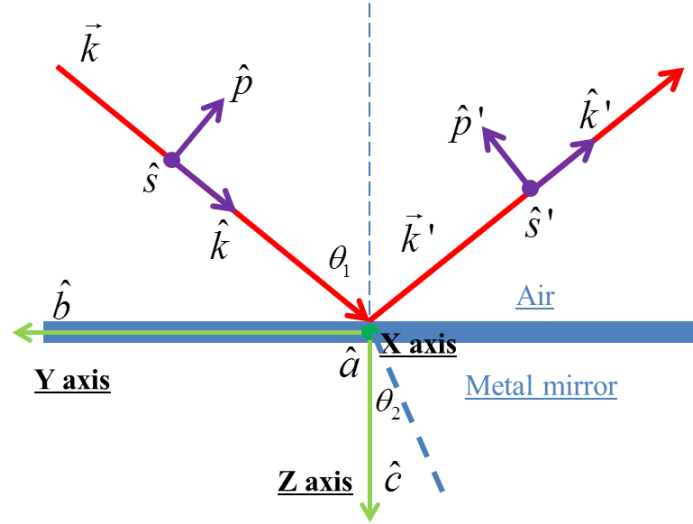


Figure 2-15. Beam reflected from a surface of metal mirror

There are three coordinate systems in this reflection model which can be described in following equations:

$$\hat{p} \times \hat{s} = \hat{k}, \quad (2-5)$$

$$\hat{p}' \times \hat{s}' = \hat{k}', \quad (2-6)$$

$$\hat{a} \times \hat{b} = \hat{c}, \quad (2-7)$$

The Fresnel formula for metal surface can be applied in our calculation as:

$$r_p = \frac{\tilde{n} \cos \theta_1 - \cos \theta_2}{\tilde{n} \cos \theta_1 + \cos \theta_2} \quad r_s = \frac{\cos \theta_1 - \tilde{n} \cos \theta_2}{\cos \theta_1 + \tilde{n} \cos \theta_2} \quad (2-8)$$

Along with the Snell's law:

$$\tilde{n} \sin \theta_2 = \sin \theta_1$$

$$\tilde{n} = n + i \cdot k, \quad (2-9)$$

In this case, the commonly referred refraction angle θ_2 is no longer representing any physical angle. It is a complex number for calculation. If we consider an incident beam has a certain polarization described in coordinate system $\langle \hat{p}, \hat{s}, \hat{k} \rangle$, it can have a simple expression and be written as follow:

$$\vec{E} = \begin{pmatrix} 0 \\ p \\ s \end{pmatrix}, \quad (2-10)$$

As for the reflected beam, the polarization can be described in the same expression but in coordinate system $\langle \hat{p}', \hat{s}', \hat{k}' \rangle$, as shown in the following equation:

$$\vec{E} = \begin{pmatrix} 0 \\ p' \\ s' \end{pmatrix}, \quad (2-11)$$

And we could have the parameters correlated with each other following the Fresnel formula as described earlier in this paper.

$$p' = r_p \cdot p, \quad (2-12)$$

$$s' = r_s \cdot s, \quad (2-13)$$

The parameters p', p, s', s can be the complex number for describing both the amplitude and phase factor of the E-field by its coordinate vector respectively. However, it certainly introduces trouble for later discussion if the polarization needs to be discussed in different coordinate. Thus, we want them expressed in the same system. In this example, E-field will be unified in the coordinate of $\langle \hat{a}, \hat{b}, \hat{c} \rangle$

According to the theory of linear algebra, a transformation matrix can be found to switch polarization expression from a coordinate to another by defining the orthogonal unit vectors with each other. If we have the incident angle of the beam described in $\langle \hat{a}, \hat{b}, \hat{c} \rangle$ (that means if we know the coordinate of vector \hat{k} described in (x, y, z) , which representing the direction of a beam pointing at) and the polarization described in $\langle \hat{p}, \hat{s}, \hat{k} \rangle$ in advance, then the transformation matrix can be derived from the following equations:

$$\hat{k} = (x \cdot \hat{a} + y \cdot \hat{b} + z \cdot \hat{c}) \cdot \lambda / 2\pi, \quad (2-14)$$

$$\hat{p} = \left(\frac{xz}{\sqrt{x^2 + y^2}} \cdot \hat{a} + \frac{yz}{\sqrt{x^2 + y^2}} \cdot \hat{b} - \sqrt{x^2 + y^2} \cdot \hat{c} \right) \cdot \lambda / 2\pi, \quad (2-15)$$

$$\hat{s} = \frac{-y}{\sqrt{x^2 + y^2}} \cdot \hat{a} + \frac{x}{\sqrt{x^2 + y^2}} \cdot \hat{b} - 0 \cdot \hat{c}, \quad (2-16)$$

Where λ the wavelength of the incident beam and the wave number vector shall have the following expression:

$$x^2 + y^2 + z^2 = \left(\frac{2\pi}{\lambda}\right)^2, \quad (2-17)$$

Thus, we can have

$$(\hat{k}, \hat{p}, \hat{s}) = (\hat{a}, \hat{b}, \hat{c}) \cdot A, \quad (2-18)$$

A is the transformation matrix, which has the following expression:

$$(\hat{k}, \hat{p}, \hat{s}) = (\hat{a}, \hat{b}, \hat{c}) \cdot \begin{bmatrix} \frac{\lambda x}{2\pi} & \frac{\lambda xz}{2\pi\sqrt{x^2 + y^2}} & \frac{-y}{\sqrt{x^2 + y^2}} \\ \frac{\lambda y}{2\pi} & \frac{\lambda yz}{2\pi\sqrt{x^2 + y^2}} & \frac{x}{\sqrt{x^2 + y^2}} \\ \frac{\lambda z}{2\pi} & \frac{-\lambda\sqrt{x^2 + y^2}}{2\pi} & 0 \end{bmatrix}, \quad (2-19)$$

The same process can be conducted between coordinate $\langle \hat{p}', \hat{s}', \hat{k}' \rangle$ and $\langle \hat{a}, \hat{b}, \hat{c} \rangle$, with the transformation matrix B between them being described as follow:

$$(\hat{k}', \hat{p}', \hat{s}') = (\hat{a}, \hat{b}, \hat{c}) \cdot \begin{bmatrix} \frac{\lambda x}{2\pi} & \frac{-\lambda xz}{2\pi\sqrt{x^2 + y^2}} & \frac{-y}{\sqrt{x^2 + y^2}} \\ \frac{\lambda y}{2\pi} & \frac{-\lambda yz}{2\pi\sqrt{x^2 + y^2}} & \frac{x}{\sqrt{x^2 + y^2}} \\ \frac{-\lambda z}{2\pi} & \frac{-\lambda\sqrt{x^2 + y^2}}{2\pi} & 0 \end{bmatrix}, \quad (2-20)$$

Thus, we can express the polarization described in $\langle \hat{p}, \hat{s}, \hat{k} \rangle$ and $\langle \hat{p}', \hat{s}', \hat{k}' \rangle$ into a unified system $\langle \hat{a}, \hat{b}, \hat{c} \rangle$, as follow:

$$\begin{pmatrix} E_x \\ E_y \\ E_z \end{pmatrix} = A \begin{pmatrix} 0 \\ p \\ s \end{pmatrix}, \quad (2-21)$$

$$\begin{pmatrix} E_x' \\ E_y' \\ E_z' \end{pmatrix} = B \begin{pmatrix} 0 \\ p' \\ s' \end{pmatrix}, \quad (2-22)$$

Then we can certainly get the expression as follow:

$$\begin{pmatrix} E_x' \\ E_y' \\ E_z' \end{pmatrix} = B \begin{bmatrix} 0 & 0 & 0 \\ 0 & r_p & 0 \\ 0 & 0 & r_s \end{bmatrix} A^{-1} \begin{pmatrix} E_x \\ E_y \\ E_z \end{pmatrix}, \quad (2-23)$$

Where we define a matrix Z as follow:

$$Z = \begin{bmatrix} 0 & 0 & 0 \\ 0 & r_p & 0 \\ 0 & 0 & r_s \end{bmatrix}, \quad (2-24)$$

By now, we can easily have the expression of polarization for any beam reflected from a plate mirror (metal), as long as the refractive index of the mirror in complex form, incident angle, wavelength and initial polarization of the beam are given. However, if the surface of the mirror doesn't placed as it has been shown in Figure 2-15, what information is needed to calculate the polarization of reflected beam in this case? In this case do we need to recalculate the incident angle and initial polarization of the beam to fit the new system? These questions can be answered by the following calculation.

We define the mirror always have a coordinate system as described in Figure 2-15. The initial mirror system is the system $\langle \hat{a}, \hat{b}, \hat{c} \rangle$. By relocated the surface of the mirror, such as rotation, a new system $\langle \hat{m}, \hat{n}, \hat{j} \rangle$ is established. This new coordinate system has the same relation of the surface of mirror. The figure 2-16 is used to demonstrate this process.

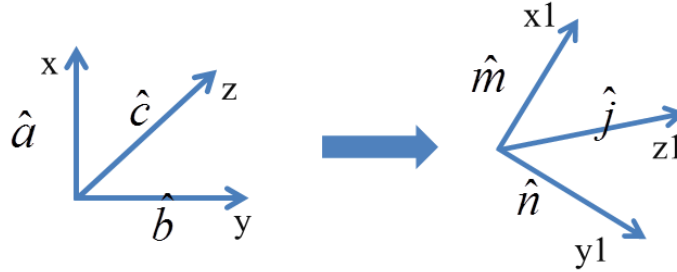


Figure 2-16. Coordinate conversion caused by rotation of the mirror

Let's assume that we know how the mirror rotated, thus the transformation matrix C_1 can be applied to have two coordinate systems have the following expression:

$$\hat{m} = C_{11}\hat{a} + C_{21}\hat{b} + C_{31}\hat{c}, \quad (2-25)$$

$$\hat{n} = C_{12}\hat{a} + C_{22}\hat{b} + C_{32}\hat{c}, \quad (2-26)$$

$$\hat{j} = C_{13}\hat{a} + C_{23}\hat{b} + C_{33}\hat{c}, \quad (2-27)$$

$$(\hat{m}, \hat{n}, \hat{j}) = (\hat{a}, \hat{b}, \hat{c})C_1, \quad (2-28)$$

Thus, if the same electromagnetic wave incident onto the rotated mirror, we can have the incident angle and initial polarization expressed in $\langle \hat{a}, \hat{b}, \hat{c} \rangle$ being calculated and

described in $\langle \hat{m}, \hat{n}, \hat{j} \rangle$ as follow:

$$\begin{pmatrix} x_1 \\ y_1 \\ z_1 \end{pmatrix} = C_1^{-1} \begin{pmatrix} x \\ y \\ z \end{pmatrix}, \quad \begin{pmatrix} Ex_1 \\ Ey_1 \\ Ez_1 \end{pmatrix} = C_1^{-1} \begin{pmatrix} Ex \\ Ey \\ Ez \end{pmatrix}, \quad (2-29)$$

By using the coordinate in $\langle \hat{m}, \hat{n}, \hat{j} \rangle$, polarization of reflected beam can be expressed in the equation similar to equation (2-) as follow:

$$\begin{pmatrix} Ex_1' \\ Ey_1' \\ Ez_1' \end{pmatrix} = B_1 \begin{bmatrix} 0 & 0 & 0 \\ 0 & r_{p1} & 0 \\ 0 & 0 & r_{s1} \end{bmatrix} A_1^{-1} \begin{pmatrix} Ex_1 \\ Ey_1 \\ Ez_1 \end{pmatrix}, \quad (2-30)$$

Furthermore, we can still have the expression in the original mirror system $\langle \hat{a}, \hat{b}, \hat{c} \rangle$ by transforming it back as follow:

$$\begin{pmatrix} Ex' \\ Ey' \\ Ez' \end{pmatrix} = C_1 \begin{pmatrix} Ex_1' \\ Ey_1' \\ Ez_1' \end{pmatrix} = C_1 B_1 Z_1 A_1^{-1} C_1^{-1} \begin{pmatrix} Ex \\ Ey \\ Ez \end{pmatrix}, \quad (2-31)$$

Considering that the initial polarization is much easier to defined in the system $\langle \hat{p}, \hat{s}, \hat{k} \rangle$, the equation can be reformed as follow:

$$\begin{pmatrix} Ex' \\ Ey' \\ Ez' \end{pmatrix} = C_1 B_1 Z_1 A_1^{-1} C_1^{-1} A \begin{pmatrix} 0 \\ p \\ s \end{pmatrix}, \quad (2-32)$$

We are almost ready to calculate the polarization of beam reflected from a parabolic mirror. Several conditions need to be mentioned. In the calculation, we consider parallel beam incident onto parabolic mirror and get focused through its focal point. Thus no matter which part of parabolic mirror irradiate, the propagation direction and initial polarization of the incident beam is always the same in overall coordinate system.

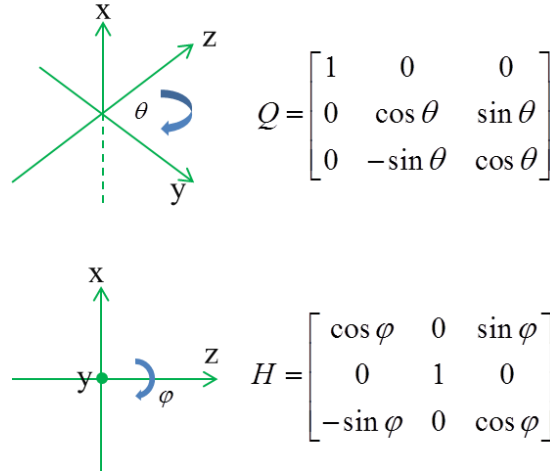


Figure 2-17. Transformation matrixes for rotating a coordinate in two directions

For easier calculation, we choose the tangent plane of the most center point of a parabolic mirror as the overall coordinate for defining the propagation direction and initial polarization of the incident beam. For calculation of reflection from any other part of the mirror, we simply need to somehow derive the transformation matrix C from that surface to the most center part of a parabolic mirror. Such a transformation can be described in Figure 2-17. Thus, the transformation matrix C can be expressed in the following equation using the rotation matrixes of Q and H

$$C = Q[\theta - \pi/4]Q[\theta + \pi/2]H[\varphi]Q^{-1}[\theta + \pi/2], \quad (2-33)$$

There are lot kinds of parabolic mirror in the market. We chose the 90 degrees off-axis parabolic mirror coated with aluminum (diameter 2 inch, effective focus length (EFL) 3 inch) for both calculation and measurements. For the measurements in real field, a LN laser with 633 nm linearly polarized and single mode was applied. Five points (A, B, C, D, E) from the parabolic mirror were chosen, which will be demonstrated in Figure 2-18. Point A presented the center point of the mirror.

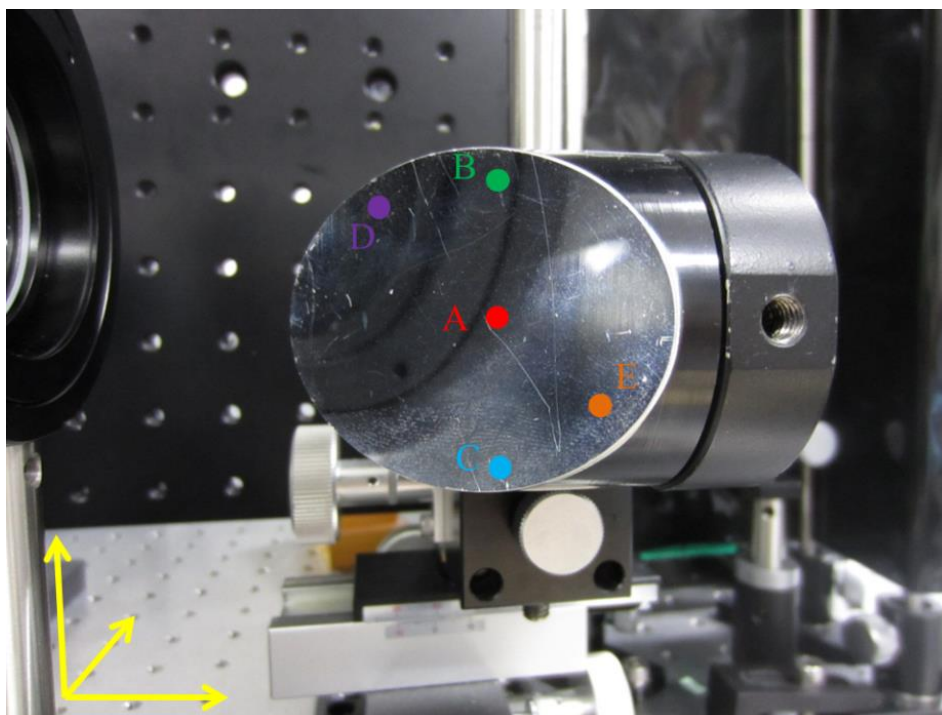


Figure 2-18. Image of the parabolic mirror we applied and locations of five points we chosen for measurements and simulations

Laser beam was collimated, pin-point and incident onto these five points to investigate the polarization of reflected beam from different part of the mirror. Coordinates of point B, C, D and E relative to point A are presented in the Table 2-1.

Table 2-1. Coordinate of five points related to point A

	Vertical axis	Horizontal axis
A	0.0 mm	0.0 mm
B	+23.0 mm	0.0 mm
C	-24.0 mm	0.0 mm
D	+17.0 mm	+15.5 mm
E	-16.0 mm	-17.8 mm

Due to the factor that parabolic mirrors are often used in pairs, the investigation of measurements and simulations were conducted by the case of a single parabolic mirror and the pairs of two identical parabolic mirror. An image of the experimental setup we

used for the single mirror measurement can be found in Figure 2-19.

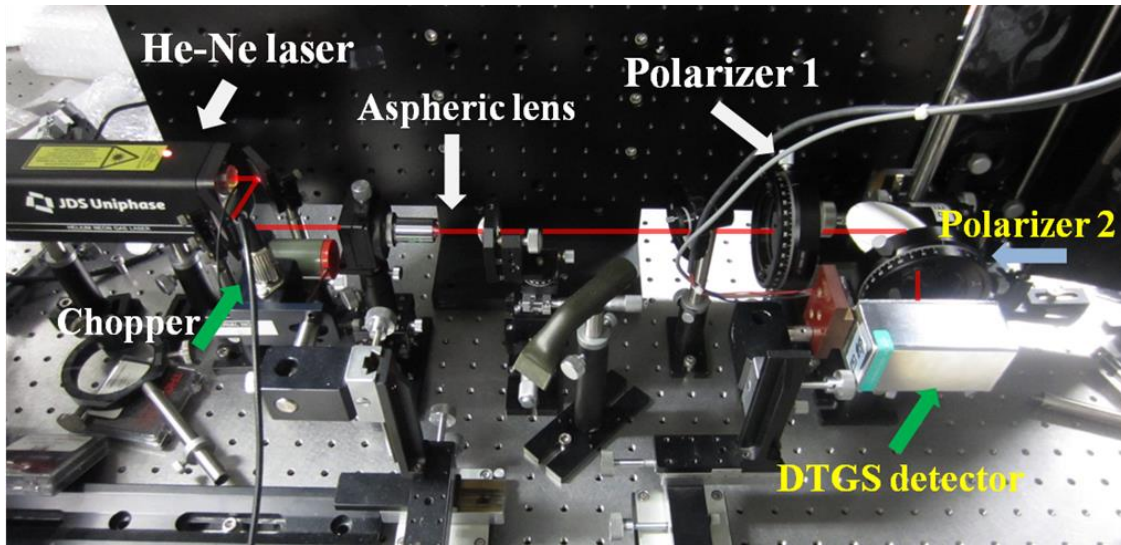
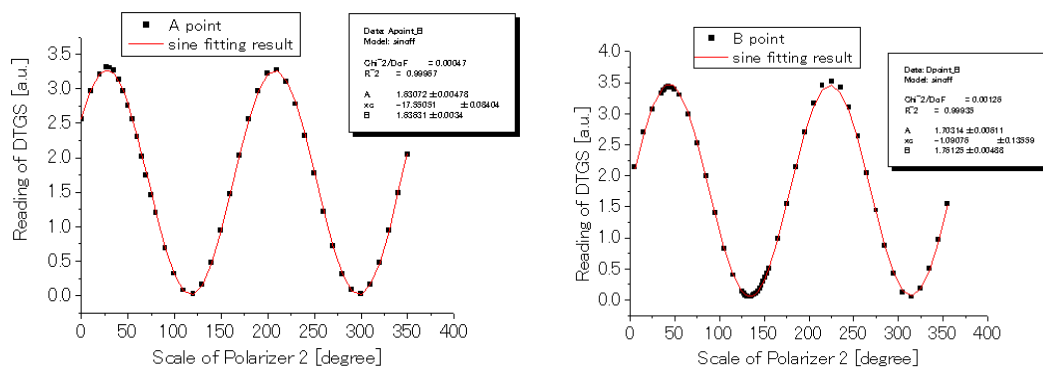


Figure 2-19. An experimental setup for the measurement of single parabolic mirror

Two absorption type polarizers have been applied for the measurements of polarization. Thus, only the energy of electric field with a polarization same as the axis of the polarizer can penetrate it while energy of other direction all restrained. The extinction ratio for both polarizers is over 20,000:1 at 633 nm which provide fine accuracy for the measurements. The polarizer 1 set the incident beam linearly polarized. Second polarizer was rotated allowing one direction polarized beam to propagate at a time for 360 degrees to detect the energy of electric field in all directions.

The raw data of the measurements of five points are presented in Figure 2-20. They are obscure for understanding the meanings. Thus, an analysis has been conducted and presented in Figure 2-21 (right part).



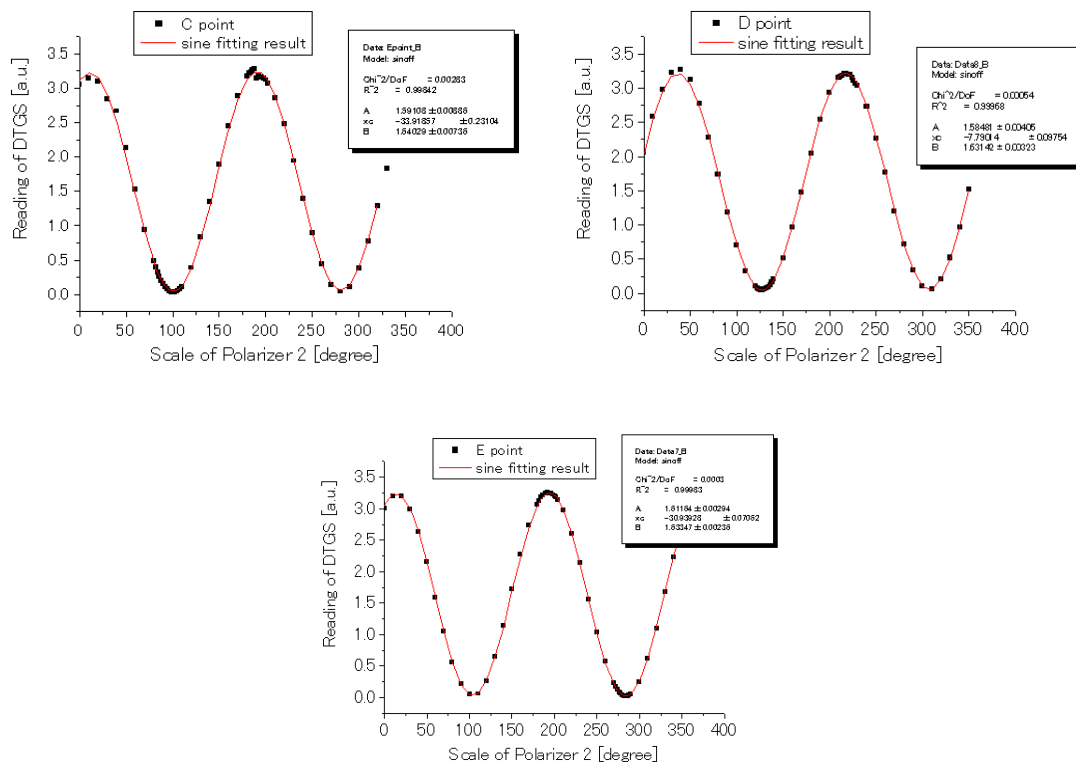


Figure 2-20. Measurements data of five points on the parabolic mirror

Additionally, we need to point out that the polarization results is a relative vision according to the observation angle. For later discussion, the observation plane has been set at the focus point towards the parabolic mirror, as shown in Figure 2-21 (left part).

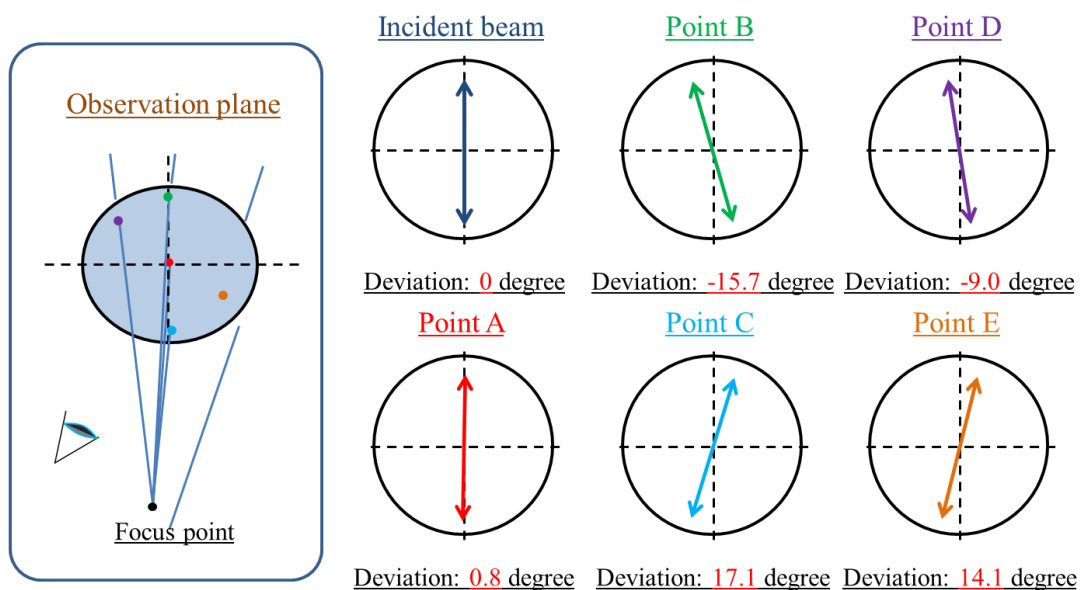
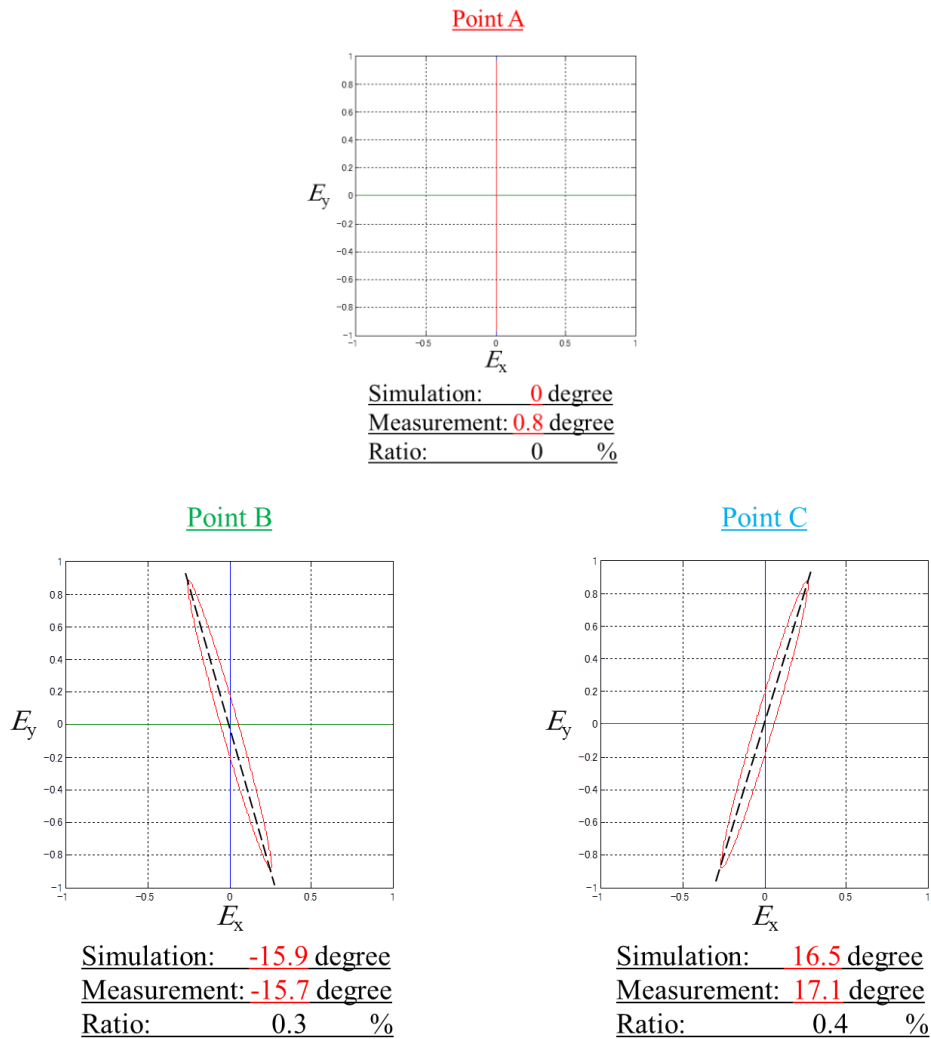


Figure 2-21. Polarization of beam reflected from five points of mirror

Next, simulation results are presented and compared to the measurements. The complex refractive index of aluminum at 635.8 nm $n=1.39$ $k=7.65$ was applied in the calculation [28]. A parameter was defined to describe the ratio of depolarization as follow:

$$Ratio = \frac{E_{\min}^2}{E_{\max}^2} = \frac{I_{\min}}{I_{\max}}, \quad (2-34)$$

Figure 2-22 present the comparison of simulations and measurements. Red lines present the polarization calculated by the model described previously in this section; dash black lines presented the measured results.



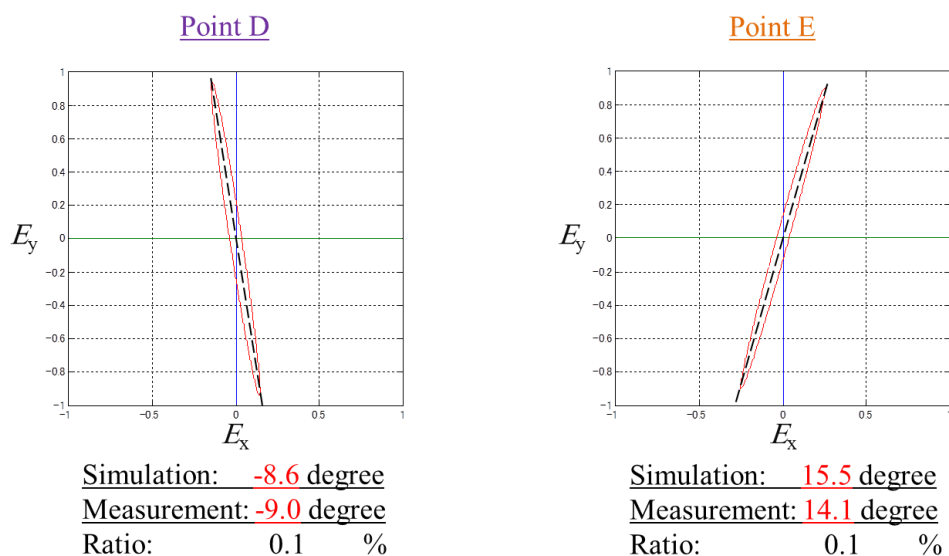
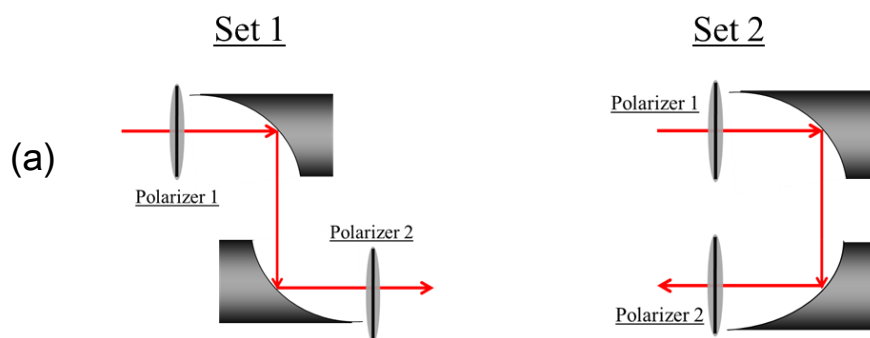


Figure 2-22. Comparison of calculations and measurements of the beam reflected from a single parabolic mirror

From the results, good consistence between calculation and measurement has been observed as well as proofing that the parabolic mirror does cause the cross polarization of electromagnetic beam being reflected from it. In the case of incident beam with a symmetrical profile and a big dimension, cross polarization can be restrained by incident the beam into the center part of the mirror due to the compensation of parabolic mirror's symmetry. However, a laser beam with small dimension or THz beam which is not visible, great attention is required in the alignment of the path to have beam reflected from the center of parabolic mirror.

Next, two situations of a pair of parabolic mirrors are considered. Their setup can be found in Figure 2-23 (a), along with the images of experiments (Figure 2-23 (b, c)).



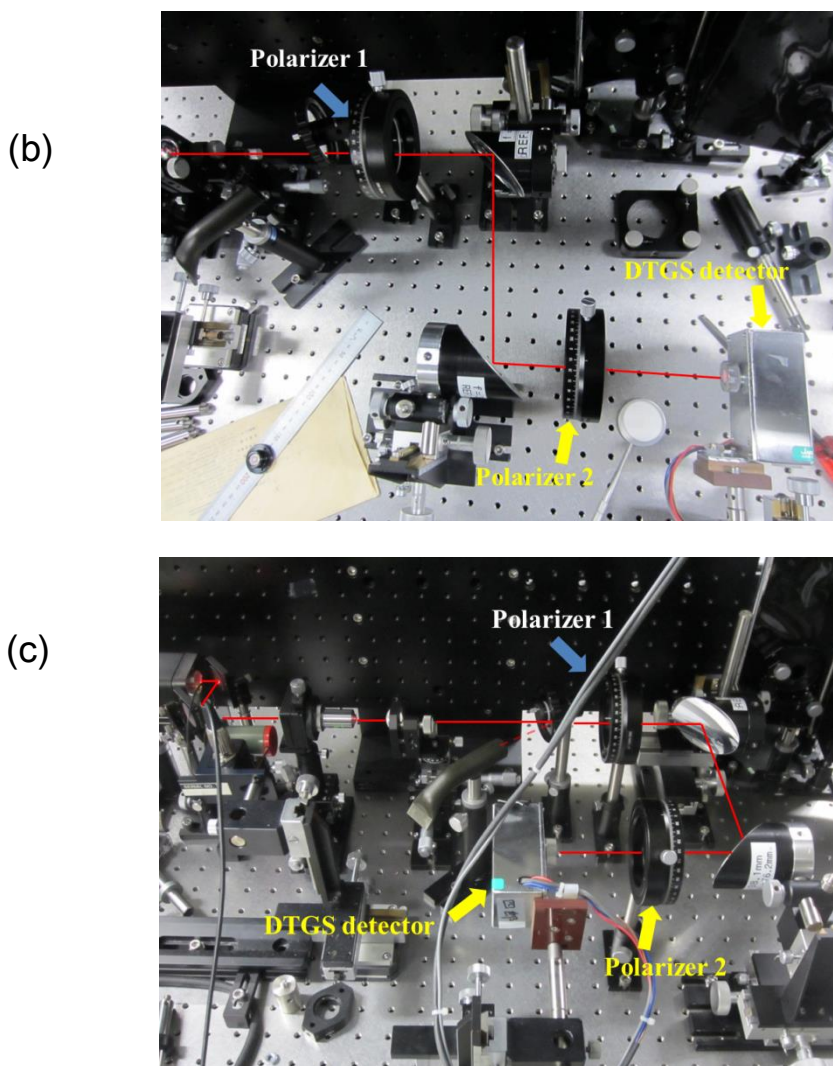


Figure 2-23. Two different situations of a pair of parabolic mirrors

Similar measurements have been conducted. Simulation program has been adapted for calculation the reflection of two surfaces. The comparison of the measurements and simulations is presented in the Table 2-2 (set 1) and Table 2-3 (set 2) respectively.

Table 2-2. Results of simulations and measurements of set 1

	Point A	Point B	Point C	Point D	Point E
Simulation	0 degree	-0.5 degree	0.5 degree	-0.7 degree	0.4 degree
Measurement	0.8 degree	-1.3 degree	2.5 degree	1.8 degree	1.5 degree
Ratio	0%	0.0016%	0.0018%	0%	0%

Table 2-3. Results of simulations and measurements of set 2

	Point A	Point B	Point C	Point D	Point E
Simulation	0 degree	28.9 degree	-29.1degree	-14.7degree	26.5degree
Measurement	-0.9 degree	31.4 degree	-33.5degree	17.4degree	-26.4degree
Ratio	0%	0.1%	0.11%	0.1%	0.04%

A visualized summary based on results in Table 2-2 and 2-3 is presented in Figure 24.

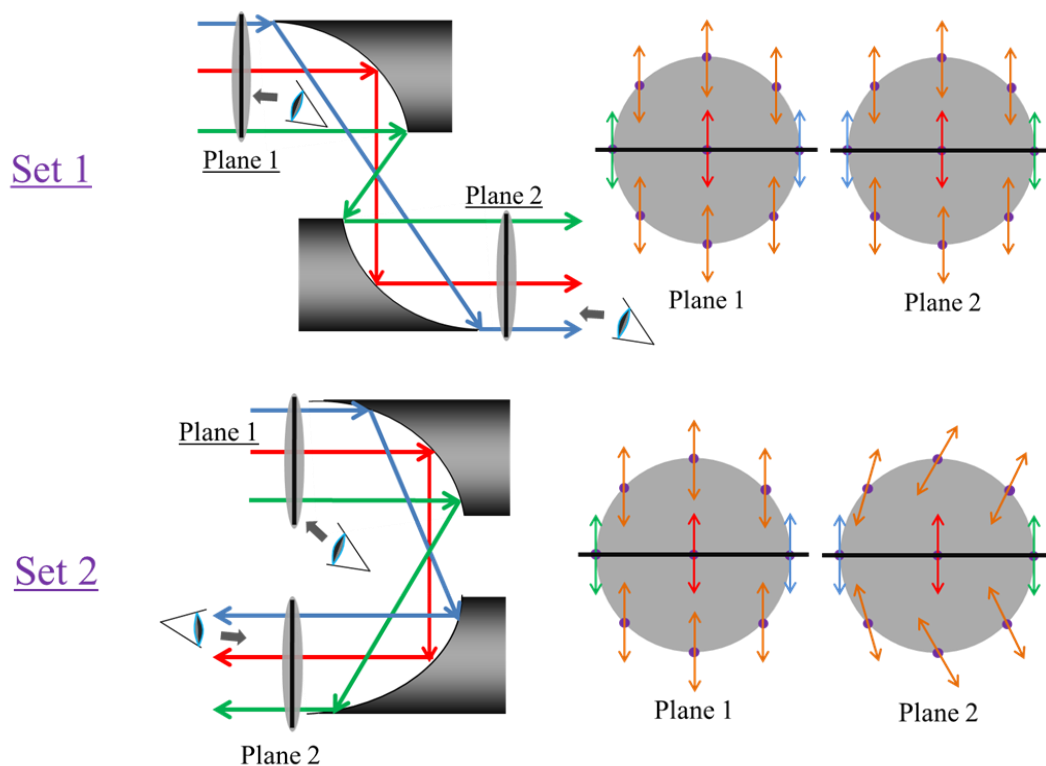


Figure 2-24. Polarization of beam reflected from different points of a pair of parabolic mirrors

2.2.3 Conclusion

We have experimentally and theoretically prove that the parabolic mirror can have a cross polarization effect on the incident electromagnetic wave. The situation of a single parabolic mirror and a pair of mirrors in two sets were studied respectively. We demonstrated that parabolic mirror can change the polarization of the beam according to which part of the mirror that the beam incident onto. However, it still keeps the linearization of polarization.

In the case of a single parabolic mirror: alignment must be conducted carefully to have beam incident symmetrically onto the mirror.

In the case of a pair of parabolic mirrors: although both situations of set 1 and 2 can keep the reflection beam collimated, one shall always use the layout of set 1 as

possible to keep the polarization of the beam profile stays the same.

This study provides an instructive guide for those who concern about the accuracy of their setup for measurements involving polarization, as well as an alternative approach to manipulate the polarization of the electromagnetic wave on purpose without a reduce of the energy in tradition way by using a beam splitter or a polarizer.

2.3 Summary

The experimental setup used for measurements introduced in later chapters was presented in chapter 2. THz-TDS is a well-developed and widely applied approach in the terahertz research field all over the world. The work author have contributed were mainly achieved by THz-TDS. Next, the study of cross-polarization effect of the parabolic mirror was presented. Due to the popularity of the parabolic mirror as an optical element in many experimental setups, it was urgent to aware researchers in terahertz field the imperfectness of parabolic mirror. Both theoretical calculation and measurements were conducted with their results presented in this chapter, to demonstrate the cross-polarization effect it could apply to the electromagnetic field. Advices were provided for restraining it to minim level.

Reference

- [1] Moeller KD, Rothschild WG, George Grüner, “Coherent source submillimeter wave spectroscopy”, *Millimeter and Submillimeter Wave Spectroscopy of Solids*, Springer, Berlin, 51-109 (1998)
- [2] G. Kozlov, A. Volkov, “Coherent source submillimeter wave spectroscopy”, Wiley, New-York (1971)
- [3] M. van Exter, Ch. Fattering, D. Grischkowsky: *Appl. Phys. Lett.* 55, 337 (1989)
- [4] M. Ketchen, D. Grischkowsky, T. Chen, C.-C. Chi, I. Duling, III, N. Halas, J.-M. Halbout, J. Kash, G. Li: *Appl. Phys. Lett.* 48, 751 (1986)
- [5] M. van Exter, D. Grischkowsky: *IEEE Trans. Microwave Theory Tech.* 38, 1684 (1990)
- [6] K. Sakai (Ed.), M. Tani, *Introduction to Terahertz Pulses, Terahertz Optoelectronics*, Springer-Verlag, page 3 (2005).
- [7] S. Nishizawa, K. Sakai (Ed.), *Terahertz Time-Domain Spectroscopy, Terahertz Optoelectronics*, Springer-Verlag, page 204 (2005)
- [8] PCA - Photoconductive Antenna for terahertz waves, parts of PCA for THz applications, [http://www.dmp Photonics.com/Photoconductive Antenna THz.htm](http://www.dmp Photonics.com/PhotoconductiveAntennaTHz.htm).
- [9] K. Sakai, M. Tani, “Terahertz-Pulse Emission from Photoconductive Antennas”, *Terahertz Optoelectronics*, Springer-Verlag, Section 1 Chapter 2, paper 6, 9-10 (2005)
- [10] D. Rutledge, D. Neikirk, D. Kasilingam, “Infrared and Millimeter Waves”, vol.10 (Academic, Orlando) Chap. 1, page 10. (1983)
- [11] Bernd Michael Fisher, *Broadband THz Time-Domain Spectroscopy of Bimolecules-A Comprehensive Study of the Dielectric Properties of Biomaterials in the Far-Infrared*, <http://www.freidok.uni-freiburg.de/volltexte/2342/>, Chapter 2, section 2, page 24 (2005)
- [12] J. Rudd, D. Mittleman, “Influence of substrate-lens design in terahertz time-domain spectroscopy”, *J. Opt. Soc. Am. B* 19(2) 319, (2002)
- [13] UHJ Jepsen P, Keiding SR, “Radiation patterns from lens-coupled terahertz antennas”, *Opt. Lett.* 20, 807809, 1995
- [14] P. L. Richards, “Bolometers for infrared and millimeter waves”, *J. Appl. Phys.* Vol. 76, No. 1, 1 (1994)

Chapter 3 Terahertz component analysis using metal mesh structure

A structure with periodic square openings curved into the surface of a metal film known as metal mesh was applied in the research described in this chapter. Firstly, spectral characteristics in THz region of such metal mesh structure for which it could be utilized as a sensor in THz sensing spectroscopy are presented in section 1 and 2. Next, several theoretical models for describing the spectral behavior of metal mesh are briefly discussed in section 3.

A series of sensing measurements of human skin samples by applying our metal mesh sensor are presented in section 4. We were exploring to apply this method as a bio-related sensitive terahertz component analysis.

3.1 Metal mesh structure

The 2D metal hole arrays structure (2D-MHA, or it was called as metal mesh in general) has been applied in spectroscopy as an filter element since 1960s. Along with the development of THz technology mentioned in Chapter 1, the idea of a 2D-MHA sensor with its parameters being varied to fit the wavelength in THz region has been brought up.

A metal mesh with square openings was applied in this research, whose image can be found in Figure 3-1.

The parameters of metal mesh shown in Figure 3-1 are as follows:

Grid constant g : 254 μm ;

Aperture length a : 180 μm ;

Thickness t : 60 μm .

We want to point out that these parameters are not precisely the same from piece to piece, because of the process error in the manufacture.

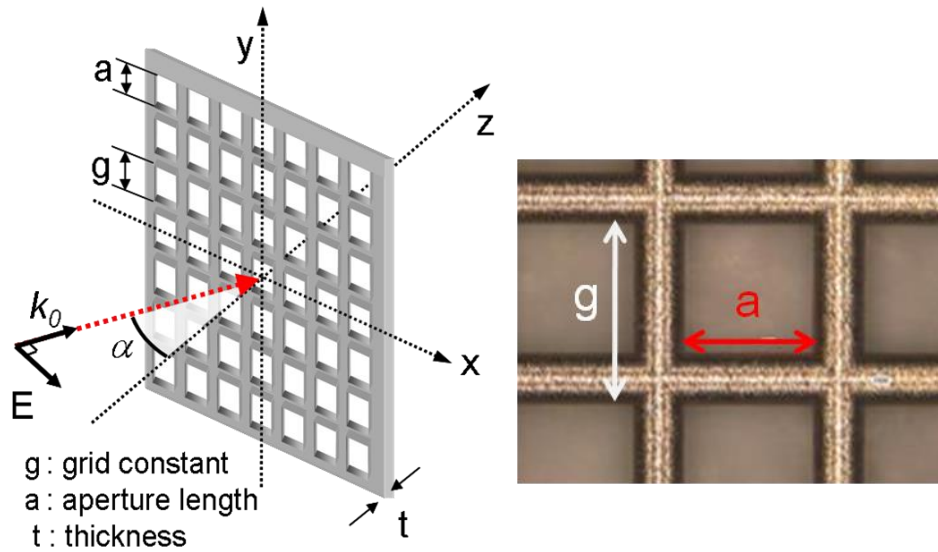


Figure 3-1. Image of metal mesh that we were using in this research work

3.2 Transmission properties of metal mesh

3.2.1 Transmittance enhancement and abnormal decline

Let's firstly consider a rectangle wave guide tube model (Figure 3-2) as the basic unit in a metal mesh's periodic structure.

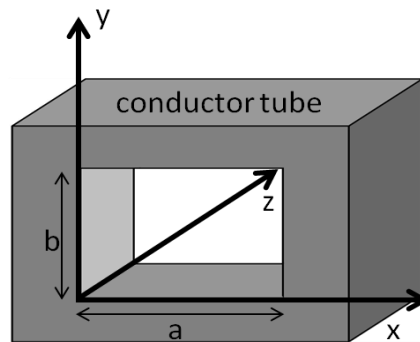


Figure 3-2. A model of rectangle wave guide tube

From the Maxwell equations, the TE wave or TM wave that propagates this wave guide tube has to meet the following Helmholtz formulas.

$$\frac{\partial^2 E_z}{\partial x^2} + \frac{\partial^2 E_z}{\partial y^2} + (k^2 - \gamma^2)E_z = 0, \quad (3-1)$$

$$\frac{\partial^2 H_z}{\partial x^2} + \frac{\partial^2 H_z}{\partial y^2} + (k^2 - \gamma^2)H_z = 0, \quad (3-2)$$

where γ is the propagating constant.

Take the TE wave as an example. According to the separate variable method, these two formulas have the solutions sharing the same form as below:

$$H_z = (A_1 \sin \beta_1 x + A_2 \cos \beta_1 x)(C_1 \sin \beta_2 y + C_2 \cos \beta_2 y) \exp(-i\beta z), \quad (3-3)$$

Based on the boundary conditions, we will have

$$\gamma = \sqrt{k^2 - \left(\frac{m}{a}\pi\right)^2 - \left(\frac{n}{b}\pi\right)^2}, \quad m = 0, 1, 2, \dots \quad n = 0, 1, 2, \dots \quad (3-4)$$

(m and n can't equal to 0 at same time)

If we consider the model of our square opening metal mesh ($a=b$), it is easy to induce from formula (3-4) that:

$$k \geq \frac{\pi}{a}, \quad (3-5)$$

This means a minimum frequency exists that no electromagnetic wave under this frequency can propagate through such wave guide tube, thus it is nominated as “cut-off frequency”. Additionally from a simple calculation for the metal mesh that we were using, this cut-off frequency f_c is around 0.83 THz.

Next, the transmission spectrum of such metal mesh in the real field measured by THz-TDS with transmission geometry is presented in Figure 3-3.

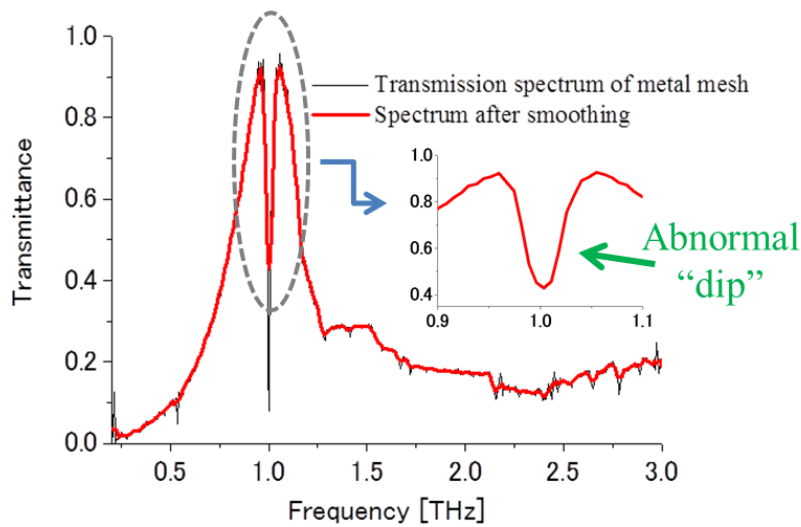


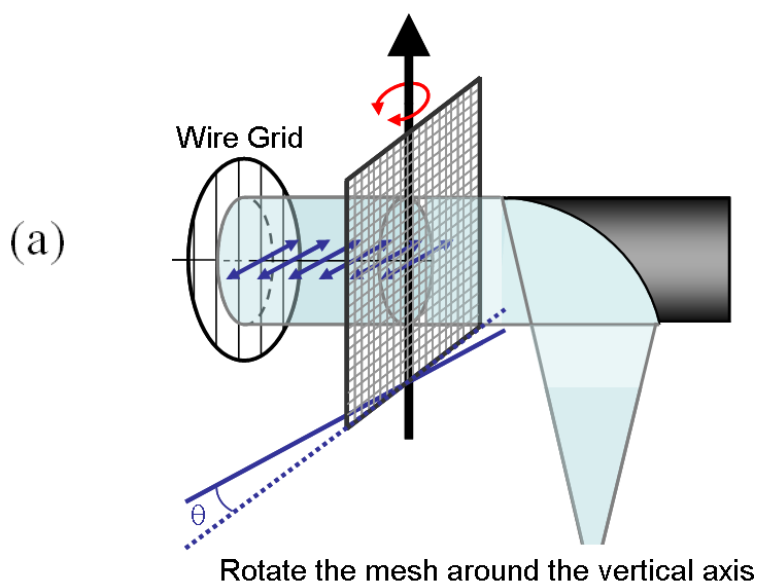
Figure 3-3. Transmittance spectrum of metal mesh

A transmission peak closed to 100% can be observed at the frequency higher than f_c , which is much higher than the opening rate of metal mesh (a^2 / g^2 , around 50%). This transmittance enhancement should be caused by some kind of resonance. A few theoretic models related to this phenomenon are introduced and discussed in section 3.3.

Among the transmission peak, an abnormal transmission feature we called as “dip” can be clearly observed, which is a very sharp decline area can be observed as shown in the inset of Figure 3-3. Like author has mentioned in Chapter 1, this “dip” frequency has the dependence of the surface condition of the metal mesh structure. Compared to the previous measurements of metal mesh in Kawase laboratory, a higher Q value of the dip frequency was achieved due to the condition optimization of the measurements (narrow band and low amplitude among a high transmission peak frequencies; higher the Q value is easier it can be observed). Thus metal mesh has the great potential to be applied as a sensor in THz region. This research work is based on this notion. Although the physical mechanism of the appearance of dip is still not clear, I started my research from the optimization to achieve high Q dip. Several measurements have been carried out for exploring these properties of dip frequency; details can be found in following sections.

3.2.2 Dependence between dip and incident angle of THz wave

These measurements have been carried out by Mr. Yoshida using Backward Wave Oscillator (BWO) setup. The results are shown in Figure 3-4 [1].



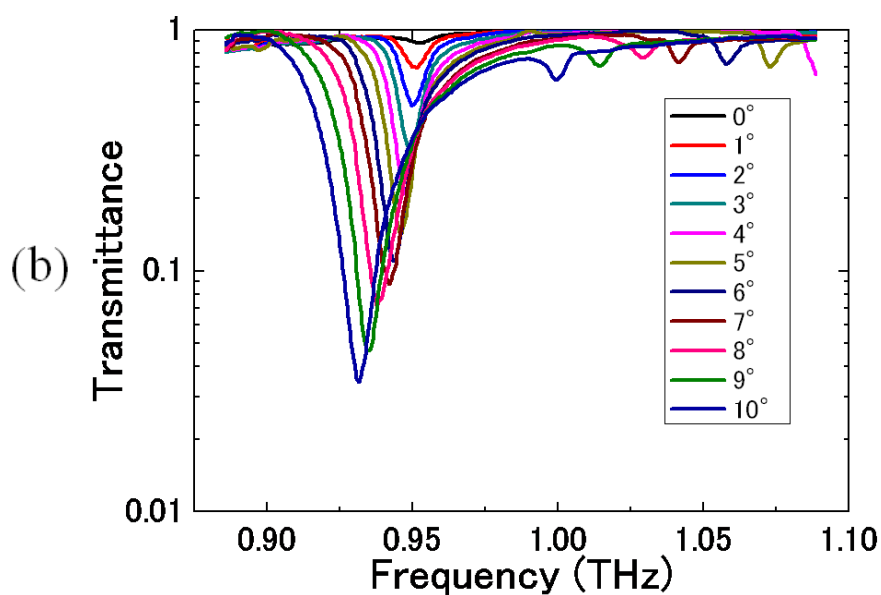


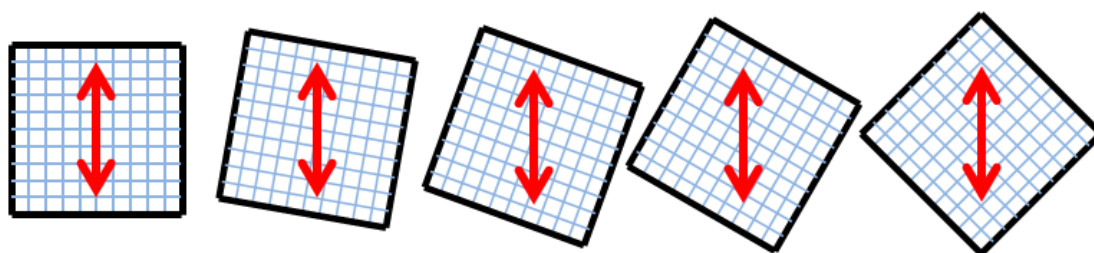
Figure 3-4. (a) The BWO experimental setup for measurement of angle dependence.

(b) Dependence between dip frequency and incident angle of THz wave.

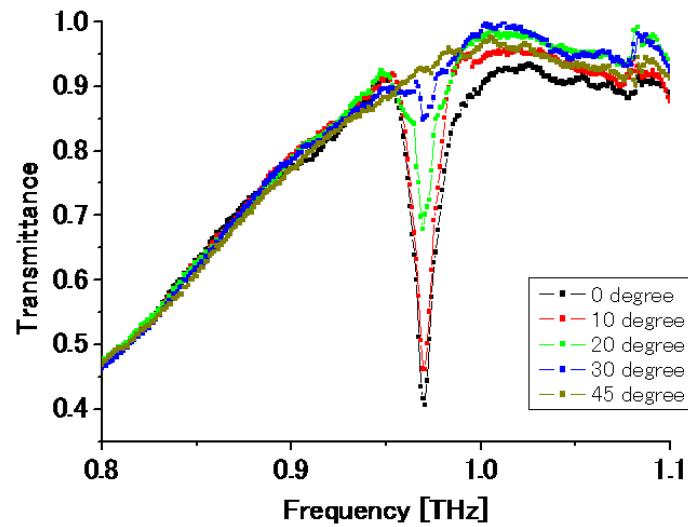
Along with incident angle getting larger, the dip frequency gets lower and the transmittance gets lower as well. The results reveal a practical factor that the incident angle of THz beam should be big enough so that the dip could acquire a high Q value in the sensing measurements.

3.2.3 Dependence between dip and polarization direction of THz wave

Setting incident angle to 4 degrees, we used THz-TDS with transmission geometry mentioned in Chapter 2 with the fixed polarization of THz beam to measure the transmittance of metal mesh while rotating the metal mesh from 0 degree to 45 degrees. Figure 3-5 (a) shows the image of this experiment. And the results can be found in Figure 3-5 (b).



(a)



(b)

Figure 3-5. (a) Rotation of the metal mesh while the polarization of THz beam stays the same.

(b) Dependence between dip frequency and polarization direction of THz wave.

From the results, we can tell that the frequency of dip is actually independent from the polarization direction of incident THz beam; however, polarization greatly impacts on the Q value of the dip, i. e. the amplitude of it. This experiment pointed out that we have to set metal mesh sensor carefully to match the polarization angle for acquiring a high Q value. Based on these results, metal mesh has been set with its grid being orthogonal to the polarization direction of the linear THz radiation generated by experimental setup described in Chapter 2.

3.3 Several theories for transmission spectrum of metal mesh

3.3.1 Surface plasmon polariton

The first theory considered a solution to describe the transmission property of metal mesh is the surface plasmon polariton (SPP) theory. For metal material, the electron groups are moving freely inside the atom grid structure instead of being restricted to a particular atom. However this balance can be broken by the existence of an extrinsic electromagnetic field, such as an incident wave or light. The unbalanced

electron groups and atom also produce the local electromagnetic field contribute to the field on the surface of dielectric metal. This interaction will excite a phenomenon named as surface plasmon polariton that propagates in a wave like fashion along the planar interface between a metal and a dielectric medium, and whose amplitude decays exponentially with increasing distance into each medium from the interface. Thus, a SPP is a surface electromagnetic wave, whose electromagnetic field is confined to the near vicinity of the dielectric-metal interface [2]. Figure 3-6 shows a simplest case of SPP propagation.

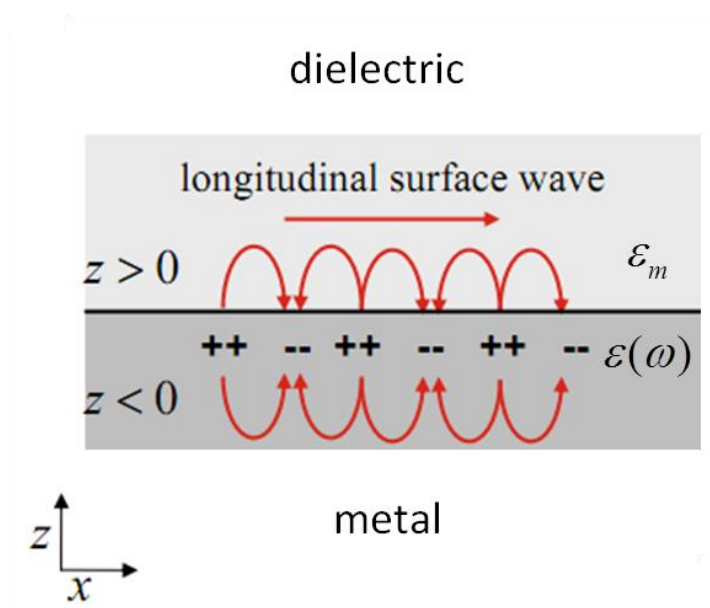


Figure 3-6. Surface Plasmon Polariton on interface of metal-dielectric

According to Maxwell equations and the boundary condition, we can derive the k_{sp} (propagation constant) as the following formula:

$$k_{sp} = \frac{\omega}{c} \sqrt{\frac{\epsilon_m \epsilon(\omega)}{\epsilon_m + \epsilon(\omega)}}, \quad (3-6)$$

This formula describes the distribution curve of k_{sp} shown in Figure 3-7, with two asymptote lines: $k_x = (\omega/c)\sqrt{\epsilon_m}$ when $\omega \rightarrow 0$; $\omega = \omega_p / \sqrt{1 + \epsilon_m}$ when $k_{sp} \rightarrow \infty$.

From this graphic, we can see that the light line has no intersection with the distribution curve which implies that light directly incident onto a flat metal surface can never couple directly to an SP at any finite frequency.

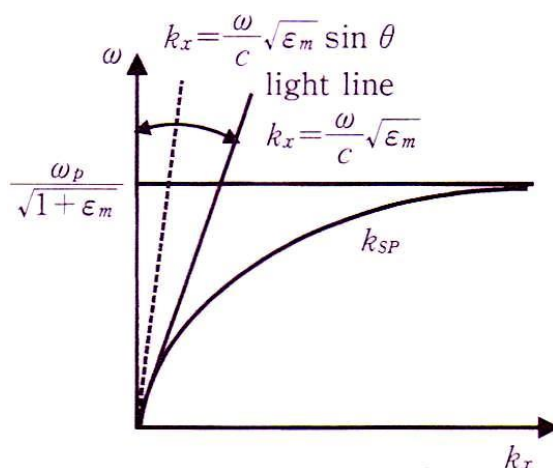


Figure 3-7. Distribution curve of k_{sp}

However, a periodic structure such as the metal mesh or crude surface of metal excites the SPP. Let's consider a 1-D metal mesh with the periodicity of a as an example. The reciprocal lattice can be written as:

$$g_n = (2\pi/a)n, \quad n = 0, \pm 1, \dots \quad (3-7)$$

Thus we can have the new formula for k_{sp} as:

$$k_{sp} = k_{ix} + g_n = \frac{\omega}{c} \sqrt{\epsilon_m} \sin \theta + \frac{2\pi}{a} n, \quad (3-8)$$

New distribution curve is shown in Figure 3-8.

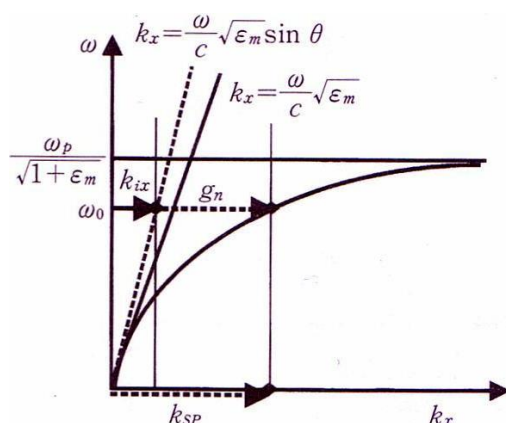


Figure 3-8. Distribution curve of k_{sp} for a 1-D periodic model

The intersection of this curve is the frequency which can excite the SPP on interface. Furthermore, 2-D periodic structure (periodicity in both direction is g , in other words it is a square type) follows the same discipline. We can derive the λ_{spp} as [3]:

$$\lambda_{spp} = \frac{g(\varepsilon_m - \sin^2 \theta)}{\sqrt{(m^2 + n^2)\varepsilon_m - n^2 \sin^2 \theta + m \sin \theta}}, \quad (3-9)$$

However, both simulation results and experimental results have proved that the main transmission peak occurs at the frequency lower than the lowest model of SPP wave.

3.3.2 Diffracted evanescent wave model

A new model in which the transmission is modulated not by coupling to SPs but by interference of diffracted evanescent waves generated by subwavelength features at the surface, leads to transmission suppression as well as enhancement [4]. The image of this model can be found in Figure 3-9.

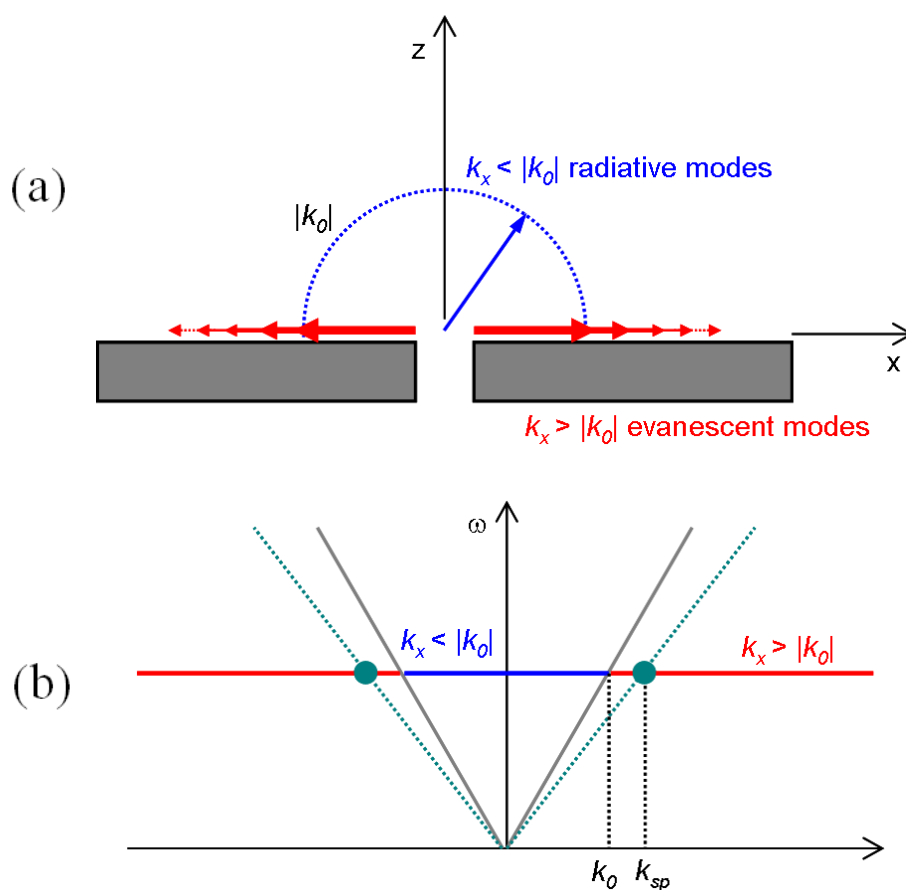


Figure 3-9. Geometry of optical scattering by an opening in a screen in (a) real space and (b) k-space

Assume that electromagnetic wave of frequency $\omega = ck_0 = 2\pi c / \lambda_0$ emerging from a subwavelength aperture (be shown in Figure 3-9 (a)). In the common understanding,

this wave is diffracted into a continuum of radiative (“homogeneous”) modes of which the in-plane component of the wave vector is $k_x \leq k_0$ (blue circle in Figure 3-9 (a) and blue horizontal line in Figure 3-9(b)). However, this new model considers that incident wave also partly diffracted into a continuum of evanescent (“inhomogeneous”) modes propagating along the surface with real $k_x > k_0$ and imaginary $k_z = i(k_x^2 - k_0^2)^{1/2}$ (red arrows in Figure 3-9(a) and red horizontal lines in Figure 3-9 (b)).

As shown in Figure 3-9 (b), the SPP model does exist in such abnormal diffraction, however, the fraction of the total evanescent power coupled into the SP is very low (in other words the SP does not constitute a preferred channel for diffraction compared to the other diffracted lossy modes which are not long-range guided modes of the surface).

For understanding the fundamental characteristics of the total evanescent field diffracted by a subwavelength aperture, we consider the concrete example of light diffracted a single slit of width d in an opaque screen. The electric field amplitude of the total diffracted field at the surface is given by [5]:

$$E(x, z = 0) = -\frac{E_0}{\pi} [Si(k_0(x + \frac{d}{2})) - Si(k_0(x - \frac{d}{2}))], \quad (3-10)$$

For $x > \lambda/2$ we find the formula (3-10) can be approximated by:

$$E(x) = \frac{E_0}{\pi} \frac{d}{x} \cos(k_0 x + \frac{\pi}{2}), \quad (3-11)$$

The total diffracted evanescent field can thus be described as a running wave propagating with a well-defined wave-vector lying in the plane of the surface [4]. The inventor of this model designated this wave as a “composite diffracted evanescent wave” (CDEW), which has the obvious differences from the SPs. The basic characteristics of CDEW are: be launched at any frequency, independently of the presence of neighboring apertures; wave vector equal to the source; amplitude of the CDEW decays with lateral distance as $1/x$; it has an initial phase shift factor compared to wave incident on surface.

This new model was proposed to apply in the nano-aperture structure interacting with visible light. It was proved to be good fit to results of those experiments carried out. On the other hand, I believe that by following its definition of CDEW, this model is probable to be applied in our metal mesh structure (with the size of a few hundred micron meter) interacting with THz wave. An approximation of formula (3-11) can be considered as:

$$E(x) = C(x) \cos(kx + \phi), \quad (3-12)$$

where ϕ is the phase shift with respect to the incident wave; $C(x)$ is a monotonically varying function of distance. An experiment about how grid constant affects the transmission peak of metal mesh was carried out by Dr. Kato (Figure 3-10) [6]. If we construct an interference leading to transmission maxima by formula (3-12), then the interference frequency can be predicted to occur at:

$$m\lambda = L + \frac{\phi}{2\pi} \lambda, \quad (3-13)$$

where L is the distance of evanescent wave traveled to its adjacent aperture.

If we choose $L = \sqrt{2}g$ and $\phi = -\pi/2$, the predicted wavelengths of transmission peaks fit well to the results of Dr. Kato's measurements (Figure 3-11) [6].

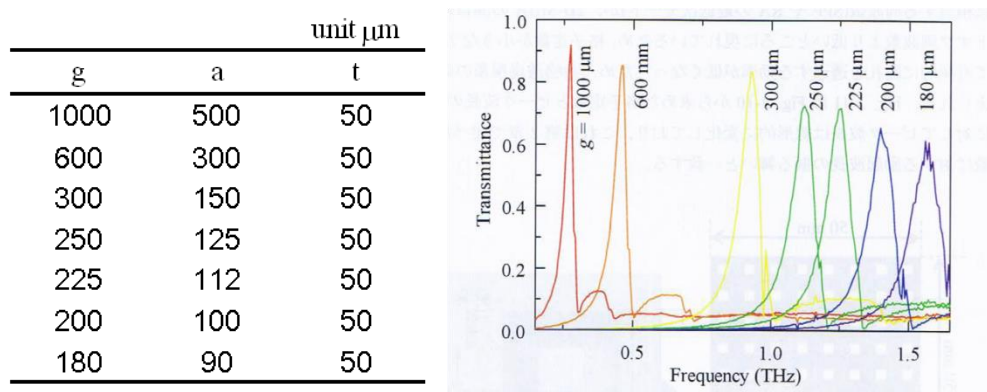


Figure 3-10. Transmittance of metal mesh with different grid constant.

The opening ratio stays the same (25%) by adjusting a parameter

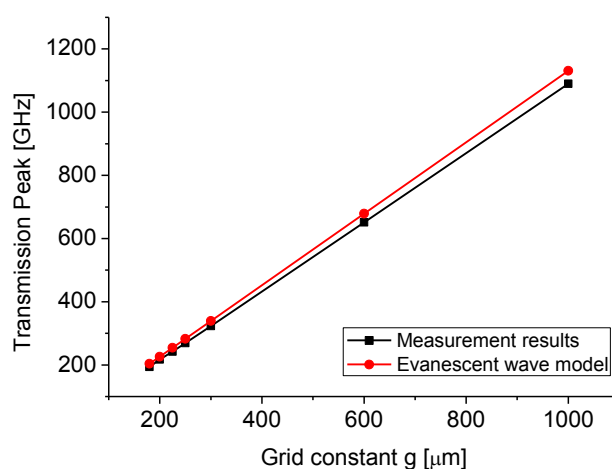


Figure 3-11. Comparison of measurement results and predicted results

This shall imply that the metal mesh's transmission peak occurs because the interference of incident wave and the diffracted evanescent wave launched from the aperture on the cross direction (Figure 3-12).

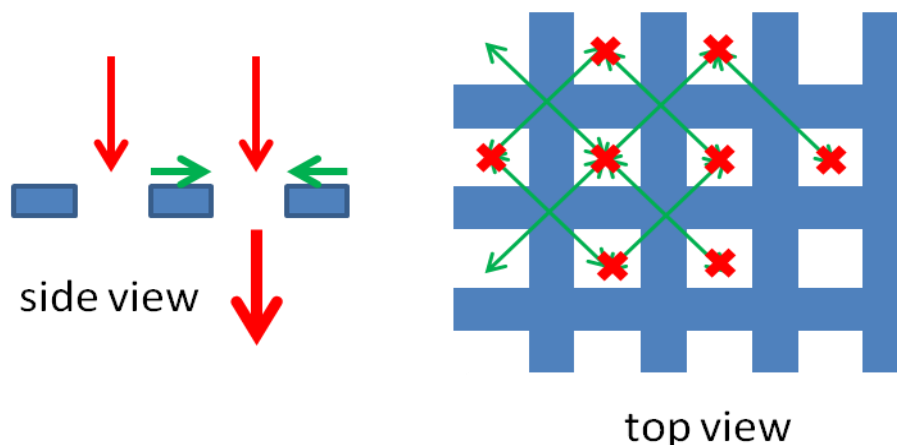


Figure 3-12. A possible interference between the incident wave and diffracted evanescent wave launched from the aperture on the cross direction. One thing to be aware is that the CDEW can diffracted into all directions, and interference on a single aperture is emerged by the incident wave (red vector) and the evanescent waves from multiple cross directions (green vector)

3.3.3 Diffracted interference of adjacent square opening in (1, 1) direction

Few researches have been done to discuss the abnormal dip among in transmission peak of metal mesh. Thus the mechanism of it still remains unrevealed. However due to its high Q value, it could be expected to work as a spectroscopic probe of sensor with a good performance.

In the former study by Mr. Yoshida, a model of diffracted interference of adjacent square opening in (1, 1) direction was proposed to explain the appearance of dip and the dependence between dip and incident angle of THz wave presented in section 3.2.2 [7] (Figure 3-13). It needs to be clear that the model still remains a rough approximate explanation as fitting with the measured results of dip at the moment. The purpose is to verify and predict the appearance tendency of dip, which could give directive guide to our application of metal mesh sensor.

It needs to be emphasized that this diffracted interference model is different from the model presented in Section 3.3.2. The interference emerged in (1, 1) direction is excited by just two diffracted waves: one is excited by the aperture itself; the other is

excited by the aperture in its (-1, -1) direction, not like the model introduced by former section in which it is excited by incident beam at a single aperture and those evanescent waves from all apertures close to it. Thus we can divide periodic apertures of metal mesh by many lines parallel to the line link (0, 0) and (1, 1) on x-y plane.

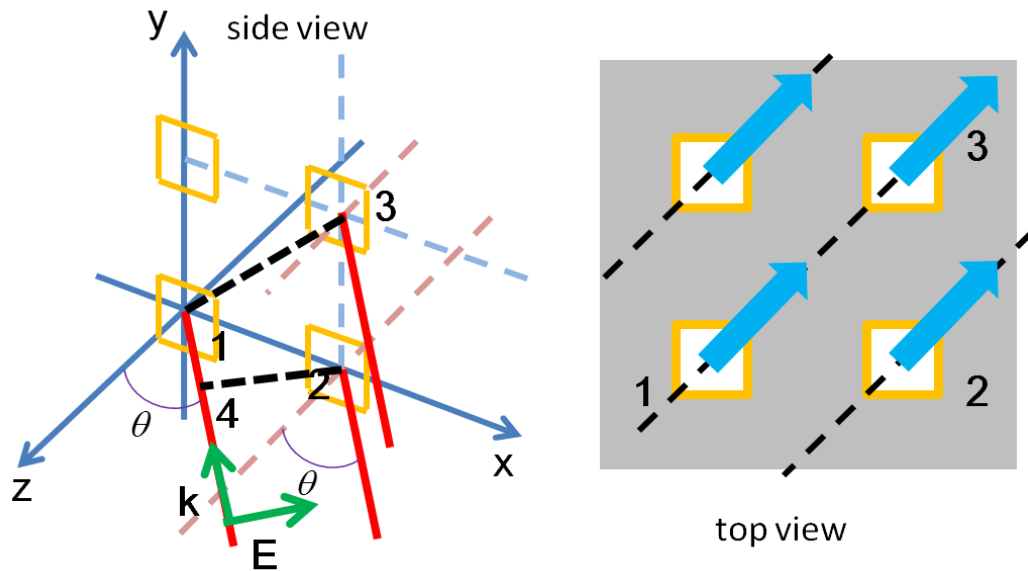


Figure 3-13. Diffracted interference of adjacent square opening in (1, 1) direction of x-y plane.

Phase at point 2, 3, 4 are equal to each other. The diffracted wave excited at one aperture travels through the plane in (1, 1) direction

From this model, we can predict the interference maxima frequency will occur at:

$$g \sin \theta + \sqrt{2}g = m\lambda_{dip}, \quad (3-14)$$

While any frequency meets this formula, an interference maxima wave will appear and propagate along the surface of metal mesh leading to reduction of transmission energy, which explains the sharp decline of dip.

It's not hard to understand the phenomenon that dip shift to lower frequency while the incident angle getting bigger derived from the formula (3-14). About the variation of the Q value, phase matching conditions between adjacent parallel lines are involved (Figure 3-14).

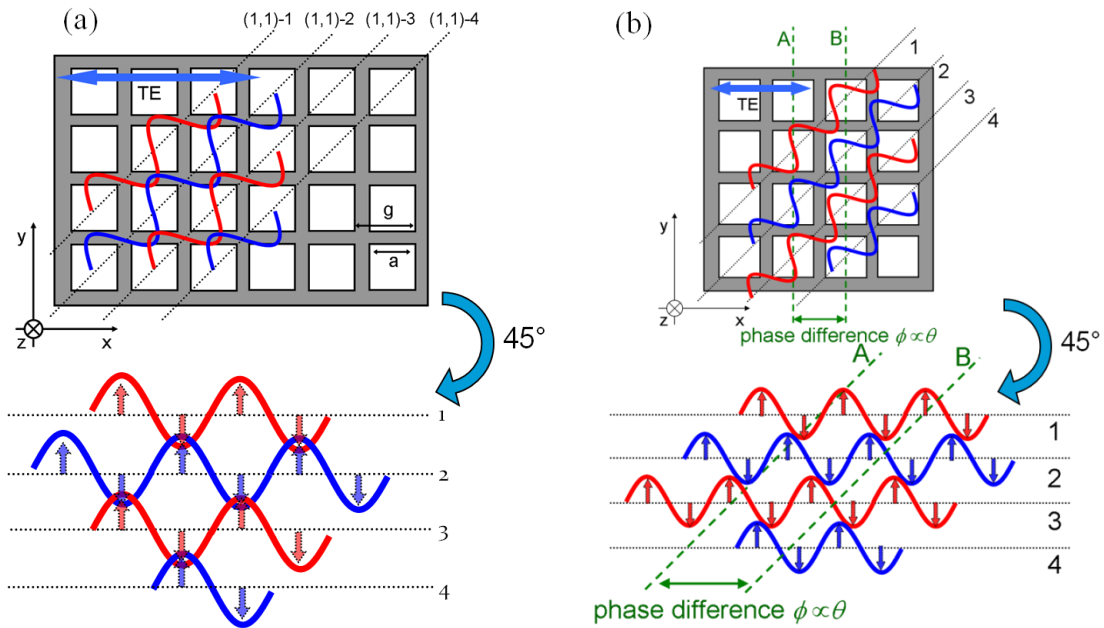


Figure 3-14. (a) Complete phase mismatching condition between two lines of interference.

(b) Alleviation of complete phase matching condition by incidence of oblique wave.

As the vertical incidence of THz wave on metal mesh, four interference lines parallel to each other possess a phase separation of $\pi / 2$ shown in Figure 3-14 (a), this matches the complete phase mismatching condition which leads to no diffracted wave propagation along the surface of mesh, in other word the transmission don't lose energy from in-plane scattering and the dip is disappeared. However, by irradiating oblique wave onto metal mesh, this complete phase mismatching condition will be alleviated so that the dip starts to emerge again.

Although this model could predict the tendency of dip shifting or its Q value depending on the incident THz radiation, it is still difficult to well match the frequency of calculation by formula (3-14) to the results of real measurement or numerical simulation. More inspection of this model is still needed.

3.4 Measurements of the human skin samples using metal mesh sensor

So far, the transmission characteristic of metal mesh structure in THz region and theories for possibly describing its physical foundation as well as its potential to operate

as a sensor have been presented. In the following sections, an example of applying such structure for sensing measurements is described.

3.4.1 Introduction of sample and motivation

Health care of the skin is gaining more and more serious concern in our daily lives, not only to females but also to males. However, the conventional approaches for analyzing skin component usually provide limited information when the amounts of certain component are required [8-10]. Spectroscopy can be considered an efficient method for the measurement of skin sample as electromagnetic waves can be aimed and irradiated onto sample directly and making no human contact of the sample, which in other word nondestructive inspection is possible. Thus the trouble of preparation of the sample is also reduced.

The samples measured in this research work is called stratum corneum (also known as horned layer), which is the outermost layer of the epidermis, consisting of layers of dead cells with lot kinds of functional protein inside them. There is lipid substance among the dead cells [11]. The components of the sample can change related to pathological conditions [12], external environments [13, 14], even aging [15]. The purpose of the stratum corneum is to form a barrier to protect our underlying tissue from infection, dehydration, chemicals and mechanical stress. The thickness of the stratum corneum remains balanced due to a process called desquamation, which describes the cell shedding from the surface of the stratum corneum with new pieces supplied from those in the stratum basale. These cells migrate through the epidermis towards the surface in a journey that takes approximately fourteen days [16].

Cells of the stratum corneum contain a dense network of keratin, a protein that helps keep the skin hydrated by preventing water evaporation. Such cells can also absorb water, further aiding in preventing dehydration, which is the origin of wrinkling of the skin on the fingers and toes of humans and other animals when they are immersed in water for too long. Additionally, this layer can also explain the phenomenon called as “spring back” or a stretchy property of skin due to a weak glutenous protein bond responsible for restore the skin to its natural status. And among the cells of stratum corneum, there are ceramide, fatty acid and cholesterol, which we labeled as the lipid content [16].

The thickness of the stratum corneum varies throughout the body. In general, the stratum corneum contains 15 to 20 layers of dead cells, with the thickness between 10 and 40 μm [16].

The samples provided by the POLA Chemical Industries, Inc. were measured. They were acquired around abdomen from Caucasian females by the EDTA and trypsin treatment [17], which were cut into rectangle pieces with the size around 10 mm \times 10 mm. Before the measurements, samples were kept in containers at zero temperature.

The histologic images of human stratum corneum are shown in Figure 3-15. And the details of these skin layers are shown in Figure 3-16.

As the stratum corneum playing such an important role in human lives, it deserves great attention to be taken care of. Thus, a lot of researches have been conducted for this purpose. Before any further discussion and application of those kinds study, the first step is to get to know the status of it. Although in ideal situation, a real time inspection that directly access from human skin getting rid of the inconvenience of sample collection is the best. The conventional approaches for accomplishing the goal are basing on the chemical analysis, which is a destructive process making it impossible for the analogy of further treatments.

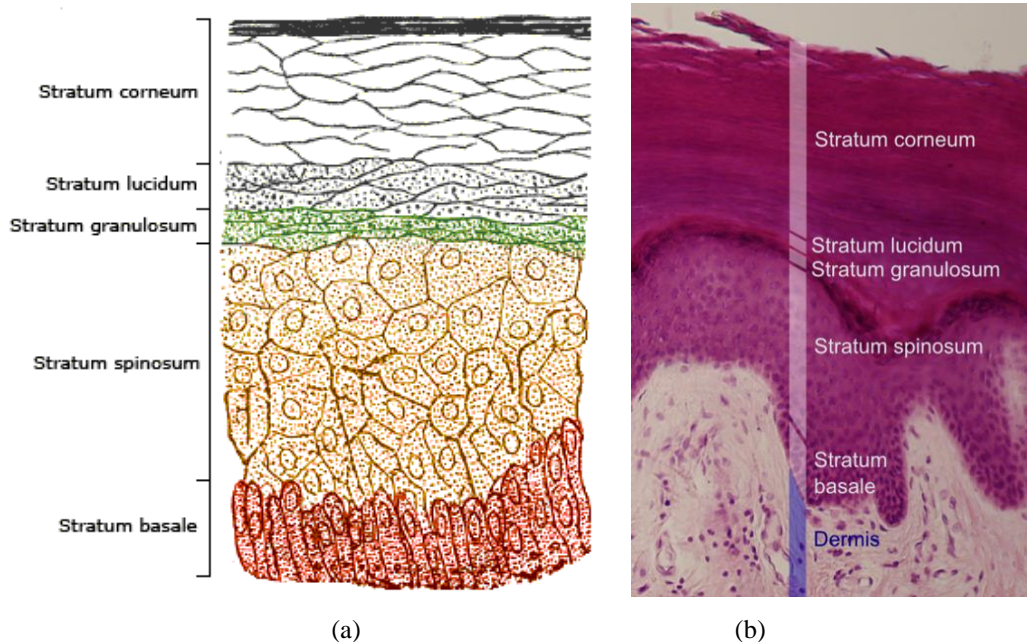


Figure 3-15. (a) Structure image of stratum corneum.

(b) Dyeing image in microscope [16]

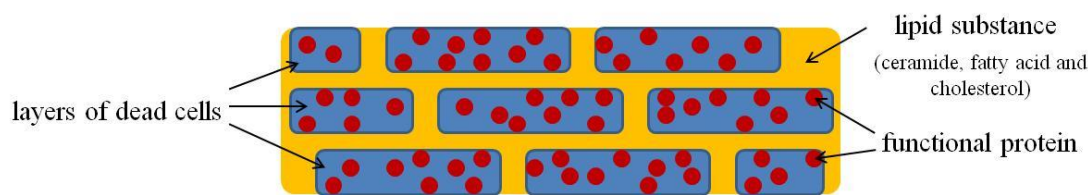


Figure 3-16. Details for the composition of stratum corneum

At this point, our research about THz sensing technology provides another approach for this task. By introducing our metal mesh as a spectroscopic sensor, there is a great potential that the status of stratum corneum can be acquired by the non-destructive inspection.

The objective of measurements in later sections of Chapter 3 is to discuss the feasibility of applying metal mesh sensor for the status inspection of human skin as a trial research to develop a practical non-destructive approach for the analysis of skin component and test of pharmaceutical solution.

3.4.2 Sample preparation

Before any measurements started, we had to attach the sample onto the metal mesh surface as flatly as possible. Firstly, we sank the metal mesh sensor into a container filled with pure water. Then the stratum corneum sheet was taken out from its vessel to be put into the pure water too. It floated in the liquid as it weighs very little. The next step is to aspirate the pure water by a drip pipe extremely slowly keeping stratum corneum sheet staying flat all the time. At last, the sheet would sink and be attached onto the surface of metal mesh sensor smoothly and tightly. It shall be emphasized that the aspiration process must be carried out carefully to assure the flatness of sample sheet the whole time. It usually took about 20 minutes to complete this step. A simple drawing presented in Figure 3-17, shows the general idea of it.

It was necessary to leave the metal mesh sensor with the sample sheet to stand for 30 minutes till it reached the complete nature drying. Figure 3-18 shows one image of metal mesh sensor attached with sample.

Being a sensor, we used the abnormal decline area in the transmittance spectra of metal mesh, mentioned in former section of Chapter 3 as “dip” for a “probe” to express the variation of objects. Although the metal meshes used in this research work were all

manufactured in same size, the “dip” range however came with some tiny difference from piece to piece. To set a comparable reference line for stratum corneum, we measured transmittance spectrum from different parts of a particular metal mesh. The metal mesh in this measurement was divided into four parts shown in Figure 3-19.

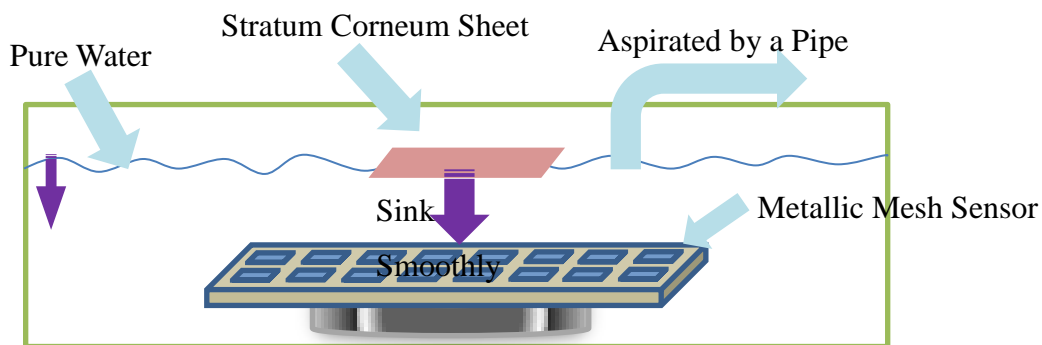


Figure 3-17. The aspiration of pure water to make skin sheet sank onto metal mesh sensor



Figure 3-18. Image of metal mesh sensor attached with sample

Part 1 and part 2 were the bare metal structure covering by no sample. Our THz-TDS with transmission geometry setup was applied. The parallel THz beam was restricted by an aperture with 7 mm diameter. The incident angle of metal mesh surface which was mentioned in Chapter 3 was 4 degrees. The transmittance spectrum was acquired shown in Figure 3-20.

We could tell from Figure 3-20 that the dip frequency fit close to each other, implying the surface flatness of metal mesh was adequately good. Thus, we considered these dip lines acquired by bare metal surface as basic reference line when the later

measurements were carried out by using the same metal mesh sensor.

The transmittance spectrum of stratum corneum on part 4 of metal mesh sensor was measured later. Result was shown in Figure 3-21 with the red line representing the subject status. We could observe that dip experienced a shift to low frequency domain

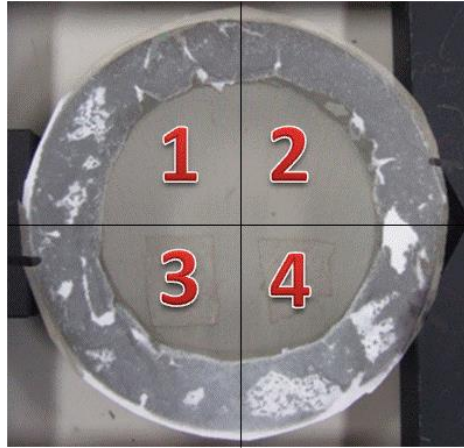


Figure 3-19. Real image of a particular piece of metal mesh labeled as metal mesh

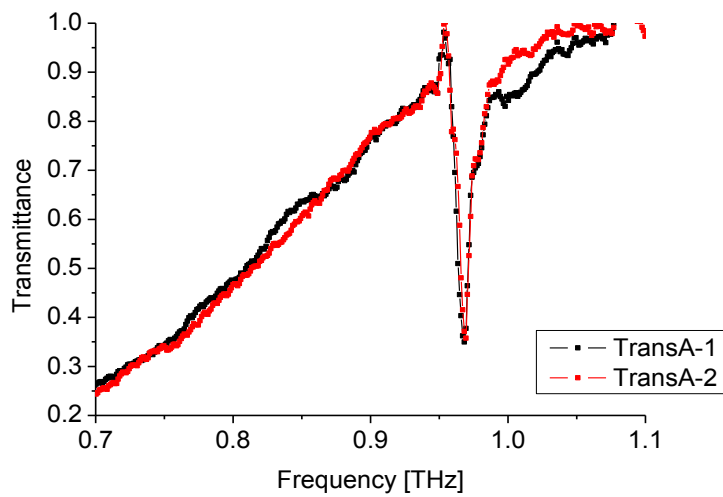


Figure 3-20. Transmittance spectrum measured by through part 1 and part 2 of metal mesh

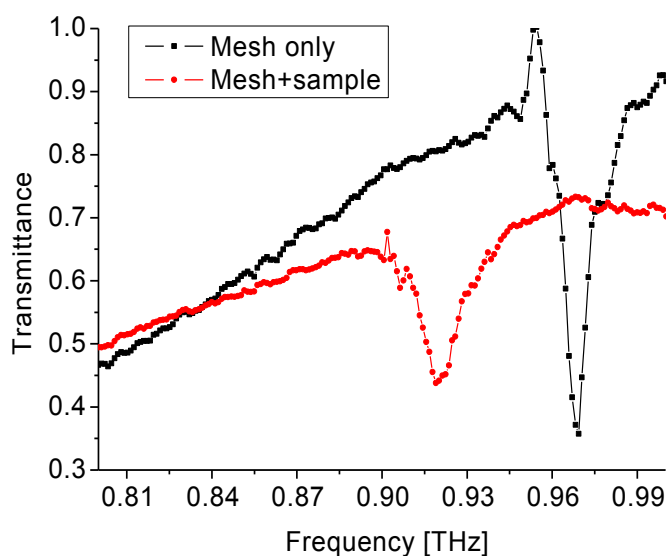


Figure 3-21. Transmittance spectrum measured after sample was attached onto metal mesh sensor

3.4.3 Lipid substance sensing measurements

As it has been mentioned in former section, there are ceramide, fatty acid and cholesterol, which we labeled as the lipid content among cells of stratum corneum. These organic substances are easily soluble in some organic solvent, such as a mixture of chloroform and methanol used in this research work.

Chloroform is an organic compound with formula CHCl_3 . It is one of the four chloromethane with the natures of colorless, sweet-smelling, dense liquid, and is considered somewhat hazardous. It is a common solvent in the laboratory because it is relatively unreactive, miscible with most organic liquids, and conveniently volatile [18]. Figure 3-22 shows its chemical formula and image of liquid state in a test tube.

This section reports several measurements to track variation of lipid content by using our metal mesh sensor in THz region.

The reference line of bare metal surface and the basic line of sample sheet were measured firstly. Then we dropped 1 mL chloroform methanol solution onto the stratum corneum to dissolve the lipid content among cells and fallen into a container below together. About 15 minutes was spared to let the chloroform methanol remained on metal mesh volatilize completely. Then we measured transmittance spectrum of sample sheet again.

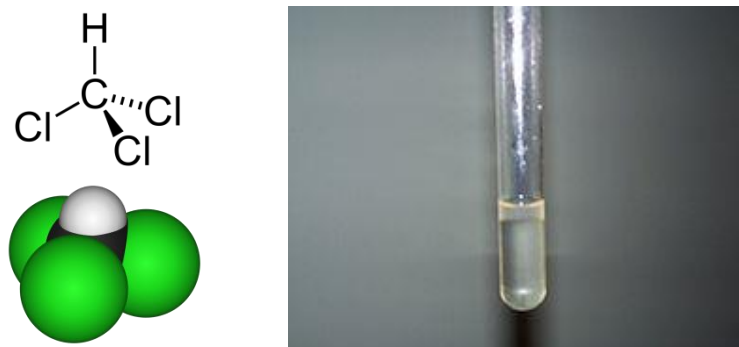


Figure 3-22. Formula of chloroform and its liquid state in a test tube

These experiments have been carried out several times by different pieces of metal mesh with stratum corneum attached. For the reliability of reference line, we also measured the transmittance spectra of bare mesh treated by chloroform methanol as shown in Figure 3-23. In this thesis, two typical results among them are presented. Figure 3-24 (a) shows the data of metal mesh A and Figure 3-24 (b) shows the data of another metal mesh marked as B.

A shift to high frequency domain after the treatment can be confirmed from both data of metal mesh A and metal mesh B as being presented. For further proof that support these dip shifting were caused by variation of lipid content, several more experiments were designed to proceed.

We prepared a mixture solution which formed by the same components as the lipid in human stratum corneum (ceramide, fatty acid and cholesterol). At first, a 10 μL of such mixture was supplied back to stratum corneum sheet by a Pasteur pipette, then another 15 μL was resupplied next, which made a 25 μL of this mixture added to sample totally. One important thing to be mentioned is that the lipid resupplied back was not dropped directly onto the sample sheet but flowed from up down by gravity, thus there definitely were no 100% absorption inside or concreting on surface of sample (size around 10 mm \times 10 mm, the lipid actually resupplied back was quite a small amount as most of it just flowed away). Figure 3-25 explains this process visually.

At last we removed lipid that has been resupplied by treating samples with chloroform methanol again. Transmittance spectrums were acquired right after every procedure respectively. We expected that dip should shift back to original position (the red lines shown in Figure 3-24) with the lipid resupplied, and then return to fit the

spectrum of first-time treatment (the green lines shown in Figure 3-24). These procedures were put into practice repeatedly with different metal meshes on different days. This thesis presented one of them by using the metal mesh sensor B, shown in Figure 3-26.

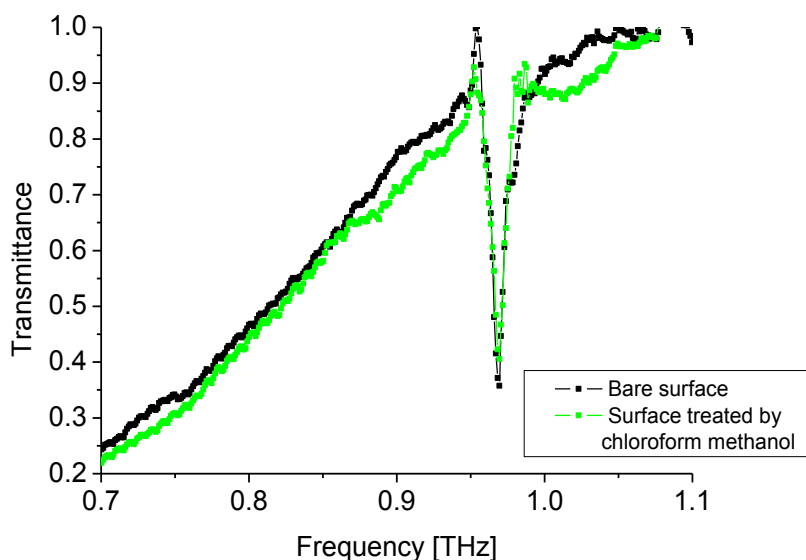
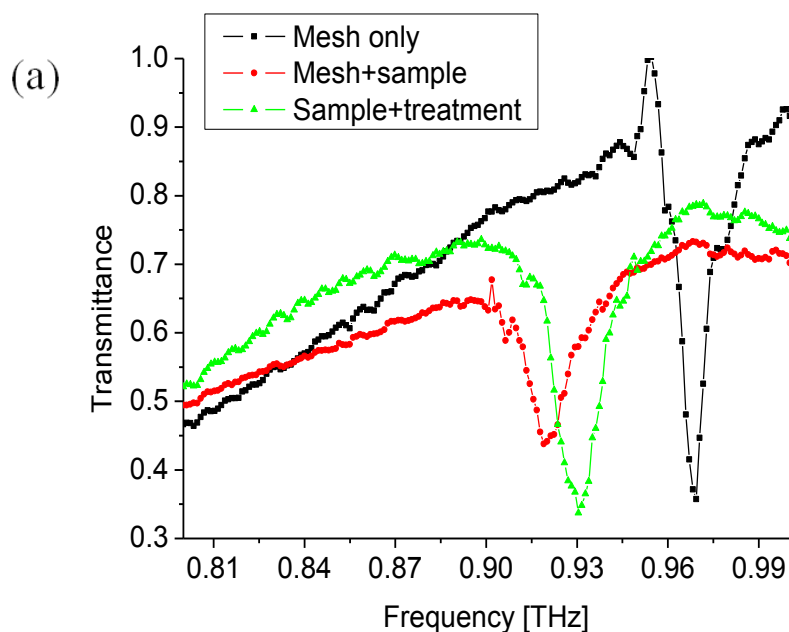


Figure 3-23. Metal mesh treated by chloroform methanol. We can tell that the mixture solution doesn't affect metal thus the dip stays the same frequency



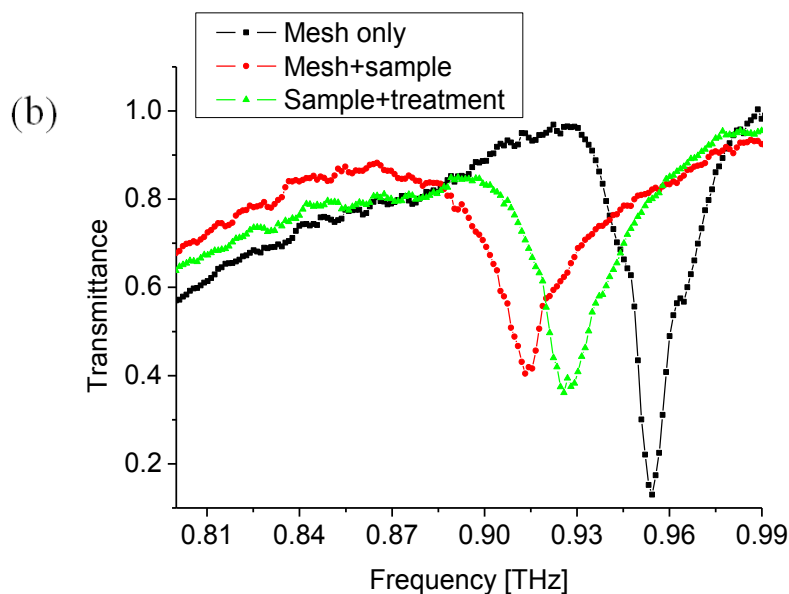


Figure 3-24. (a) Transmittance spectrum of sample treated by chloroform methanol, metal mesh A

(b) Transmittance spectrum of sample treated by chloroform methanol, metal mesh B

The result was highly approximated to our expectation, only except that dip of sample re-treated by chloroform methanol shifted to high frequency domain exceed that of first-time treatment (dip shifting between purple line and green line shown in Figure 3-26). Same exceeding phenomenon has been occurred with repeatability by using other metal mesh. Although it still didn't come out with a precise explanation, I suppose the reason may lie in that our treatment caused the disorder of cells structure to make stratum corneum sheet a little thinner.

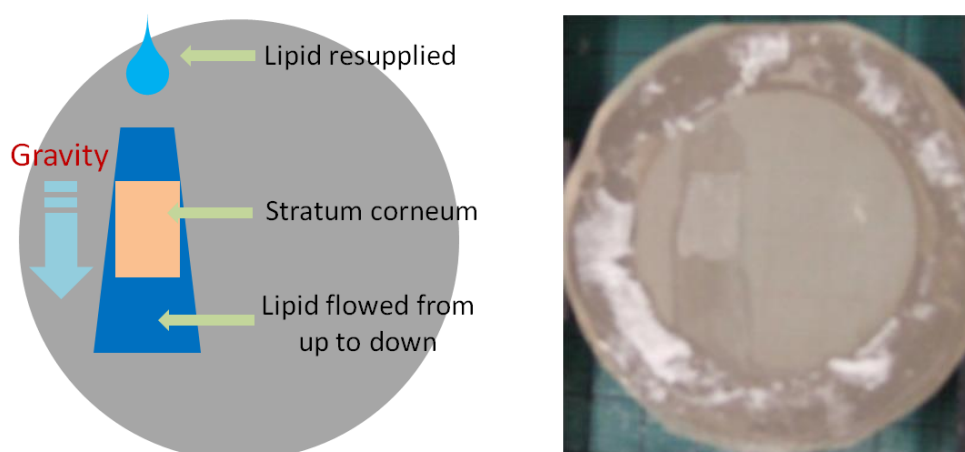


Figure 3-25. The process of resupplying lipid back to sample. We can see from images above, a lot of lipid solution was just flown by the sample sheet down to the container below.

This section has explained that our metal mesh sensor in THz region is possible to sense tiny variation of lipid content in human stratum corneum (sensitivity is up to detect the difference of less than 10 μL). In other words, we can distinguish the samples with or without the lipid content by transmittance spectrum, which makes it possible to carry out the measurements in next section.

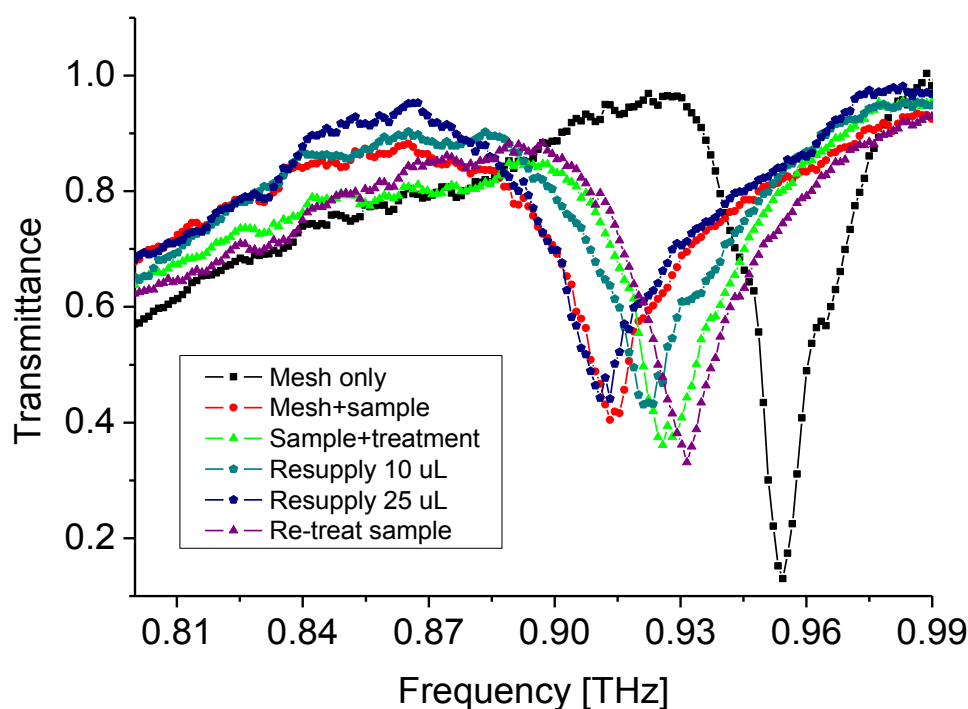


Figure 3-26. Transmittance spectra of resupplying lipid back to sample and re-treat it later

3.4.4 Protein denaturation sensing measurements

As mentioned in former section, several kinds of protein substances play essential function as well as make up great components of stratum corneum. An investigation of protein denaturation was conducted and reported in this section.

Denaturation is a process in which proteins lose its tertiary structure and secondary structure which is present in their native state. Denatured proteins can exhibit a widely range of characteristics including becoming not functional.

A common way to cause denaturation process is heating. We carried out the heating experiments as shown in Figure 3-27(a) and Figure 3-27(b) shows the transmittance spectrums of stratum corneum after being heated to 80° for 30 seconds by

a low-power dryer. This temperature is high enough to make protein denaturation as well as keeping the sample not scorch.

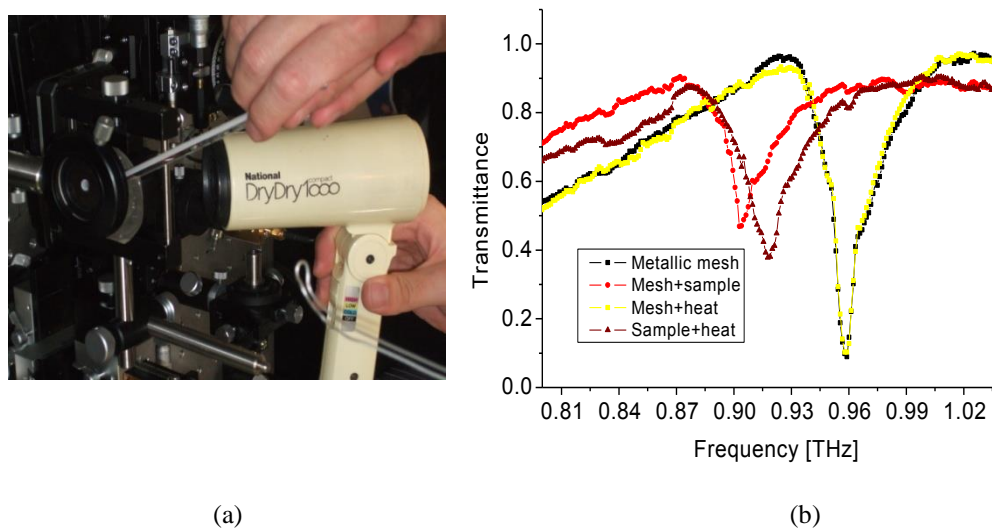


Figure 3-27. (a) Heating the sample attached onto metal mesh sensor
(b) Transmittance spectrums of sample after heating

The transmittance spectrum of heating bare metal mesh perfectly fit to the original reference spectrum (light yellow line fit to the black line in Figure 3-26 (b)). Thus, the shift of spectrums should be caused by the variation of sample. For further confirmation of its essence, we listed several possible reasons by considering constituents of stratum corneum:

- (1) Heating cause the variation of lipid content
- (2) Heating cause the variation of water content
- (3) Heating cause the variation of protein content

In section 3.4.3, we have cleared that our metal mesh sensor can inspect and verify samples without lipid content. We continued the measurements of transmittance by heating those samples. After complete cooling off, we resupplied 10 μL of pure water by the method same as how we resupplied the lipid content back to stratum corneum. It has to be emphasize again that the pure water flowed from up to down, only a small amount of it had been absorbed by samples. After that we left sample standing for about ten minutes waiting for evaporation to be done. Transmittance spectrums measured right

after every procedure respectively. Results are exhibited in Figure 3-28.

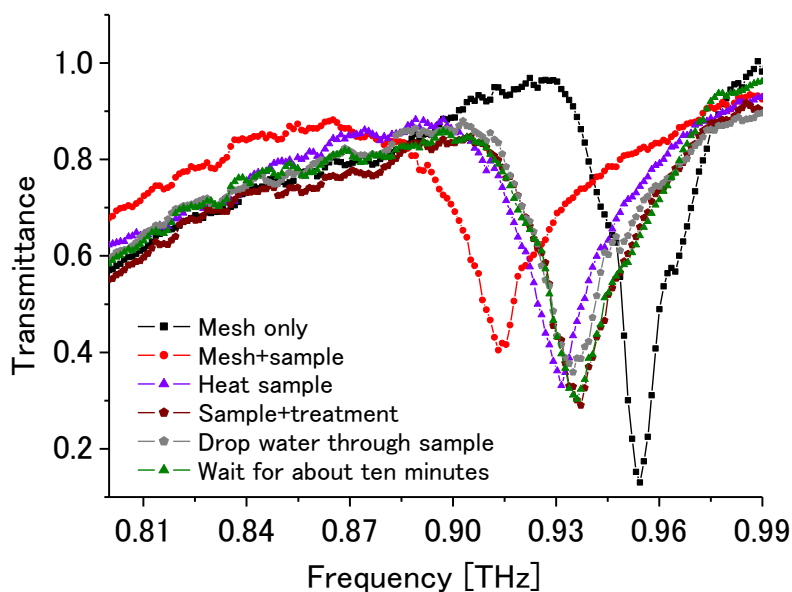


Figure 3-28. Transmittance spectra for heating the sample without lipid content and resupplied with pure water

Results show dip shift to high frequency after heating the sample, and resupply of pure water made dip shifting to low frequency by a tiny distance. It suggested that the possible reason one in the list can be ruled out which means this dip shifting is not caused by variation of lipid content, as well as that the water content has very limited effect of causing it. Another experiment's results also supported my point well, which can be found in Figure 3-29.

We used sample whose transmittance spectrums after heating has been shown in Figure 3-27 (b) to carry out a series of measurements. Firstly 10 μL of pure water were dropped and flowed through sample and then treatment of chloroform methanol similar in section 3.4.3 was applied. At last lipid content was resupplied.

Both Figure 3-28 and 3-29 point out that dip shifting after heating samples do not caused by evaporation of water content or variation of lipid content during the temperature getting to higher level. These proofs could be strongly supported that protein denaturation is possible to be observed using our metal mesh sensor.

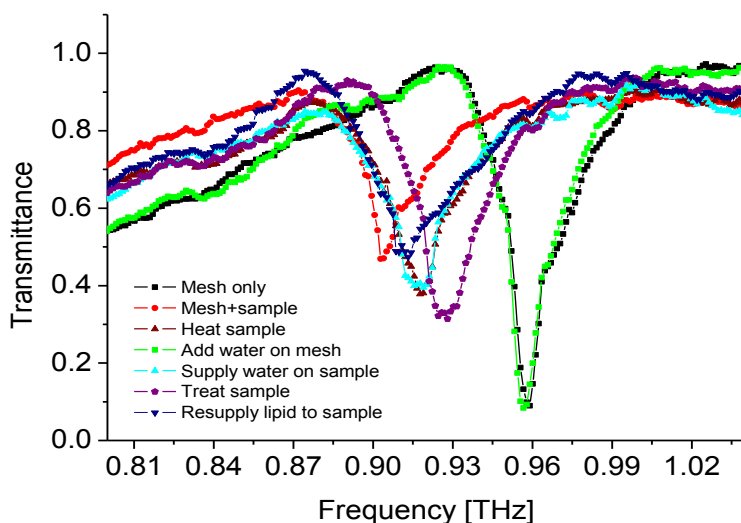


Figure 3-29. Transmittance spectra for resupply water to sample which has been heated firstly and then do the treatment

Although the heating process experiments went on fine, we acquired some results from another denaturation experiment that were not very “clear”, in which the skin sample on metal mesh A was applied. Instead of heating, we sank the sample into a denaturation solution (mixed with dithiothreitol and guanidine hydrochloride) after lipid content removed to make protein denatured.

Influence of denaturation solution on bare metal mesh was investigated as shown in Figure 3-30. Dip of sensor did not shift after sinking into our mixture.

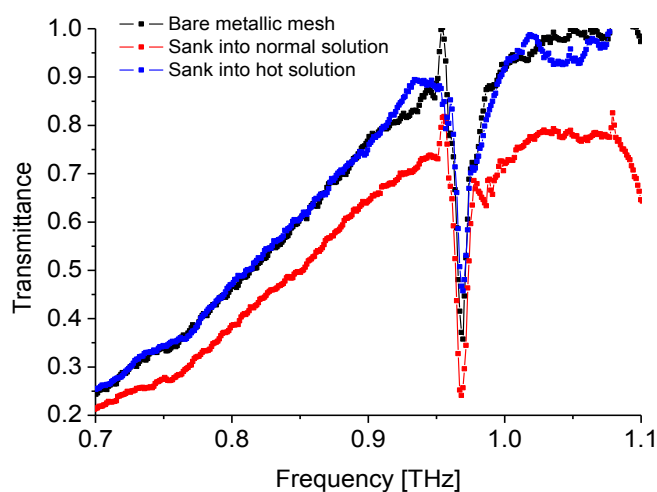


Figure 3-30. Transmittance spectra of bare metal mesh taken out from denaturation solution and restore its dryness.

Then the part of metal mesh attached with sample was sunk into the solution at room temperature. After record its transmittance spectrum, it was sunk into the same solution which heated to around 80 °C then we carried out the measurement again (For the record, we left sensor restore its dryness before every measurement.).

We expected the same shifting of dip could be acquired as the heating experiment to support our point (we can rule out the factors of lipid content and moisture condition), however the results show that no shifting of dip can be observed after sinking sample into solution at room temperature. Dip did shift as heating experiment when sample was sunk into mixture at around 80 °C. These results can be found in Figure 3-31.

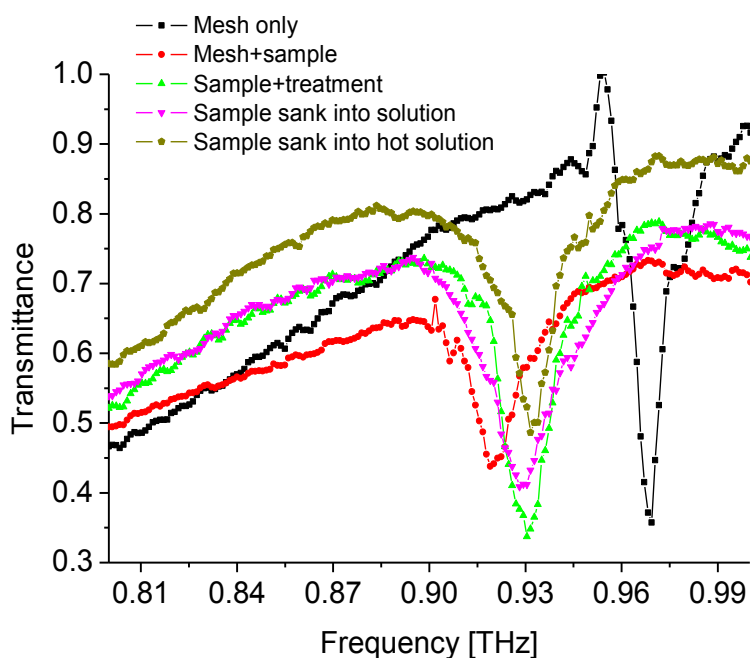


Figure 3-31. Results of protein denaturation caused by a mixture solution at room temperature and heated to 80 degrees Celsius.

3.5 Summary

This chapter firstly presented the image of metal mesh that we were using, and then reported the incident angle dependence as well as polarization dependence of the abnormal decline band distinguished as “dip” in its transmission spectrum. Several theoretic hypothesis including Surface Plasmon Polariton (SPP), the Composite Diffracted Evanescent Wave theory, that trying to explain the transmission property of

metal mesh were introduced. Although there was no decisive conclusion to the explanation of transmission property especially the appearance of dip frequency, we believed that the diffracted evanescent wave theory holds the key to the answer of this task.

Next, a series of measurements of human skin (stratum corneum) by applying a THz sensing method using metal mesh were introduced. We confirmed that variation of lipid content in stratum corneum sample could be observed sensitively. The protein denaturation was also traceable by using our THz sensor. As a result, we can say that our THz sensing method using metal mesh is a practicable and sensitive spectral analysis for human skin measurements, which may lead to many bio-relevant applications.

Reference

- [1] 吉田茂樹, 金属二次元周期構造を用いた高感度テラヘルツセンサーの開発, 第三章 メタルメッシュの透過特性、P35 (2009)
- [2] Anatoly V. Zayats, Igor I. Smolyaninov, Alexei A. Maradudin, Nano-optics of surface plasmon polaritons, *Physics Reports* 408 (2005) 131-314 (2004)
- [3] 吉田茂樹, 金属二次元周期構造を用いた高感度テラヘルツセンサーの開発, 第二章 理論的背景、P16 (2009)
- [4] Henri J. Lezec and Tineke Thio, Diffracted evanescent wave model for enhanced and suppressed optical transmission through subwavelength hole arrays, *Optics Express*, Vol. 12, No.16, pp. 3629- 3638,(2004)
- [5] M. K. Kowarz, “Homogeneous and evanescent contributions in scalar near-field diffraction”, *Appl. Opt.* 34, 3055-3063 (1995)
- [6] 加藤英志、テラヘルツ波による金属二次元開口アレイを用いたセンシングに関する研究、第三章 金属2次元開口アレイ（2D-MHA）の透過特性、P37-38 (2010)
- [7] 吉田茂樹, 金属二次元周期構造を用いた高感度テラヘルツセンサーの開発, 第四章 メタルメッシュの透過スペクトルに現れるディップに関する考察、P58 (2009)
- [8] PJ Aspers, GW Lucassen, EA Carter, HA Bruining, GJ Puppels, “In vivo confocal Raman microspectroscopy of the skin: noninvasive determination of molecular concentration profiles”, *J Invest Dermatol*, 116, pp.434–442 (2001)
- [9] R Voegeli, J Heiland, S Doppler, AV Rawlings, T Schreier, “Efficient and simple quantification of stratum corneum proteins on tape strippings by infrared densitometry”, *Skin Res Technology*, 13, pp. 242–251 (2007)
- [10] M Yamaguchi, Y Tahara, T Makino, T Shimizu, A Date, “Comparison of cathepsin L activity in cheek and forearm stratum corneum in young female adults”, *Skin Res Technology*, 15, pp. 370–375 (2009)
- [11] AV Rawlings, “Trends in stratum corneum research and the management of dry skin conditions”, *Int J Cosmet Sci*, 25, pp. 63–95 (2003)
- [12] Di Nardo A, P. Wertz, A. Giannetti, S. Seidenari, “Ceramide and cholesterol composition of the skin of patients with atopic dermatitis”, *Acta Derm Venereol*, 78, pp. 27–30 (1998)

- [13] R.J. Rycroft, W.D. Smith, “Low humidity occupational dermatoses”, *Contact Dermatitis*, 6, pp. 488–492 (1980)
- [14] E.J. Kim, X.J. Jin, Y.K. Kim et al. “UV decreases the synthesis of free fatty acids and triglycerides in the epidermis of human skin in vivo, contributing to development of skin photoaging”, *J Dermatol Sci*, 57, pp. 19–26 (2010)
- [15] H. Tagami, “Functional characteristics of the stratum corneum in photoaged skin in comparison with those found in intrinsic aging”, *Arch Dermatol Res*, 300, pp. S1–S6 (2008)
- [16] P. Ovaere, S. Lippens, P. Vandenabeele, W. Declercq, “The emerging roles of serine protease cascades in the epidermis”, *Trends in Biochemical Sciences*, vol. 34, pp. 453-463 (2009)
- [17] A.P. Lavrijsen, J.A. Bouwstra, G.S. Gooris, A. Weerheim, H.E. Bodde, M. Ponc, “Reduced skin barrier function parallels abnormal stratum corneum lipid organization in patients with lamellar ichthyosis”, *J Invest Dermatol*, 105, pp. 619-24 (1995)
- [18] Rossberg, M. *et al.* “Chlorinated hydrocarbons” in *Ullmann’s Encyclopedia of Industrial Chemistry* (2006)

Chapter 4 Identification over obstacles using terahertz tags/barcodes

In this chapter, the application of identification over obstacles by applying terahertz technique is explored. We started this research work by the development of a novel design of surface metal antenna. Although plenty of time has been invested to improve such design, the drawbacks of surface metal antenna are still inevitable. Followed by that, we present a concealed terahertz barcode/chipless tag to achieve remote identification through an obstructing material using terahertz radiation. We show scanned terahertz reflection spectral images of barcodes concealed by a thick obstacle. A concealed and double-side printed terahertz barcode structure is proposed, and we demonstrate that our design has better performance in definition than a single-side printed barcode using terahertz time-domain spectroscopy. This technique combines the benefits of a chipless tag to read encoded information covered by an optically opaque material with low cost and a simple fabrication process. Simulations are also described, along with an explanation of the principle of the terahertz barcode identification system.

4.1 Introduction of background and motivation

Techniques for identification and recognition have progressed significantly over the past century, bringing considerable convenience to our daily lives. Many efforts have been made to improve the accuracy, cost, and simplicity of these techniques. The most widely used systems include radio-frequency identification (RFID) [1], the barcode [2], and more recently, the quick-response (QR) code [3]. The principle of these techniques is communication via reflected electromagnetic waves from encoded elements [4]; however none of these techniques meet the rapidly developing need for industrial applications because barcodes and QR codes only operate at visible wavelengths, which have security implications as well as negative impacts on the aesthetics of the products they identify. Although RFID is suitable for remote operation via a tag that can be concealed and does

not require direct human interaction, implementation is expensive and has environmental issues because of the metals and semiconductors used. There has been some recent progress in developing chipless RFID tags to reduce the cost [5–11]; these solutions essentially entail placing a metal structure on substrate, allowing a spectral response at a few gigahertz. Thus, challenges remain in terms of the complicated design of RFID tags and problems with counting multiple samples because the responses of tags can overlap when they are close in proximity due to scattering of the beam. An interesting chipless alternative is found by a French research group and called as terahertz identification (THID) tags [12, 13], which are based on the spectral response of the interference from a multi-layer structure. Currently, however, the quantity of information that can be stored using THID is low.

Terahertz (THz) radiation can penetrate many commonly used packaging materials, making it suitable for nondestructive and noninvasive inspection and imaging [14–16]. Compared to the X-ray techniques, it has no harm to human being and a moderate transmission to see through soft material; Compared to millimeter wave, it has much less scattering and better directivity due to the relatively smaller wavelength. Thus, we believe that it can be considered to have great potential in the application field of identification. The problem remains by how we could design the carrier for efficiently coding the information. In the following sections, results regarding to the design and choice of information carrier are presented and discussed.

4.2 Surface metal antenna array

4.2.1 Definition

Firstly, an artificial metal structure has been considered as the carrier for coding the information. “Surface metal antenna array” in this paper is the structure of periodic metal elements being embedded onto a planar dielectric substrate. More popular name for it is the metafilm or the planar metamaterials, which is a remarkable and rapidly developing research topic ever since the first simultaneous demonstration of it for performing as “left-handed” medium [17-18]. The metamaterials typically represent a family of artificial composite materials which is formed by identical conductive elements (mostly being made by metal with sub-wavelength dimensions) periodically

being coated within or on top of the dielectric substrate. They can provide exotic response when interact with electromagnetic waves according to their specific designs, such as negative refractive index [19], perfect focusing [20-21], and invisibility cloaking [22-23]. The rising of metamaterials science gave THz research great push for the reason that it offered an alternative path for the researchers who were troubled by the lacking of elements or materials which can have desirable response in the THz region [24]. A lot of the papers have been published regarding the applications by applying metamaterials in the field such as modulators, high-performance filters, and sensors [25-30]

The tunability of resonance frequency for a metamaterial structure, or specific the planar metamaterials (surface metal antenna array in this paper) is achieved by the design of the element's structure and the material of substrate. For our purpose, a proper designed antenna with characteristic spectrum could be used to carry information. One example of such coding process is briefly described in Figure 4-1.

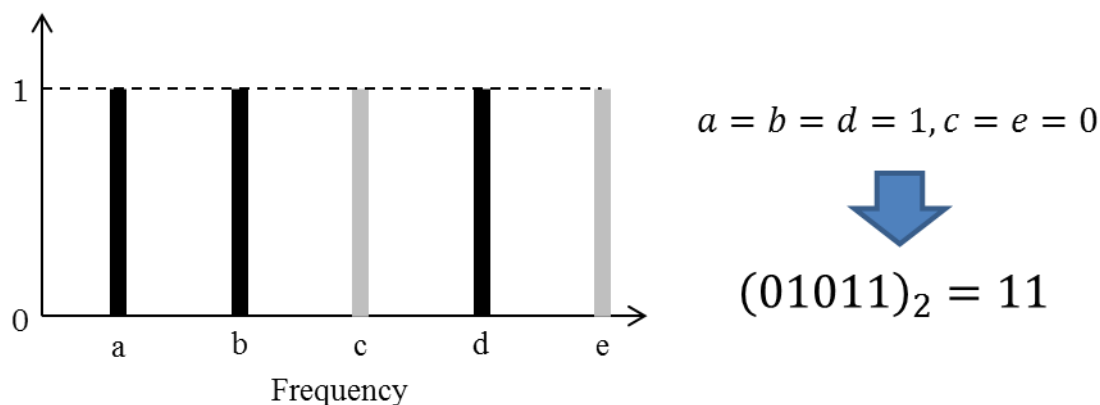


Figure 4-1. An example of the coding process for sorting information in THz spectrum.

The frequencies marked as “a” to “e” are considered as bits in the THz spectrum. A designed antenna array shall have the resonance (a singular area e. g. peaks in the spectrum) lies upon one or a few frequencies of those bits, while stays consecutively in other bits. For example, the deep black line in the spectrum of Figure 4-1 representing the location of resonance while the shallow gray lines indicate the opposite. By defining the value of frequency of bits as “1” when resonance appears or “0” when there is none, a binary information can be encoded from the spectrum of Figure 4-1 as $(01011)_2$,

which is 11. The more possible resonances an antenna array structure can have, the larger information can be sorted in it. Meanwhile, the Q values of those resonances are apparently becoming important given a challenge in designing the structures. A few researches in this direction to achieve high Q value deserve a mention [31-33] while other designs working in THz region such as split ring resonator (SRR) don't possess peaks of very high Q value yet [34].

A novel design of the planar metamaterial is presented in the later sections for exploring the identification application of it. Simulations and experimental results are compared and discussed.

4.2.2 Design and simulation results of “clock” shaped mode

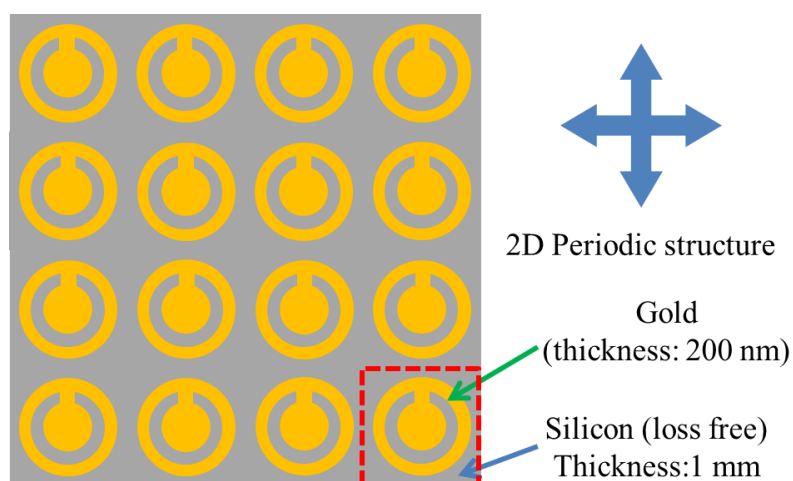


Figure 4-2. The basic model of “clock” shaped design

A “clock” shaped design was considered. The basic model of it is shown in Figure 4-2. The material for the patterns in yellow color is set as gold with the thickness of 200 nm. The substrate is made by 1-mm-thick silicon. It is a 2D periodic structure built and simulated by using CST Microwave Studio 2013 [35]. A ring with the outer radius of 40 μm and inner radius of 30 μm is beset a circle with radius of 20 μm , while there is a bar with 10- μm -width connecting them. It is a structure holding a similar appearance of a typical clock pointing at 0 or 12 am. The “clock” shaped pattern is repeating itself with a grid constant of 100 μm in both vertical and horizontal directions of the surface. A single cell of the design with spatial dimensions is presented in Figure 4-3.

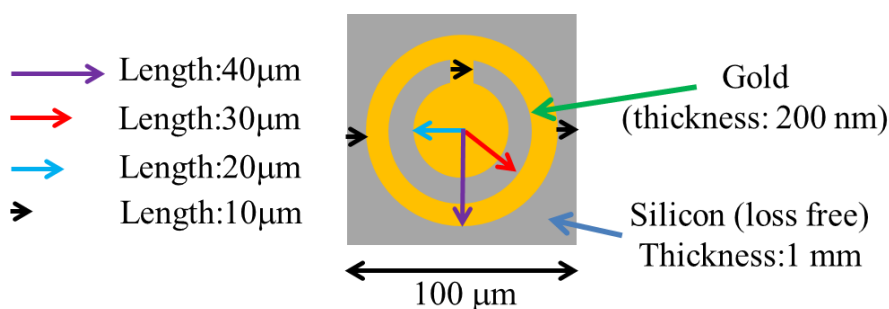


Figure 4-3. A single cell with spatial dimensions of the “clock” shaped model

Reflection spectra of such design and models introduced later in this section have been calculated. Although the research regarding metamaterials mostly concentrated on the study of transmission characteristic of the structure, reflection spectrum is more usable in the application of identification since the product encoded by any kind of terahertz tag/barcode may have a complex structure causing strong scattering of the transmitted beam or larger absorption simply lowering the signal-to-noise ratio, which in both ways inspection applying terahertz transmission spectrum is not practical. To calculate reflection spectrum, a linear polarized plane wave was excited and incident onto the surface of proposed model as shown in Figure 4-4.

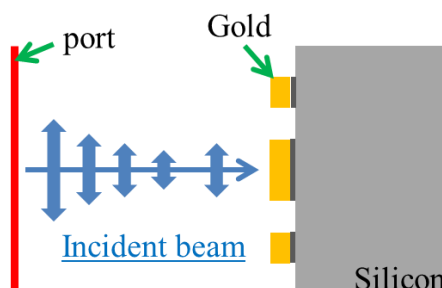


Figure 4-4. The diagram of simulation for reflection spectrum

In the simulation software, a time domain solver was applied to shorten the calculation time. THz signal was generated in time waveform and the simulator calculated the reflected signal in time domain as well. Fast Fourier Transformation (FFT) is required to achieve the information in its frequency spectrum, which is the same process as we conduct the measurements using THz-TDS mentioned in Chapter 2. With the finite thickness of the substrate, a second reflection pulse is expected to be observed in the calculation of time waveform. Figure 4-5 presents an example of the

calculated time signal with a time resolution of 15 fs.

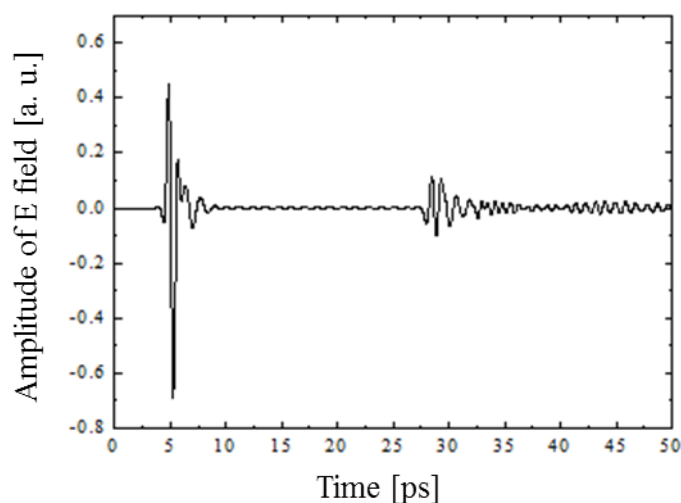


Figure 4-5. Calculated THz reflection signal in time waveform

Reflection of the opposite side of silicon substrate is clearly observed in calculation as we expected. Applying FFT on this signal would certainly bring the interference fringes into resulting spectrum, which can obstruct the study of the electromagnetic response of the patterns. Thus, we applied FFT onto the signal inside the time zone (0~26) ps by removal of all signal after 26 ps, achieving the frequency resolution around 30 GHz. The same treatment was also applied in the experimental results introduced in the following section 4.2.3. Next, some shaping of the basic model has been conducted to create the patterns as shown in the Figure 4-6.

Six transformed models based on the basic design are presented and named in the order of S1 to S6. For model S1, the metal bar was removed leaving outer ring disconnected with the inner circle; for model S3-6, another metal bar was added to connect the outer ring and inner circle and it rotate by the center of inner circle at an interval of 45° angle. Reflection spectra of model S1-6 have been calculated respectively and the reflectivity of each model was also acquired by dividing the reflection signal with a reference signal which was generated automatically by the software. Spectral results can be found in Figure 4-7.

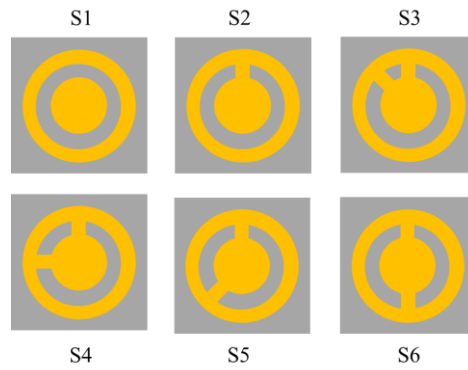


Figure 4-7. Several transformed models based on the basic design

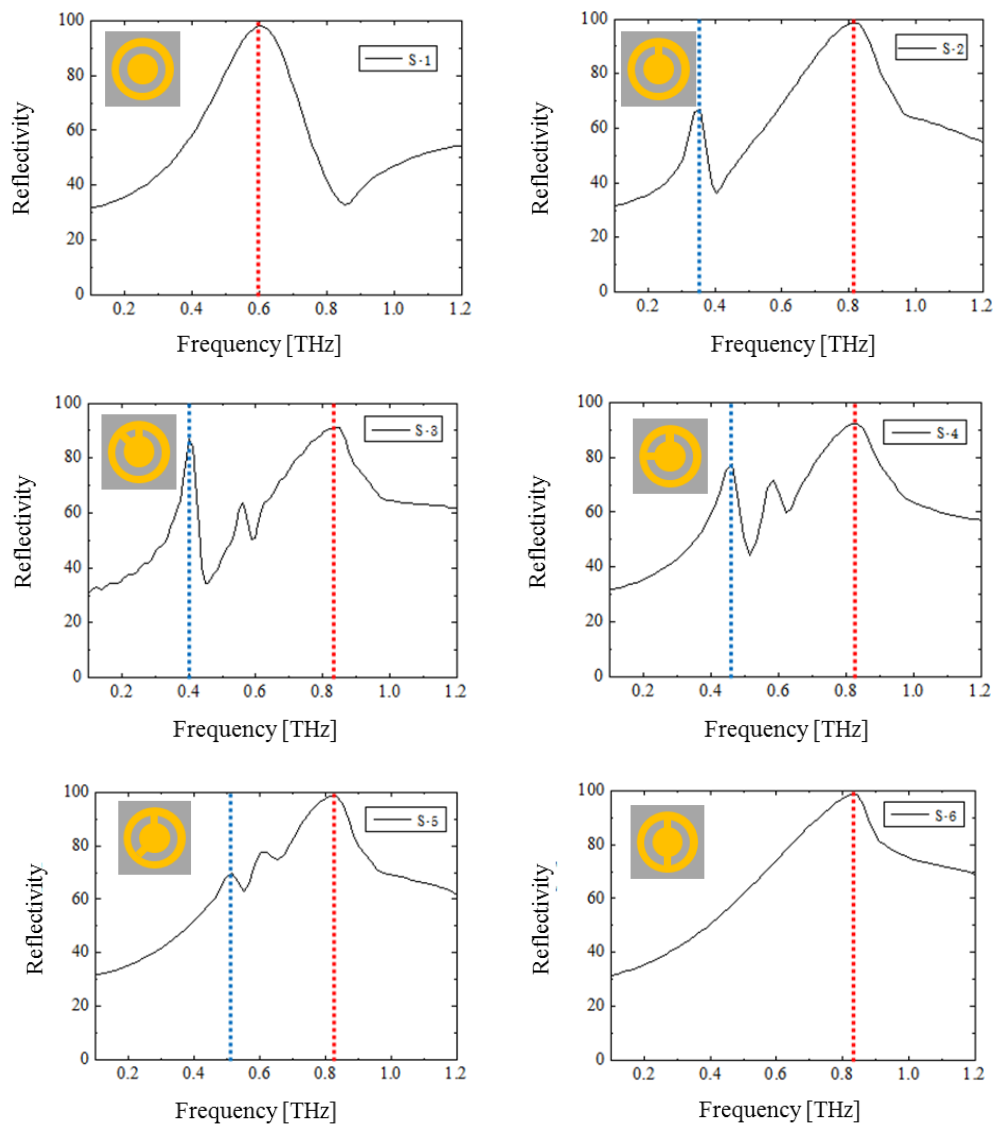


Figure 4-7. Calculated reflectivity of model S1-6

In the spectra of reflectivity, resonance peaks are marked in red line and blue line to distinguish from each other. We believe that these resonance peaks in different color

are caused by different mechanism while those in the same color share the origin of resonance. After conducting a rough summary of these results, some interesting conclusions can be made: the red peak occurred in higher frequency around 820 GHz stays the same in model S2-6 independent from the secondary bar added to the model; the blue peak actually shift towards higher frequency while the intersection angle between two metal bars getting bigger. A third peak between the red and blue peaks can be observed in the results of model S3-5, which is not to our interested as a reason will be given in the later section.

The positive correlation between the intersection angle of two metal bars and the frequency of blue peak is able to be used for coding the information in the following way: similar to that the different combination of bars in barcode system present different number, the frequency of the peak can present a certain number for the identification purpose controlled by the intersection angle. Next step is by how we can add new peaks in the spectrum for carrying more information. A solution to this question has been found.

We added another ring with bigger inner (50 μm) and outer radius (60 μm) to the structure as being shown in Figure 4-8. It is named as model S8 (another model was already named as model S7, which is not presented in this paper). With the bigger outer ring, the grid constant of such model is also enlarged by 40 μm keeping the distance between two closest cells as 20 μm .

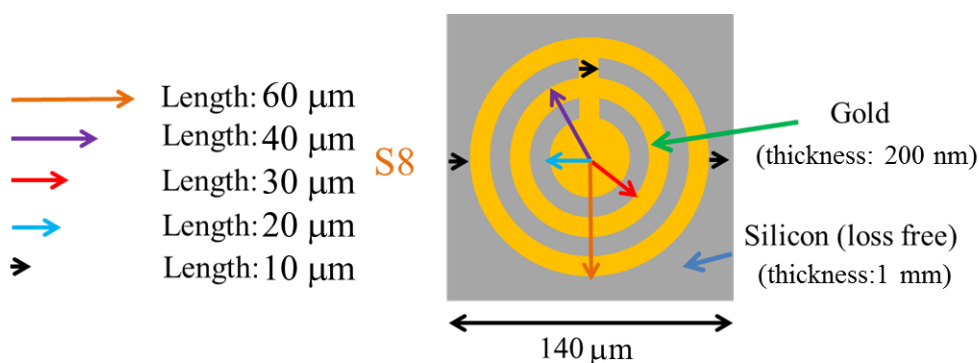


Figure 4-8. New design of model S8 adding a ring with bigger dimension.

Reflection spectrum of model S8 has been calculated and presented in Figure 4-9 (left side). Another model was also modified from model S4 and calculated. Its pattern and reflection spectrum are also shown in Figure 4-9 (right side)

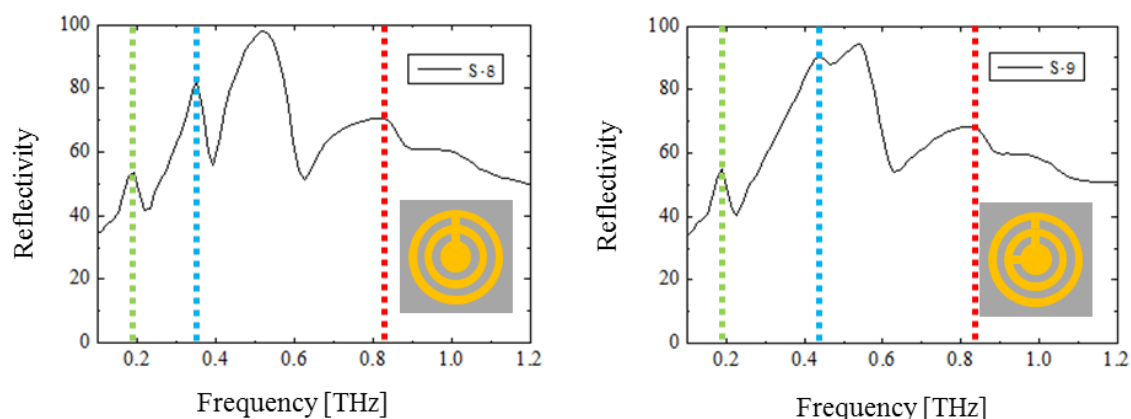


Figure 4-9. Calculated reflection spectra of model S8 and S9.

A new peak as marked in green line is occurred due to the secondary ring outside the original design. The frequency of red peak stays the same which is irrelevant to the existence of the secondary ring. Compared the spectrum of S8 and S2, we can observe that both the red and blue peaks stay the same frequencies, also being irrelevant to the existence of the secondary ring. These results suggest the possibility of controlling green and blue peaks independently. Thus the green peak can be considered as another channel to code information and in a way it solved the problem of carrying more information. More detailed discussion regarding to this aspect will be presented in section 4.2.4.

Next, we took a brief consideration of the electric field on the surface of metal at the resonance frequencies. Model S2 and S4 have been chosen for the comparison. The red peaks of both models are located at 816 GHz while the blue peak of S2 located at 356 GHz and that of S4 located at 443 GHz. Since the main concern of this study is the blue peak, electric field of blue peaks are presented in Figure 4-10 for S2 (left) and S4 (right) respectively. The color bars on the right side of figures indicate the amplitude of electric field from 0 (blue color) to its maximum (red color). From the results, we can conclude that the resonances of blue peaks mostly concentrate at the inner structures of the patterns between the ring and the circle. Attempt to find the correlation between the effective distance (distance between ring and circle in the direction of polarization) and frequency of the peak were conducted. However, it hasn't come to a conclusion, thus it isn't included in this paper.

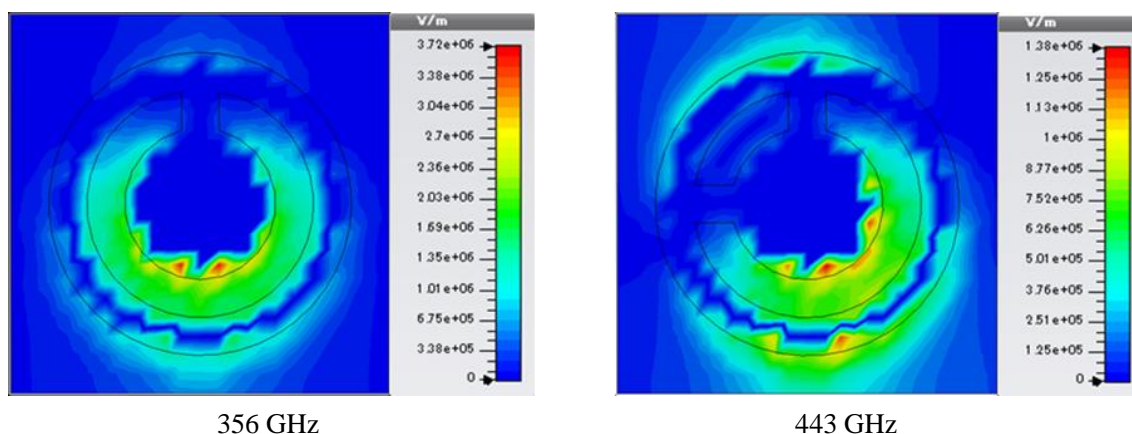


Figure 4-10. Electric field of blue peaks of model S2 (left) and S4 (right)

4.2.3 Experimental measurements of “clock” shaped mode

To verify the validity of our simulation results, samples share the same dimensions of pattern described in model S2, S4 and S9 have been fabricated and measured using THz-TDS with reflection geometry as shown in Figure 2-8 (b). A method called “lift-off process” [36] has been applied for manufacturing the samples. Figure 4-11 describe the procedure of it briefly.

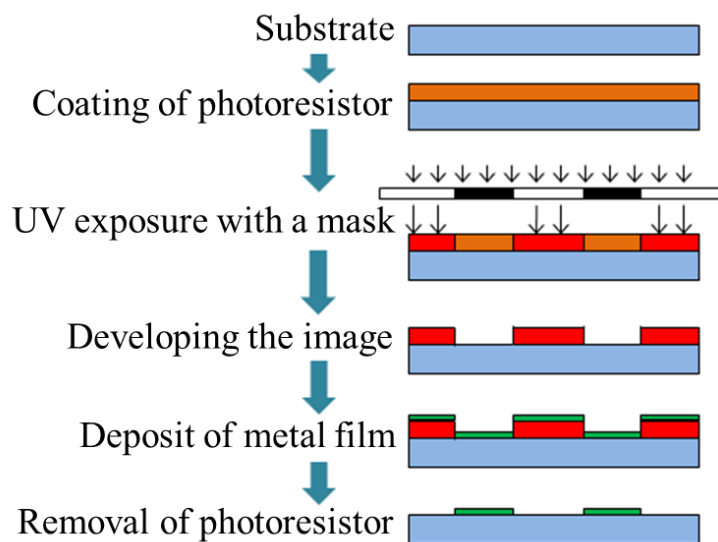


Figure 4-11. The procedure of “lift-off process” for sample manufacture

The patterns were coated onto a single silicon substrate with the thickness of 1 mm. 200-nm-thick Au film was applied for the patterns together with a 50-nm-thick Cr film for connecting Au and silicon substrate. Each model of gold pattern was placed in a $1 \times$

1- inch square area (25.4 mm × 25.4 mm). Figure 4-12 demonstrate the diagram of the samples.

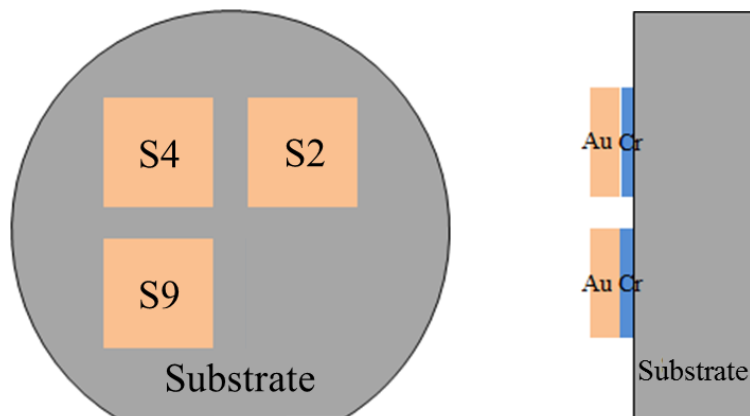


Figure 4-12. Image of patterns on silicon substrate (left: front view; right: side view)

Dimensions of each patterns don't repeat here, please refer to the figure 4-3 and 4-8. The fineness of fabricated samples was confirmed by using a microscope. Images of each pattern were recorded and presented in Figure 4-13.

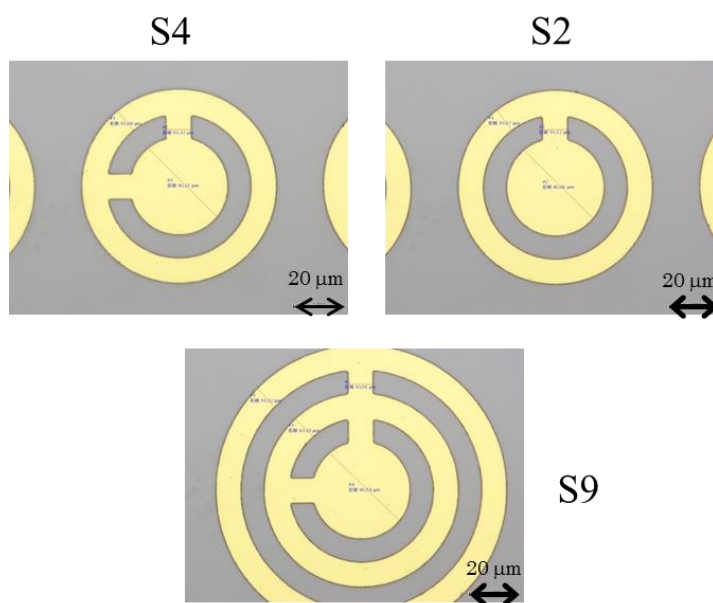


Figure 4-13. Images of patterns acquired by microscope

Time waveform of reflection signals of each pattern was acquired by THz-TDS and presented in Figure 4-14. A secondary reflected pulse of back-surface of silicon substrate can also be observed clearly. However, as we can observe that the pulse shapes

in real measurements are dissimilar to that of simulation. It is because we only calculated the reflection spectrum from 50 to 2000 GHz, while the available spectral range of our THz-TDS with reflection geometry is up to 3000 GHz. Additionally, the software we used generate the THz time signal based on the spectral range and intensity of radiation inside that range. Thus, simulation has a different reference signal compared to that of the real measurement. The important concern of this research is the reflectivity of the structures, which makes this difference of time signal irrelevant. By applying FFT on a selected time zone (a window of 26 ps width), reflectivity of three samples were achieved and presented in Figure 4-15 together with comparisons of simulation models respectively.

Good consistence between simulations and real measurements is achieved, proofing the validity of our model and calculation. The peak occurred between blue and red peaks in the simulation of model S4 didn't appear in the measurement in real field. A possible explanation of it could be that this resonance peak only occurs in simulation is aroused due to the idealization of simulation.

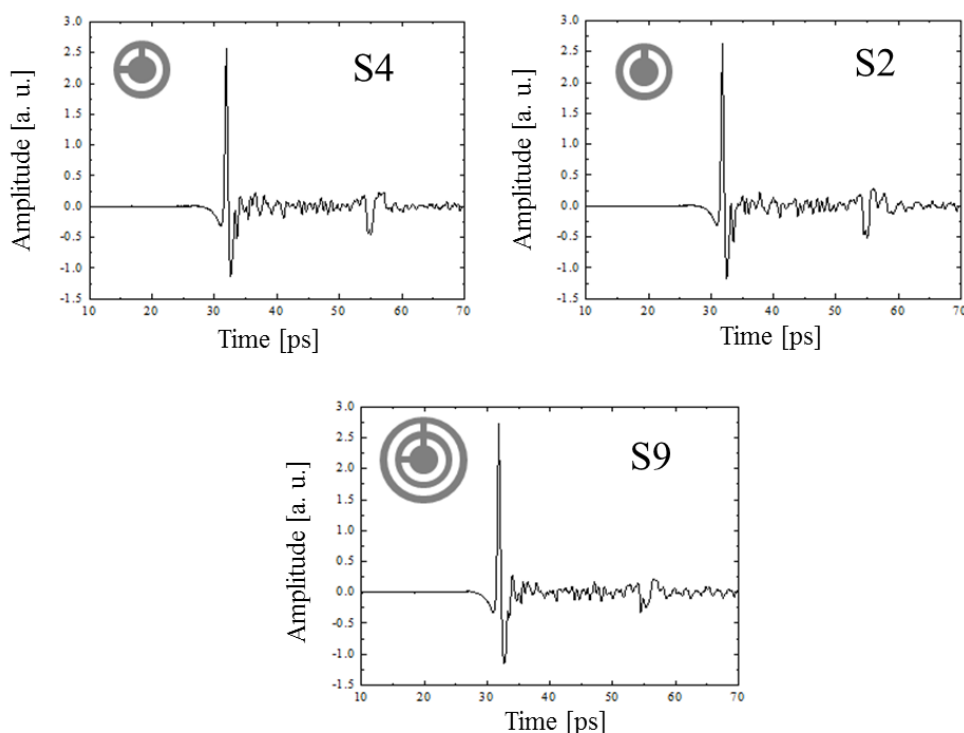


Figure 4-14. Time waveforms of samples acquired by THz-TDS with reflection geometry

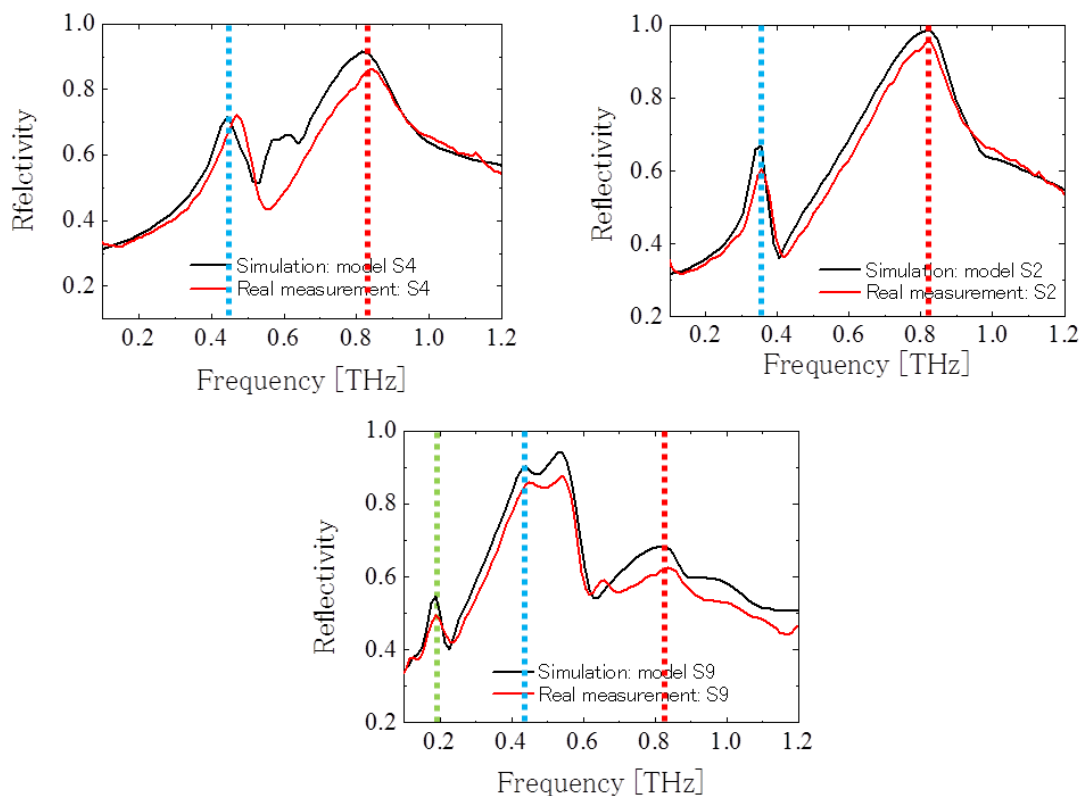


Figure 4-15. Comparison of simulation and real measurements for model S2, S4 and S9

We conducted an investigation of the polarization dependence of the blue and red peaks of fabricated samples. The direction of linear polarized THz radiation of THz-TDS setup can't be switch. Instead of that, we rotated the samples by angle of 45° each time in the order of 45° , 90° , 135° , 180° , 225° , 270° and 315° . A demonstration can be found in Figure 4-16.

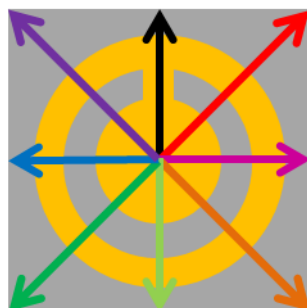


Figure 4-16. A demonstration of polarization measurements of model S2

The polarization direction of THz radiation started in horizontal direction which is

shown in the black arrow in figure. Then we rotated the sample clockwise around the center point of THz beam. That made the direction of linear polarized THz radiation turned counter-clockwise, thus the deep purple arrow represented the state of 45°, blue arrow represented the state of 90°, and so on. Measurements have been conducted for model S2 and S4, as shown in Figure 4-17 (a, b) respectively.

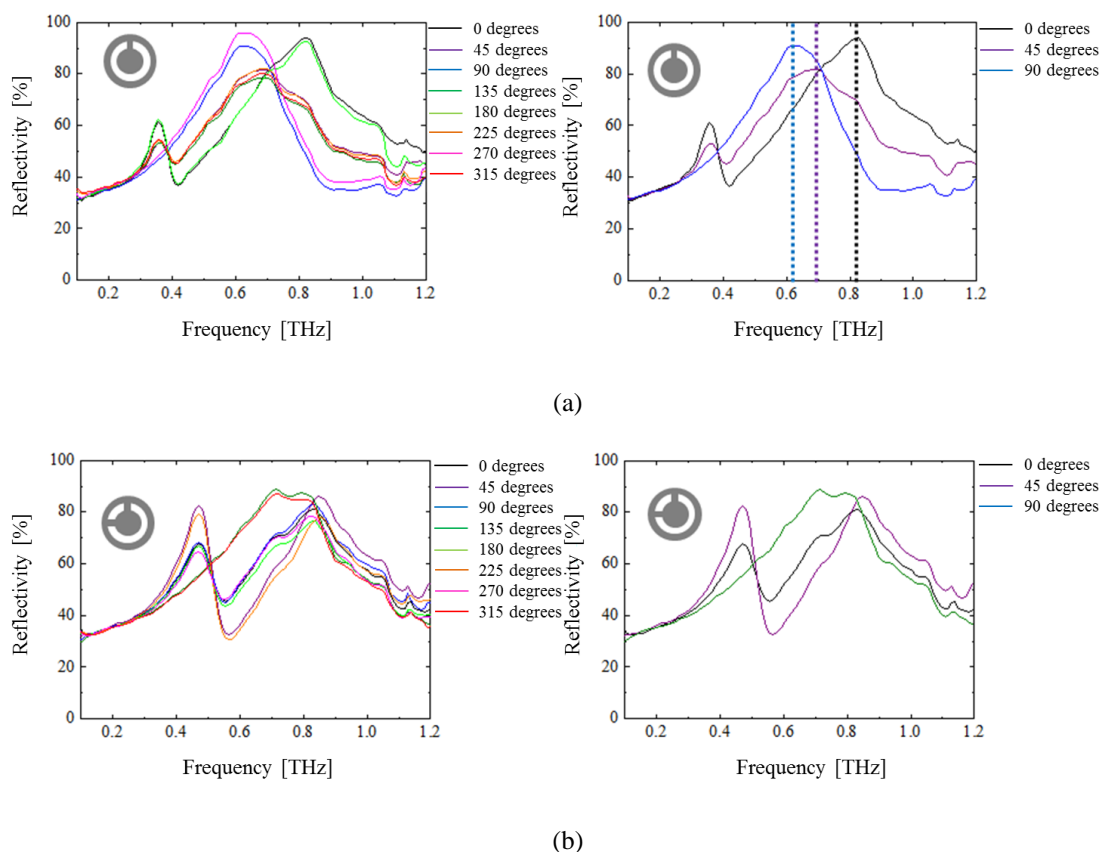


Figure 4-17. Polarization dependence of the resonance peaks for model S2 (a) and S4 (b)

As we can observed in Figure 4-17, polarization affect both blue and red peaks but in different ways. For easier analysis, three angles (0°, 45° and 90° for S2; 0°, 45° and 135° for S4) were chosen and presented for comparison as shown in the figures (right side) respectively. The amplitude of blue peak in lower frequencies gets smaller when the polarization deviated from the horizontal direction. However the frequency of blue peak didn't shift along with the rotation of polarization. On the other hand, the frequency of red peak shifts towards lower frequency along with the rotation of polarization, suggesting the origin of the resonances for blue and red peaks are different.

4.2.4 Discussion

In this section, a discussion will be presented for demonstrating the feasibility of applying “clock” shaped surface metal antenna for THz identification. Drawbacks will also be presented in the end of the discussion. Due to the disadvantages of this technique, we didn’t actually apply it for any identification measurements over obstacles.

Figure 4-18 shows the summarized results to demonstrate the shift of blue peaks in lower frequency region. This shift of frequency depending on the metal structure of the model could be applied for encoding the information, while the red peak in higher frequency region remains at almost the same frequency.

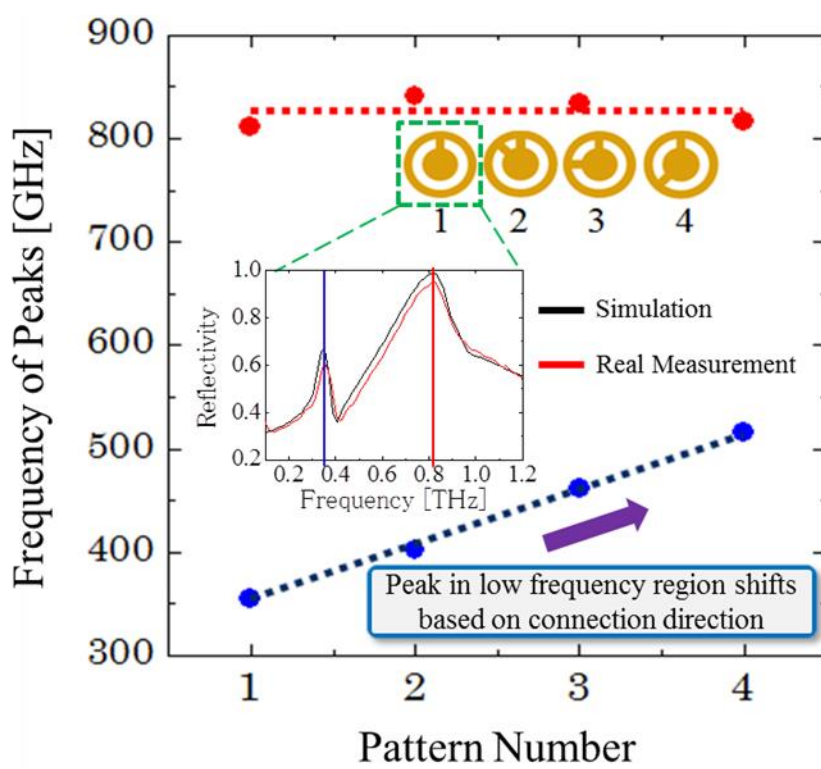


Figure 4-18. Locations of blue and red peaks in the reflection spectra of proposed models

The shift of frequency could be considered in proportion to the intersection angle between two metal bars connecting outer ring and inner circle of the “clock” shaped structure. This fact showed the simplification of our design for encoding the information. Next, Figure 4-19 demonstrated that our proposed model can independently control the peak frequencies of blue and green peak by adding a secondary ring into the structure.

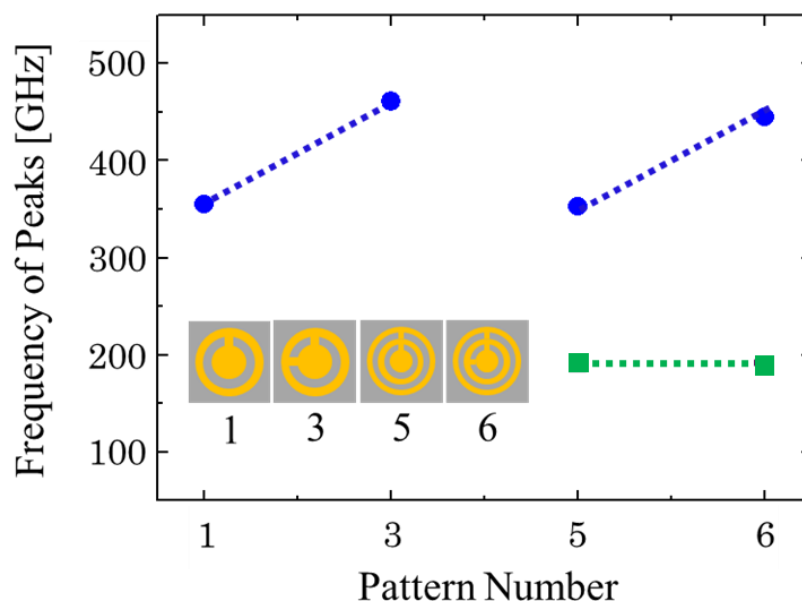


Figure 4-19. Shift of the blue peak in reflection spectra of model for increasing the

Although we have demonstrated the validity of applying our proposed metafilm to application of THz identification, the drawbacks of the technique such as being list here were still inevitable: the material for fabricating metal patterns need to have very good conductivity (e. g. gold, copper); the dimensions of pattern were subwavelength order, and the width of metal structure is only 10 μm . Several optimizations of the features of proposed design have been conducted (results aren't shown in this paper) but failed to achieve high Q value of the peak; the structure fabricated by lift-off process having the features in the order of tens of micrometers is very costly (one pieces of our silicon substrate which has three patterns being coating cost over 400,000 yen). The cost performance of it is very low at the moment, considering the bits of information it may hold. Thus, we have changed our view for achieving THz identification over obstacles in another way, which will be demonstrated in details in later section.

4.3 Concealed THz barcode identification system using THz-TDS

The existing barcode system has many good qualities such as printability, low cost,

and especially many related well-operating techniques to read its image in a noisy environment due to the long history since it firstly stroke the market. Before this study, there has been no report regarding direct measurement of the barcode images over obstacles by using the ability of THz wave.

Here, we describe a new type of barcode that operates at THz frequencies. The system can be considered a hybrid of a conventional barcode and RFID, and it meets the requirements of a low-cost system for industrial identification of concealed tags. Rather than designing antennas to serve as a chipless tag, we use a printed barcode system that is concealed behind the packaging and use ink that is highly reflective at THz wavelengths. In implementing such a concept, the following should be considered. The spatial resolution for imaging depends on the spot size of the imaging beam and this, in turn, depends on the wavelength, which is on the order of millimeters at the lower end of the THz frequency range. The features on barcodes and QR codes have sub-millimeter dimensions; however, it is not practical to achieve such small features using a THz system using diffraction-limited optics because of the requirement for a lens with a very large numerical aperture, which is challenging at THz frequencies. Furthermore, the higher end of the THz high-frequency range is characterized by greater absorption from common packaging materials, which makes the reflected signal weak, thereby degrading the signal-to-noise ratio.

We use a printable barcode design with a dielectric coating layer on the back-side to construct an etalon cavity, which should operate behind a layer of packaging. Instead of making effort to get rid of the attenuation and obstructive multiple reflections caused by the presence of obstacle, we exploit it and try to utilize it to our advantage. This allows us to read the image of a barcode even when the dimensions of the low-frequency beam are larger than the width of the bar. Because this type of barcode works with a printable coating layer, we refer to it as a double-side printed barcode. We describe the results of imaging experiments, together with a comparison of a single-side printed barcode without covering and our double-side printed barcode. In our experiments, a thick express mail service (EMS) envelope was used as an obstacle. All experiments were performed using THz time-domain spectroscopy (THz-TDS) under conditions that approximate what can be expected in the field; thus, the imaging beam was soft focused, and a dry nitrogen environment was not used.

4.3.1 Sample preparation

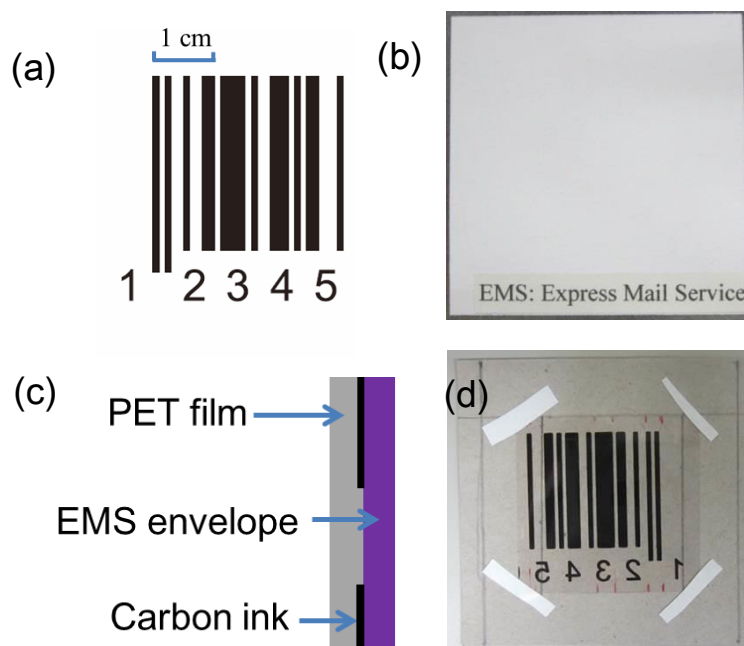


Figure 4-20. (a) The geometry of the 1D barcode, (b) the EMS envelope, (c) the structure of the barcode sample and envelope, and (d) a photograph of the reverse side of the barcode and envelope.

We carried out spectral-imaging measurements using a one-dimensional (1D) barcode with and without the EMS envelope. The envelopes were made of water-resistant, durable paper, which is commonly used and provided by the post office, and samples were cut into 7×7 -cm pieces. The thickness of the envelope was approximately $330 \mu\text{m}$, as measured using a micrometer. A $50\text{-}\mu\text{m}$ -thick polyethylene terephthalate (PET) film was used as a substrate to have barcode patterns being printed on. Many kinds of metal (e. g., aluminum, copper) have high reflectivity in THz region. They could have been considered good candidates as the ink for barcode except for their high cost in manufacture. In this paper, a conductive carbon ink was used to print the $8\text{-}\mu\text{m}$ -thick barcode patterns onto the PET film because of the high reflectivity at THz frequencies. This conductive carbon ink is inexpensive; it is commonly used to form membranes for flexible electronic circuits and has surface resistivity of $10 \Omega/\text{cm}^2$ at $14\text{-}\mu\text{m}$ -thick. Figure 4-20 (a) shows the form of the barcode pattern, and Figure 4-20 (b) shows an image of the envelope. The minimum width of the barcode feature is 1mm . In the experiments, the barcode samples were attached to the back of the envelope with the inked surface in

contact with the paper, as shown schematically in Figure 4-20 (c). Figure 4-20 (d) shows an image of the PET film imprinted with the barcode and attached to the envelope. All the barcode samples were manufactured and provided by Dai Nippon Printing Co., Ltd., Japan.

4.3.2 Experimental setups and conditions

We used a THz-TDS system with reflection geometry. The samples were examined at a 20° angle of incidence using a THz beam soft focused using a parabolic mirror with an effective focal length of 4 inches. The size of the beam at the focal point, and therefore the spatial resolution of the THz-TDS system, depends on the frequency. This frequency dependence of beam dimension at focal point has been inspected by the knife-edge measurement. The full-width at half-maximum (FWHM) of THz wave calculated from the results along with the exponential fitting are presented in Figure 4-21 (a). It suggests that the FWHM of beam is around 3.3 mm at 0.41 THz and 1.5 mm at 0.99 THz, which is larger than the minimum width of the barcode feature. Commercially available photoconductive antennae were used as the emitter and detector. Because a dry nitrogen environment was not used, the effects of water vapor absorption were present in the spectra. Figure 4-21 (b) shows the THz time-domain waveform and Figure 4-21 (c) shows the corresponding spectrum for transmission through air with no sample as a reference. The frequency resolution of our measurements was approximately 12 GHz. Absorption lines due to water vapor can clearly be seen, which is consistent with previous reports [37]. The reflectivity of the conductive carbon ink is shown in Figure 4-21 (d). The conductive carbon ink was highly reflective at frequencies in the range 0.2–2.2 THz. Reflectivity of 50- μm -thick PET film as substrate is also presented in Figure 4-21 (d). The interference of it can be observed clearly.

Some of the reflections from the carbon ink appeared to show a reflection coefficient larger than 1, which is attributed to the stability of the system, particularly to variations in the amount of water vapor. Consequently, to acquire sufficient contrast in our imaging experiments, all results were scaled so that the maximum reflectivity was 1. Figure 4-21 (e) shows an overview of the reflection geometry. Samples were scanned at 1D with a step size of 200 μm . We acquired a complete time waveform at each step to investigate spectral information.

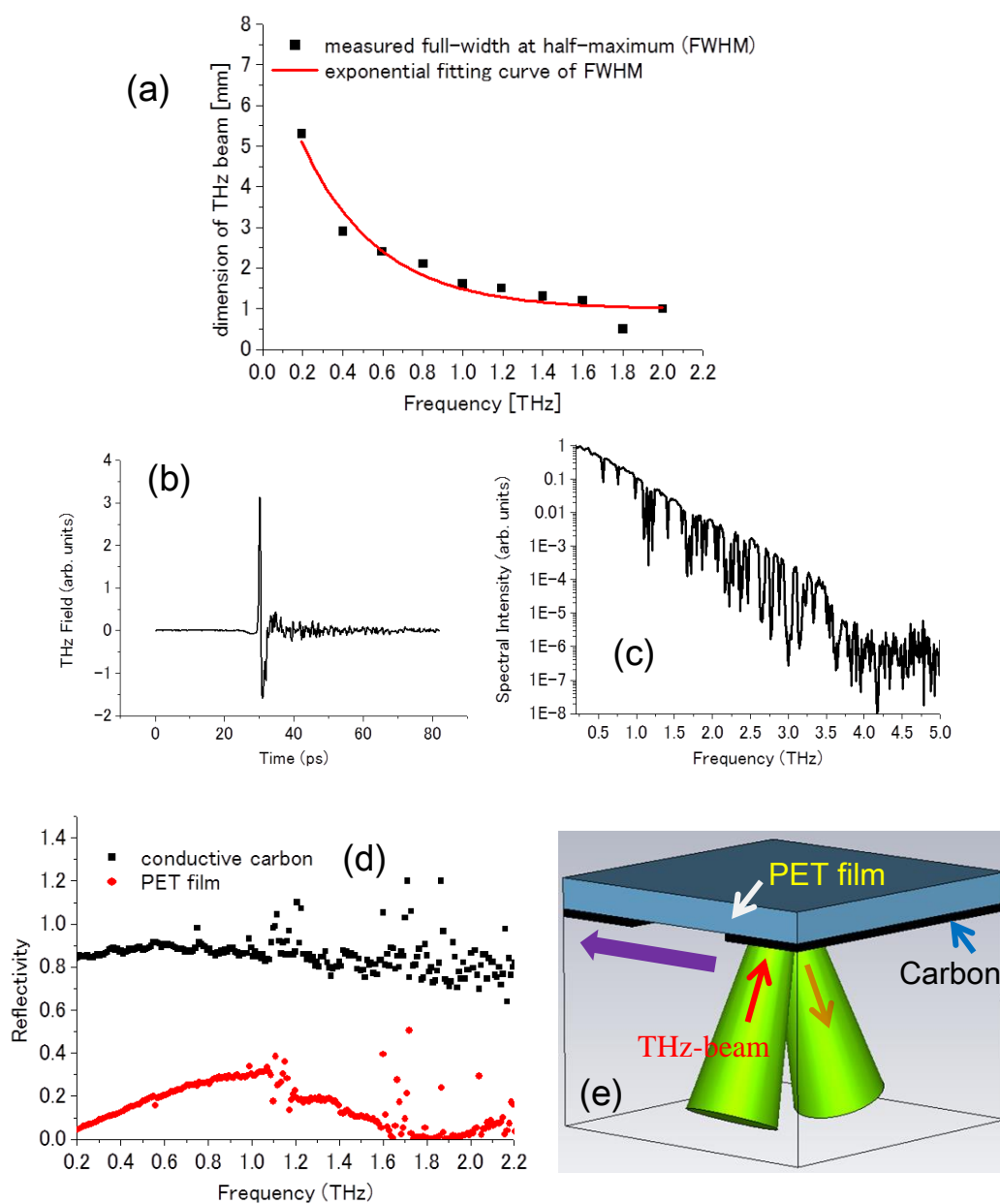


Figure 4-21. (a) The FWHM of THz beam at focal point acquired by knife-edge measurement . (b) THz time-domain waveform. (c) The corresponding frequency spectrum. (d) The reflectivity of conductive carbon (~0.85) and the 50- μm -thick PET film. (e) A schematic diagram shows the incident and reflected signals. The THz beam was focused and the angle of incidence was 20° . The purple arrow indicates the scanning direction.

4.3.3 Measurements of single-side printed barcodes

First, a barcode sample, shown in Figure 4-20 (a), was measured without the EMS

envelope to check the system performance and effectiveness of the carbon ink. The dimensions of the sample are shown in Figure 4-22, together with a pseudocolor plot showing the reflectance spectra scanned along the length of the barcode. The relatively large beam diameter at low frequencies led to poor resolution below 1 THz. However, at higher frequencies, the barcode was clearly resolved. The features at 1.2 THz and 1.7 THz correspond to absorption lines from water vapor.

Next, this sample was measured through the EMS envelope with results being presented in Figure 4-23 (a). A barcode pattern with a single 1-mm-wide bar printed on the PET film was fabricated. The reflection was measured behind the EMS envelope, as shown in Figure 4-23 (b). The interference fringes will be discussed in more detail later. Because the attenuation coefficient of the paper increased with frequency [38, 39], the location of carbon bar could not be determined at frequencies around 2 THz. Additionally, the blurred image at low frequencies does not clearly reveal the dimensions of the bars.

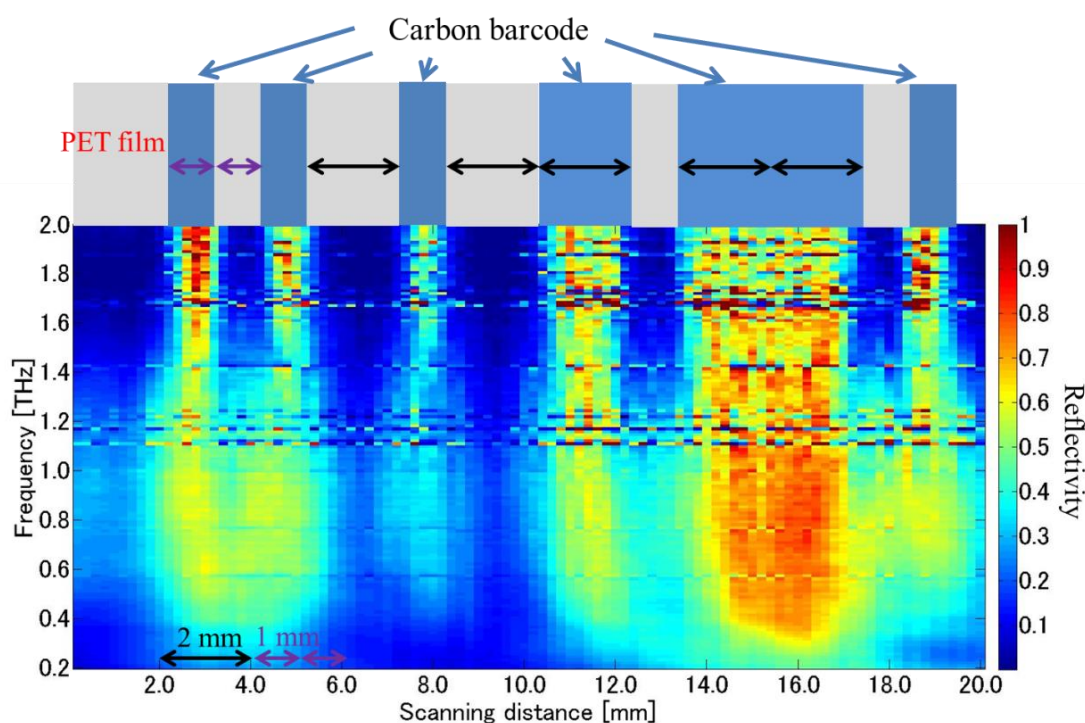


Figure 4-22. Reflection spectra for the barcode (with no EMS envelope) along the length of the barcode.

The features of the 1D barcode can be clearly resolved at frequencies around 2 THz.

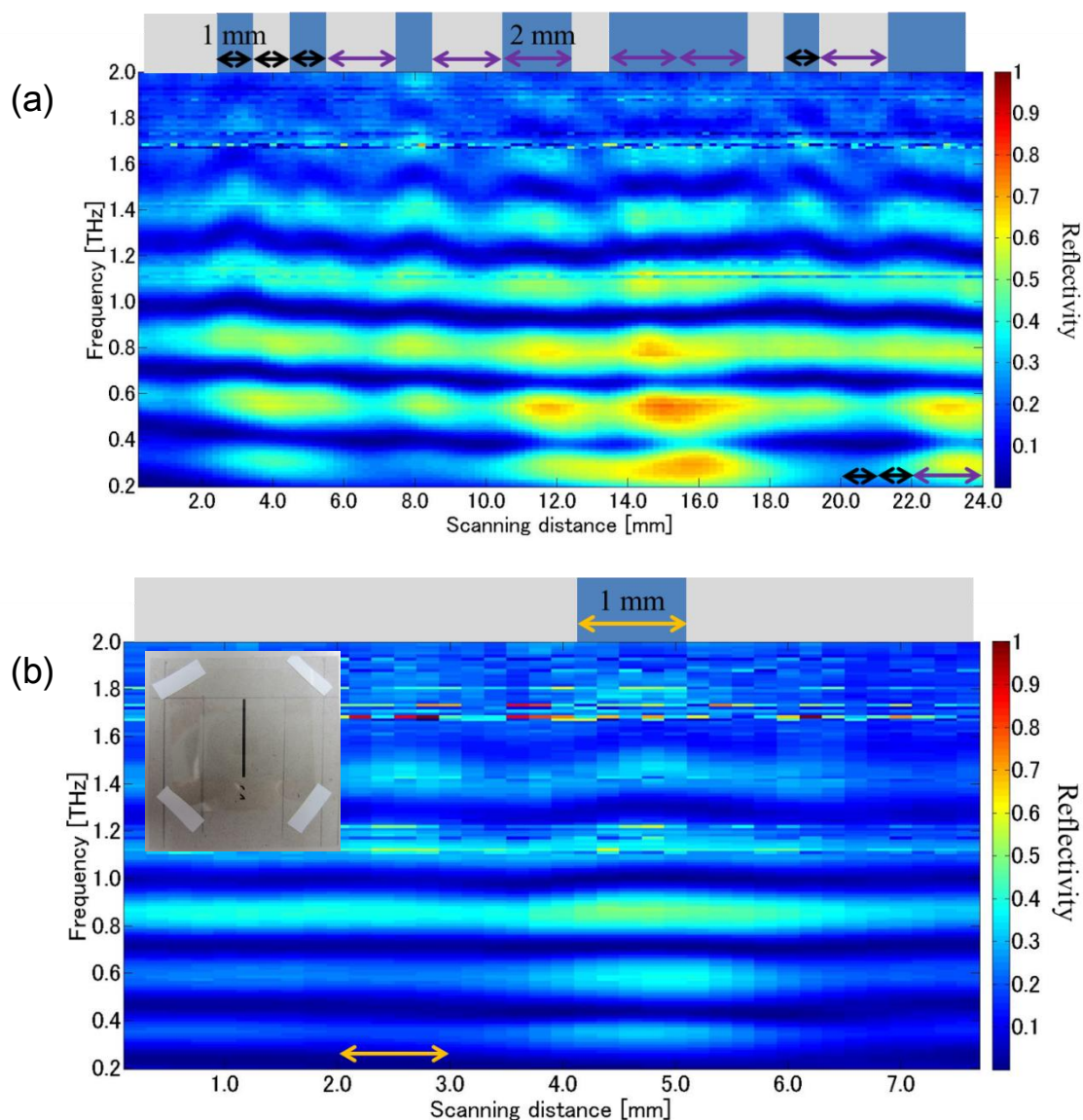


Figure 4-23. (a) Reflection spectra of the barcode behind the EMS envelope (b) Reflection spectra scanned across the single-bar behind the EMS envelope. The inset shows an image of the sample behind the envelope. The bar was 1 mm wide.

4.3.4 Measurements of double-side printed barcodes

The structure of the double-side printed barcode is shown schematically in Figure 4-24, together with a diagram showing the incident and reflected THz beams. Compared with the single-side printed barcode measurements described in the previous subsection, we added a highly reflective coating layer on the back side of the PET substrate to create

an etalon cavity. An aluminum plate mirror was applied as the coating layer firstly to testify the effectiveness of the proposed setup. Measurements of the structure behind the EMS envelope with single- and double-bar samples were carried out, and the results are shown in Figure 4-25 (a) and 4-25 (b), respectively. In the frequency region lower than 1 THz, the bars can be observed with much better definition than with the simple barcode sample, and the shape of each bar is clearly defined. The barcode shown in Fig. 4-20 (a) was also applied for the measurements, as shown in Fig. 4-26 (a). The features can be resolved in the resulting spectra.

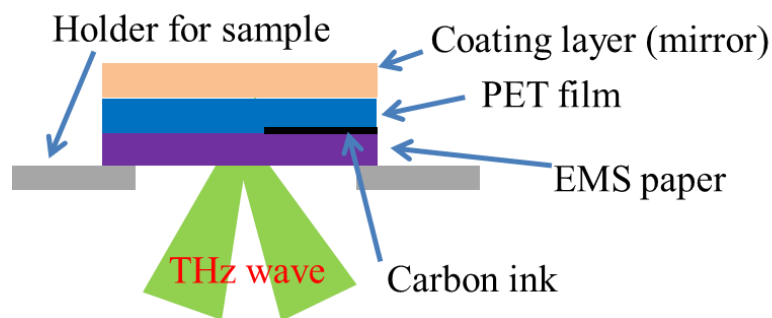
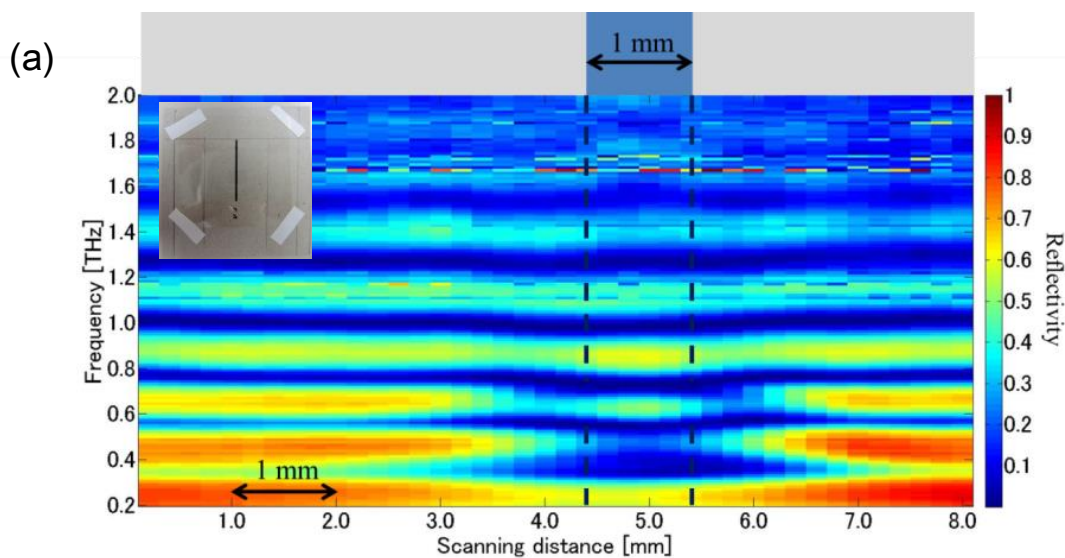


Figure 4-24. Setup for double-side printed/back-coated barcode: coating layer on the back side of PET film with high reflectivity has been added to create an etalon cavity; firstly, an aluminum mirror was applied as a coating layer to achieve high reflection; next, sample with carbon ink being back-printed as the coating layer was measured to demonstrate the validity of double-side printed setup.



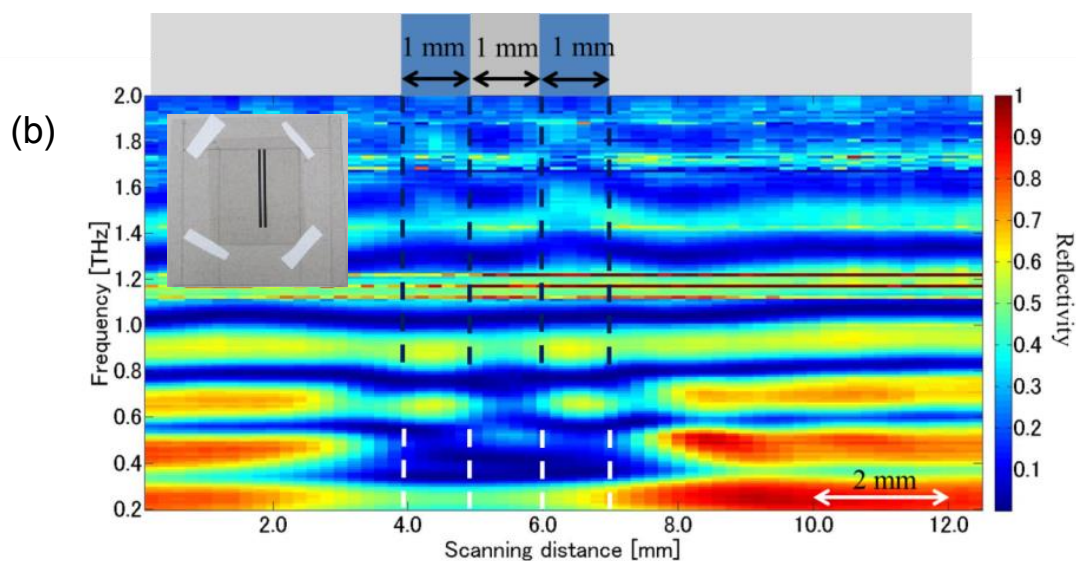
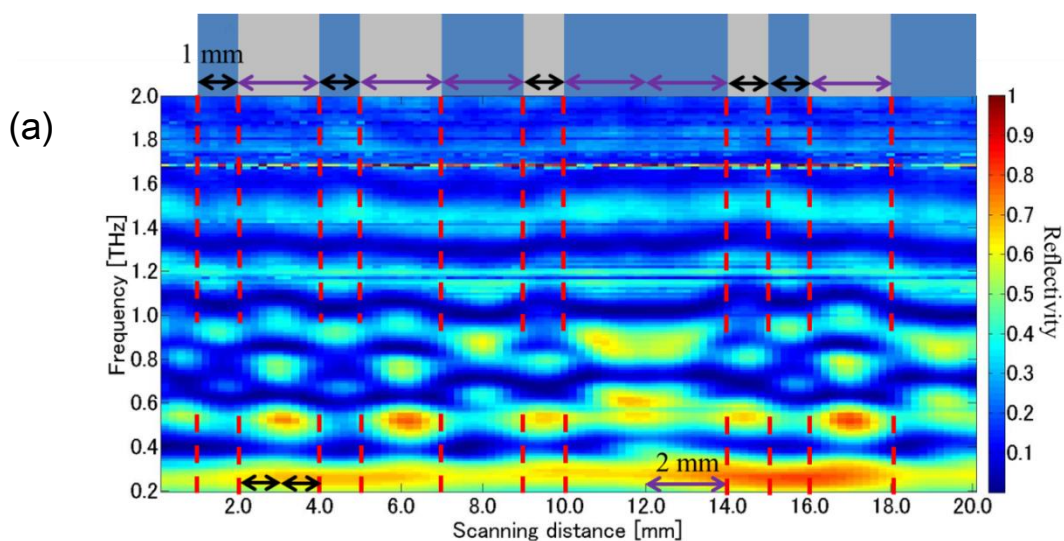


Figure 4-25. Spectral imaging of samples behind the EMS envelope achieved by applying the back-coated setup; An aluminum mirror was applied as the coating layer: (a) Spectral imaging of a single-bar sample. (b) Spectral imaging of double-bar sample.

Next, a sample with double-side printed by carbon ink was fabricated and measured behind EMS envelope. On one side, it has the same barcode features as described in Fig. 4-20 (a); on the other side, it was fully covered by an 8- μm -thick layer of carbon ink. Reflection spectra of it are presented in Fig. 4-26 (b). These results show that our double-side printed barcode system provides favorable performance compared with the simple barcode system described in section 4.3.3.



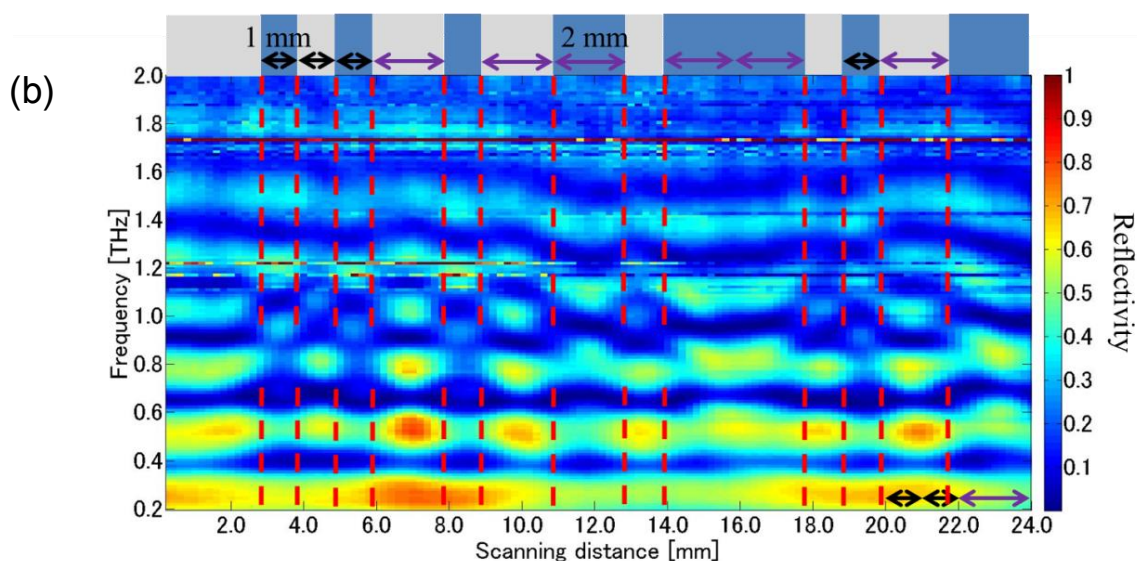


Figure 4-26. (a) Reflection spectra of the back-coated setup barcode behind the EMS envelope; aluminum mirror was applied as coating layer. (b) Reflection spectra of the double-side printed setup barcode behind the EMS envelope; an 8- μm -thick layer of carbon ink was printed on top of substrate.

Furthermore, normalization of the reflectivity at 900 GHz has been carried out for the spectrum of the carbon ink double-side printed barcode setup, as shown in Fig. 4-27 (a): a threshold of ‘0.38’ has been chosen for the calculation; value of any step with the reflectivity below the threshold was set to 0; value was unified to 1 when reflectivity exceeded the threshold. Given the fact that scanning step of sample was 0.2 mm, we considered that a good consistency was acquired. On the other hand, the normalization results of the single-side printed barcode was conducted and presented in Figure 4-27 (b) for comparison. The reflection spectra of Figure 4-23 (a) was applied for the calculation. For acquiring strongest reflection intensity, 864GHz has been chosen for the calculation. According to the knife-edge measurement as shown in Figure 4-21 (a), the differences of beam size at 864 GHz (1.69 mm) and 900 GHz (1.62 mm) are small. Thus, we can be considered that the normalizations are conducted under same condition.

Several thresholds have been chosen from 0.33 to 0.43 trying to resolve the features of barcode by the spectrum of single-side printed barcode. When the threshold set to 0.33, the normalized result shown in black line of Figure 4-27 (b) definitely get too big to fit the real feature of the barcode. This means the threshold of 0.33 is too low in this case. After increasing it little by little, normalized results become sharper and

slowly approach to the real feature. However, when the threshold set to 0.43, result in green line suggest that it is too high as the features become too separated from the real sample. These results proof that by using normalization, the double-side printed barcode can be resolved with much better accuracy than the simple-side printed barcode.

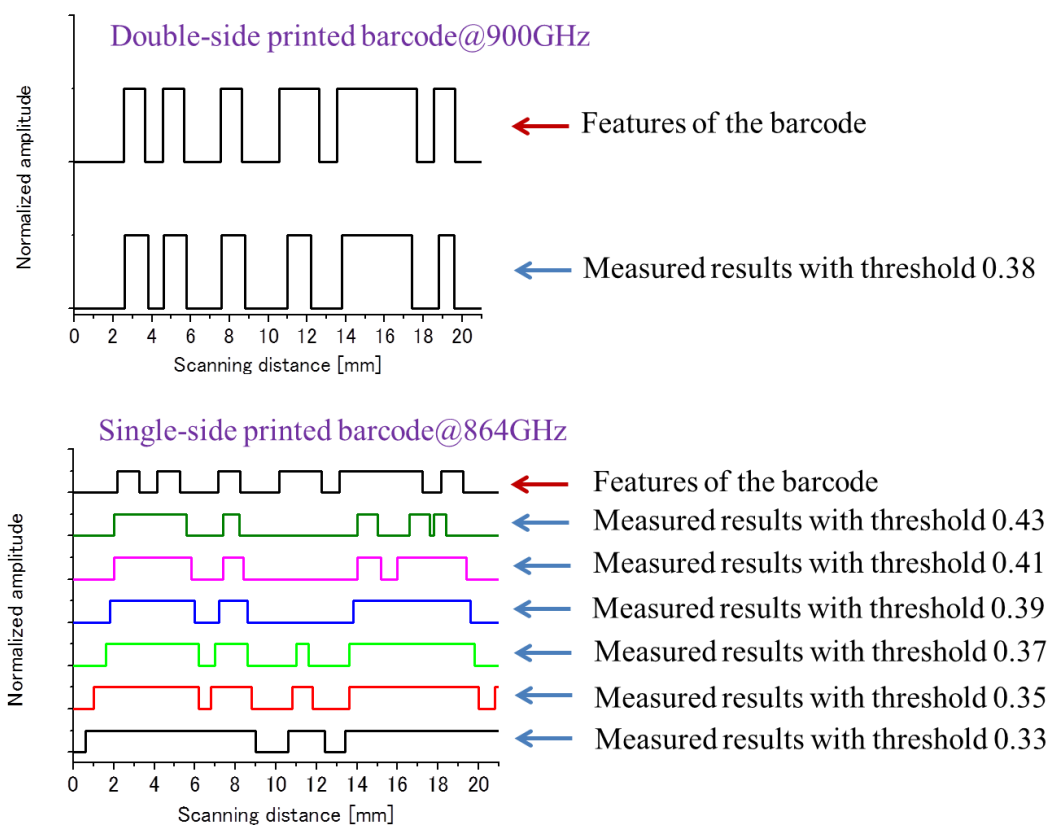


Figure 4-27. (a) Normalization of the spectrum of Figure 4-26 (b) at 900 GHz; a threshold of ‘0.38’ has been chosen for the calculation; (b) Normalization of the spectrum of Figure 4-23 (a) at 864 GHz; several thresholds have been chosen for the calculation.

4.3.5 Theoretic analysis of double-side printed barcode system

An explanation of the principle of the double-side printed barcode is presented in this section. For simplification, back-side coating layer of an aluminum mirror is considered. Reflection spectra of the EMS envelope and the PET film attached to the EMS envelope were acquired using THz-TDS. Both spectra exhibited interference patterns due to multiple reflections from the planar dielectric layers, as shown in Figure 4-28. The interference patterns indicate that there was no strong reflection due to the boundary between the PET and the EMS envelope, which indicates that the refractive

indices of the two materials were similar [38–41]. Therefore, in the simulations, we considered a homogeneous dielectric with a constant refractive index and a constant absorption coefficient to describe the PET and EMS envelope layers. Accordingly, we simplified the multi-layer structure, as shown in Figure 4-29 (a).

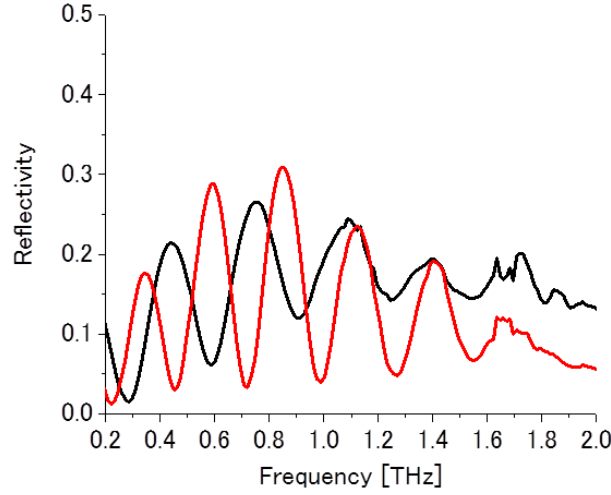


Figure 4-28. Reflection measurements of the EMS envelope (black line) and PET film firmly attached to the EMS envelope (red line) without a mirror. Etalon interference fringes can be seen in both spectra. Because of the attenuation of paper, which depends on frequency, the interference fringes disappeared at high frequencies.

Two cases were considered, i.e., either the THz radiation is not incident on the barcode and penetrates fully through the 380- μm -thick dielectric layer to be reflected by mirror, or the THz beam penetrates the 330- μm -thick dielectric corresponding to the EMS envelope and is reflected from carbon ink layer. Figure 4-29 (b) shows the geometry of the multiple reflections considered in the model. The reflected electric field can be calculated using the following equations [42]:

$$E_1 = r_1 \cdot e^{i\pi} \cdot E_0 \quad (4-1)$$

$$E_2 = t_1 \cdot t_1' \cdot r_2' \cdot e^{i(\delta+\pi)} \cdot a \cdot E_0 \quad (4-2)$$

$$E_3 = t_1 t_1' r_1' (r_2')^2 e^{2i(\delta+\pi)} E_0 = E_2 \cdot (a^2 r_1' r_2' e^{i(\delta+\pi)}) \quad (4-3)$$

•
•
•

$$E_m = t_1 t_1' r_2' (r_1' r_2')^{m-2} e^{i(m-1)(\delta+\pi)} a^{m-1} E_0 \quad (4-4)$$

$$E_r = E_1 + E_2 + E_3 + \dots + E_m + \dots = \sum E_m \quad (4-5)$$

Where $\delta = 4n\pi d \cos \theta \cdot \lambda^{-1}$ describes the phase change due to the optical path difference of reflections from the upper and lower surfaces, n is the refractive index of the medium, d is the thickness, θ is the angle of refraction at the air–dielectric interface, and λ is the wavelength. An additional phase shift of π must be considered for each reflection from a more optically dense medium, in this case, the air–dielectric and dielectric–mirror interfaces. The terms t_1 and t_1' are the transmission coefficients of the air–dielectric interface, r_1 and r_1' are the reflection coefficients. The terms t_2, t_2', r_2 and r_2' describe the transmission and reflection coefficients for the dielectric–mirror interface. The Stokes relations result in the following relations for the for air–dielectric interface:

$$t_1 \cdot t_1' = T_1 \quad (4-6)$$

$$r_1^2 = r_1'^2 = R_1 \quad (4-7)$$

where T_1 is the transmission, and R_1 is the reflection.

The dielectric–mirror interface has no transmission, and the reflectivity of the THz beam at this interface can be expressed as follows:

$$R = \frac{I_r}{I_0} = \frac{E_r \cdot E_r^*}{E_0^2} \quad (4-8)$$

This model can replicate the interference patterns of the two cases described in Figure 4-29 (a), as shown in Figure 4-30 (a) and 4-30 (b).

Here, we consider that the THz beam is reflected partly from the carbon ink and partly from the mirror. We analytical calculated a region with half of the area covered by the carbon ink using Matlab software. This geometry was also fabricated and measured for comparison with the simulations. We assumed that the THz beam had a Gaussian profile, so the intensity distribution is given by

$$I_{THz}(x, y) = I_0 \exp\left(-\frac{l^2(x, y)}{2\sigma^2}\right) \quad (4-9)$$

where

$$l^2(x, y) = x^2 + y^2 \quad (4-10)$$

(x, y) are the coordinates of a $100 \times 100\text{-}\mu\text{m}$ square beam area (i.e., the cell used in the calculation), l is the distance from the center of beam, and σ determines the beam distribution in the direction transverse to propagation. The intensity at $l = \sigma$ is given by

$$I_{THz}(l = \sigma) = \frac{I_0}{\sqrt{e}} \quad (4-11)$$

The full-width at half-maximum (FWHM) was approximately 2.35σ . The beam distribution depended on frequency was calculated from the measured FWHM of THz-TDS as mentioned in Figure 4-21 (a), so $\sigma = 2.15$ mm at 0.2 THz and varied linearly to 0.43 mm at 2 THz. The beam area for calculation was set as 4σ at each frequency; thus, $-2\sigma \leq x \leq 2\sigma$ and $-2\sigma \leq y \leq 2\sigma$.

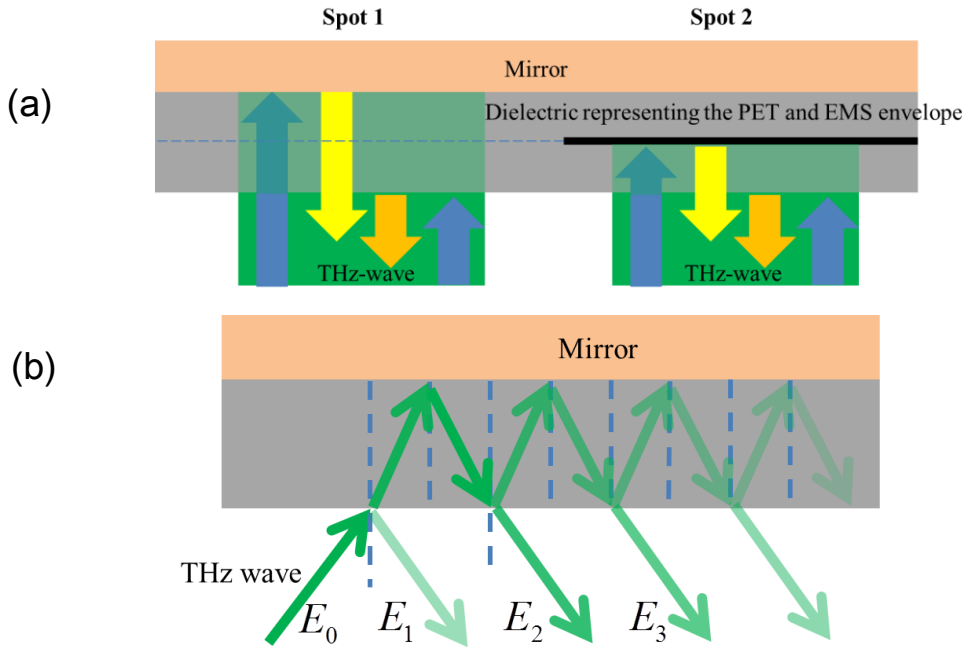


Figure 4-29. (a) The simplified structure used in the simulations, with a homogenous dielectric with the refractive index of PET. The blue dashed line shows the internal boundary between the PET film and the envelope; and the thick black line shows the carbon ink. The blue arrows represent the incident THz radiation; the yellow arrows represent the reflections. (b) Schematic diagram showing multiple reflections

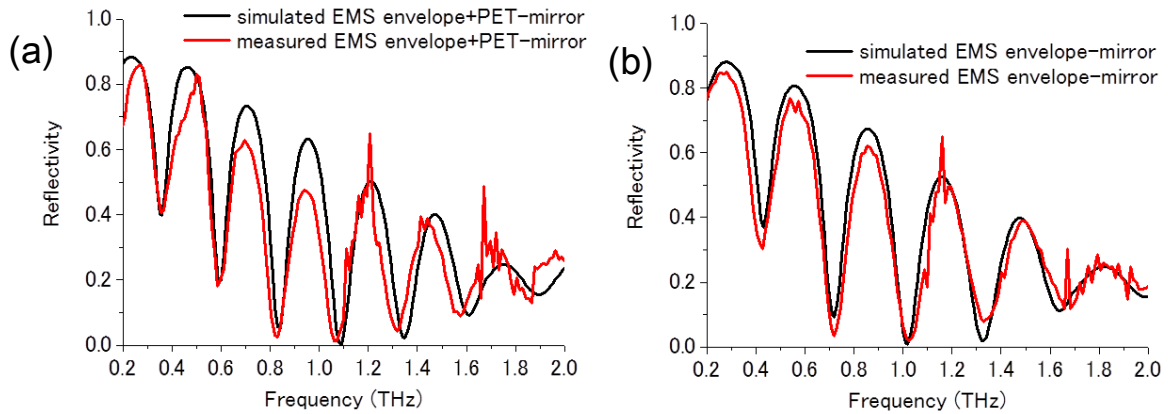


Figure 4-30. (a) A comparison of simulated and measured spectra of the PET film firmly attached to the EMS envelope (with a total thickness of 380 μm) in front of the mirror. (b) Comparison of simulated and measured spectra of the 330- μm -thick EMS envelope in front of the mirror.

Frequency range of calculation was set from 0.2 THz to 2 THz with the resolution of 10 GHz. First, we divided THz beam which has a Gaussian profile into many $100 \times 100\text{-}\mu\text{m}$ square-beam-areas (i.e., the cells used in the calculation). The dimension of THz beam depends on frequency, thus how much cells a beam can contain also depend on frequency. Next, electric field of the area inside each cell is considered flat and has its own intensity calculated from Eq. 4-9 and 4-10 using its center coordinate. Then a program was applied to consider at each cell whether THz beam inside the cell incident onto the part with or without carbon ink at a certain scanning distance of the carbon bar (i.e. spatial relation between the center of beam and the edge of carbon bar). Reflected electric field of each cell was calculated using Eq. 4-5 to 4-8 (calculation has been conducted up to 100 times of reflections). Please do notice that those cells incident to the part without ink had a big thickness d for calculation because it penetrated envelope and PET film then got reflected by mirror; d was smaller while the cell inside the area of ink as beam only penetrate envelope and got reflected directly by ink layer. Therefore, they should have different phase and amplitude term of reflected electric field. At last, whole electrical field from each cell would be added together to calculate the total reflected energy, thus the reflectivity at one such step was acquired. A figure for simple demonstration of the setup used in calculation is presented here as shown in Figure 4-31.

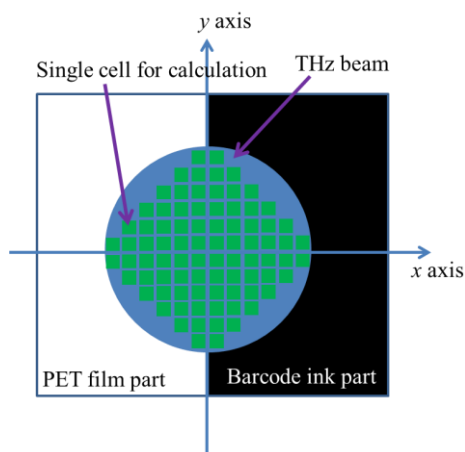
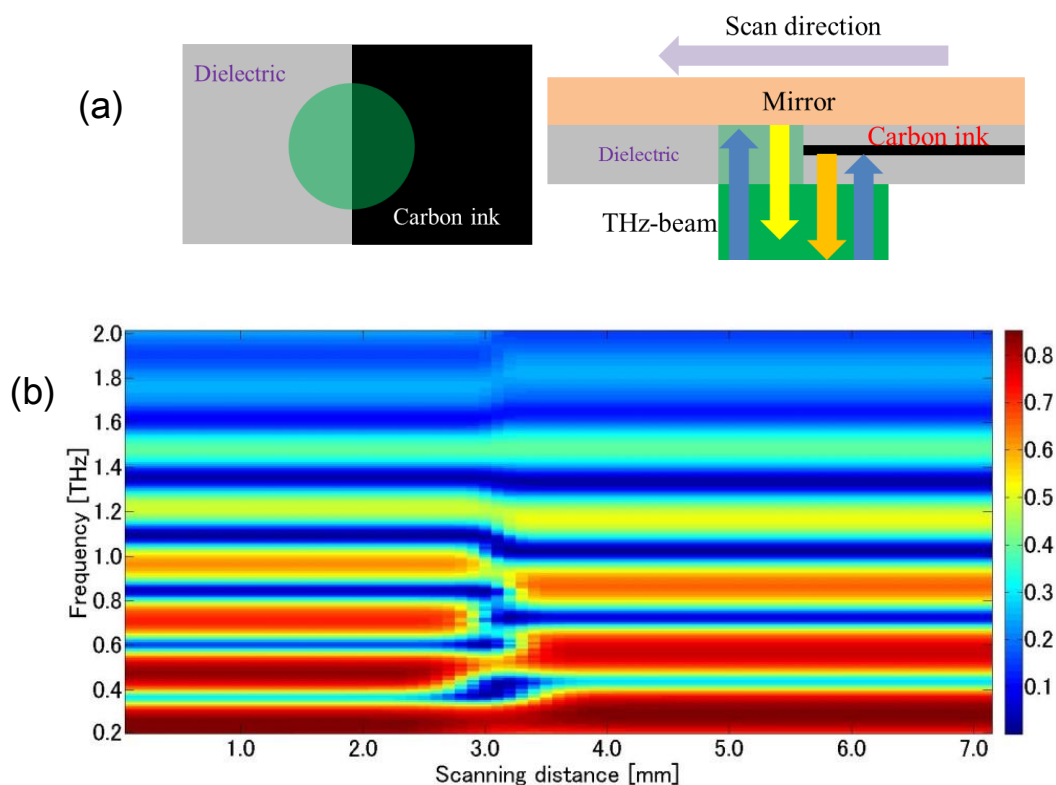


Figure 4-31. Diagram for demonstrating the simulation of beam counter to the edge of ink part

Figure 4-32 shows the simulation results together with experimentally measured data. The good agreement between the simulated and measured data supports the validity of our simplified model. We may therefore conclude that the interference patterns are predictable and controllable by carefully choosing the thickness of the two dielectric layers.



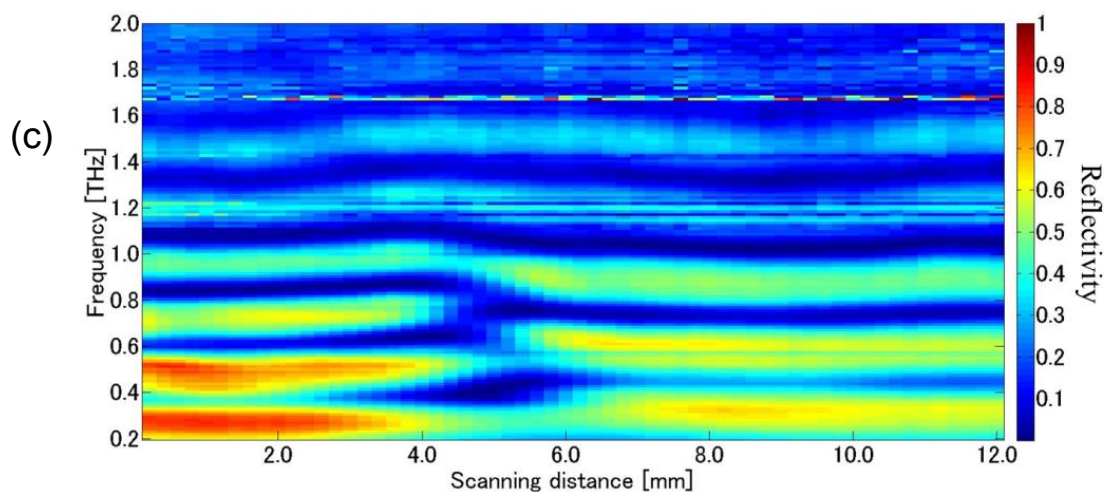


Figure 4-32. (a) The setup for investigating the reflection spectra with barcode patterns. (b) Simulated interference pattern at the edge of the barcode feature shown in (a). (c) Experimental reflection spectra scanned along the barcode feature.

4.3.6 Discussion

We have described a double-side printed THz barcode system for applications in remote identification through a covering material. Imaging experiments through a thick EMS envelope were carried out, and we described a comparison with a single-side printed THz barcode. The results showed that the double-side printed barcode provided superior spatial resolution compared with the simple barcode, even when the spot size of the incident THz beam was larger than the dimensions of the bars in the barcode pattern. With the fully printability, our proposed barcode design could be a promising alternative to achieve remote identification through obstacles at very low cost. With further optimization of the system, we expect that we will be able to achieve sufficient performance for application as a concealed label system for products and to secure information.

As we mentioned in the end of introduction part, all measurements were performed under the conditions that approximate conditions of what can be expected in the field. We believe that well-focused beam close to its diffraction-limit is not practical, because it may introduce too much trouble by well placing a product coded by concealed barcode to system's focus point as the confocal length of such system is short. Thus, the THz beam of our system was only soft focused.

We took a scan of time-pulse (around 80 ps) using THz-TDS at each point. A single

scan for time-pulse cost about 8 minutes (we used a traditional time-delay stage of THz-TDS which is time-consuming). Given our step size (0.2 mm), a measurement up to 20 mm cost over 13 hours. However, this problem of time-consuming can be solved in two aspects. First, to authors' knowledge, a fast-scan THz-TDS is commercially available with operation rates of 500 Hz at a fixed delay time of 100 ps which actually can acquire better frequency resolution compared to our THz-TDS. This commercially available system can greatly shorten the time for the imaging (100 points imaging only takes 0.2 s). The online site of the product is list can be found in reference [43]

Results shown in Figure 4-27 proof that our double-side printed barcode can operate using a THz source only generate radiation at a single frequency. Thus, it doesn't mean that a THz-TDS is necessary for implement applications in real field. Hereby, we would like to share some thoughts regarding our design's future applications in real field: the refractive index and thicknesses of an obstacle and substrate are carefully chosen and controlled. The concealed barcode formed by these two layers will be manufactured and assembled together in production process making existence of air gap as less as possible, and then sold to consumer as one. It can be attached to products as a label sheet only the information of this "label" is invisible; or in some specific cases such as mail system which a standard can be established to unify the material and thickness of packaging material. In these cases, a source is adequate with the ability of generation THz wave at certain frequency or several frequencies according to the design of our "label". Commercial available source of this kind already exist such as uni-traveling-carrier photodiode (UTC-PD) by NTT Electronics, Japan [44].

4.4 Summary

In this chapter, I explored the application of identification over obstacles using terahertz tags/barcodes. Firstly, the surface metal antenna array (metafilm) was considered for encoding the information. A "clock" shaped mode has been designed and demonstrated in the section 2, along with the measurements and simulations to support its validity. The shift of resonance frequency in spectrum could be considered in proportion to the intersection angle between two metal bars connecting outer ring and

inner circle of the “clock” shaped structure. This fact showed the simplification of our design for encoding the information. However, the high cost and inconvenience in manufacture of such metal structure held back its potential for the application. Next, a double-side printed barcode structure was proposed and measured for the applications in remote identification through a package material (EMS envelope). The favorable performance of proposed structure was acquired by comparing it to a simple single-side printed barcode using THz-TDS. With the theoretic analysis, we proved the validity of such fully printable barcode structure for the application in real field.

Reference

- [1] K. Finkenzeller, RFID handbook: Fundamentals and Applications in Contactless Smart Cards, Radio Frequency Identification and Near-Field Communication, 2010.
- [2] N. J. Woodland and B. Silver, "Classifying apparatus and method", U. S. patent 2,612,994. 1952.
- [3] M. Hara, M. Watabe, T. Nojiri, T. Nagaya, and Y. Uchiyama, "Optically readable two-dimensional code and method and apparatus using the same", U. S. Patent 5,726,435. 1998.
- [4] H. Stockman, "Communication by means of reflected power", *Proc. IRE* 36, pp. 1196-1204, 1948.
- [5] C. S. Hartmann, "A global SAW ID tag with large data capacity", *Proc. IEEE Ultrason. Symp.* vol 1, pp. 65-69, 2002.
- [6] J. McVay, A. Hoorfar, and N. Engheta, "Space-filling curve RFID tags", *Proc. IEEE Radio Wireless Symp.*, vol. 1, pp. 199-202, 2006.
- [7] S. Preradovic, I. Balbin, N. C. Karmakar, and G. F. Swiegers, "Multiresonator-based chipless RFID system for low-cost item tracking", *IEEE Transactions on Microwave Theory and Techniques*, vol. 57, no. 5, 1411-1419, 2009.
- [8] H-S. Jang, W-G. Lim, K-S. Oh, S-M. Moon, and J-W. Yu, "Design of Low-Cost Chipless System Using Printable Chipless Tag with Electromagnetic Code", *IEEE Microwave and Wireless Components Letters*, vol. 20, no. 11, pp. 640-642, 2010.
- [9] S-m. Hu, Y. Zhou, C. L. Law, and W-b. Dou, "Study of a uniplanar monopole antenna for passive chipless UWB-RFID localization system", *IEEE Transactions on Antennas and Propagation*, vol. 58, no. 2, pp. 271-278, 2010.
- [10] A. Vena, E. Perret, and S. Tedjini, "Chipless RFID tag using hybrid coding technique", *IEEE Transactions on Microwave Theory and Techniques*, vol. 59, no. 12, 3356-3364, 2011.
- [11] A. Vena, E. Perret, S. Tedjini, G. E. P. Tourtollet, A. Delattre, F. Garet, and Y. Boutant, "Design of chipless RFID tags printed on paper by flexography", *IEEE Transactions on Antennas and Propagation*, vol. 61, no. 12, pp. 5868-5877, 2013.
- [12] M. Bernier, F. Garet, E. Perret, L. Duvillaret, and S. Tedjini, "Terahertz encoding approach for secured chipless radio frequency identification", *Appl. Opt.*, vol. 50, pp. 4648-4655, 2011.

- [13] E. Perret, M. Hamdi, A. Vena, F. Garet, M. Bernier, L. Duvillaret, and S. Tedjini, "RF and THz Identification using a new generation of chipless RFID tags", *Radioengineering-Special Issue: Emerging Materials, Methods, and Technologies in Antenna & Propagation*, vol. 20, pp. 380-386, 2011.
- [14] K. Kawase, Y. Ogawa, Y. Watanabe, and H. Inoue, "Non-destructive terahertz imaging of illicit drugs using spectral fingerprints", *Optics Express*, vol. 11, issue 20, pp. 2549-2554, 2003.
- [15] D. Zimdars, J. A. Valdmanis, J. S. White, G. Stuk, S. Williamson, W. P. Winfree and E. I. Madaras, "Technology and applications of Terahertz imaging Non-Destructive Examination: Inspection of Space Shuttle Sprayed On Foam Insulation", *American Institute of Physics conference proceedings*, vol. 760, iss. 1, pp. 570-577, 2005.
- [16] Y-C. Shen and P. F. Taday, "Development and application of terahertz pulsed imaging for nondestructive inspection of pharmaceutical tablet", *IEEE Journal of Selected Topics in Quantum Electronics*, vol. 14, no.2, pp. 407-415, 2008
- [17] V. G. Veselago, "The electrodynamics of substances with simultaneously negative values of ϵ and μ ", *Sov. Phys. Usp.* 10, pp. 509-514 (1968)
- [18] D. R. Smith, Willie J. Padilla, D. C. Vier, S. C. Nemat-Nasser, and S. Schultz, "Composite Medium with Simultaneously Negative Permeability and Permittivity", *Physical Review Letters*, vol. 84, no. 18, pp. 4184-4187 (2000)
- [19] R. A. Shelby, D. R. Smith, and S. Schultz, "Experimental verification of a negative index of refraction", *Science* 292, pp. 77-79 (2001)
- [20] J. B. Pendry, "Negative refraction makes a perfect lens", *Phys. Rev. Lett.* 85, pp. 3966-3969 (2000)
- [21] N. Fang, H. Lee, C. Sun, and X. Zhang, "Sub-diffraction-limited optical imaging with a silver superlens", *Science* 308, pp. 534-537 (2005)
- [22] J. B. Pendry, D. Schurig, and D. R. Smith, "Controlling electromagnetic fields", *Science* 312, pp. 1780-1782 (2006)
- [23] D. Schurig, J. J. Mock, B. J. Justice, S. A. Cummer, J. B. Pendry, A. F. Starr, and D. R. Smith, "Metamaterial electromagnetic cloak at microwave frequencies", *Science* 314, pp. 977-980 (2006)
- [24] B. Ferguson and X.-C. Zhang, "Materials for terahertz science and technology", *Nature Mater.* 1, pp. 26-33 (2002)

- [25] J. F. O' Hara, R. Singh, I. Brener, E. Smirnova, J. Han, A. J. Taylor, and W. Zhang, "Thin-film sensing with planar terahertz metamaterials: sensitivity and limitations", *Opt. Express*, Vol. 16, Issue 3, pp. 1786-1795 (2008)
- [26] I. A. I. Al-Naib, C. Jansen, and M. Koch, "Thin-film sensing with planar asymmetric metamaterial resonators", *Appl. Phys. Lett.* Vol. 93, 083507 (2008)
- [27] H.-T. Chen, J. F. O' Hara, A. K. Azad, and A. J. Taylor, "Manipulation of terahertz radiation using metamaterials", *Laser Photonics Rev.* Vol. 5, Issue 4, pp. 513-533 (2011)
- [28] H. Tao, L. R. Chieffo, M. A. Brenckle, S. M. Siebert, M. Liu, A. C. Strikwerda, K. Fan, D. L. Kaplan, X. Zhang, R. D. Averitt, and F. G. Omenetto, "Metamaterials on Paper as a sensing platform", *Adv. Mater.* Vol. 23, Issue 28, pp. 3197-3201 (2011)
- [29] I. Al-Naib, R. Singh, C. Rockstuhl, F. Lederer, S. Delprat, D. Rocheleau, M. Chaker, T. Ozaki, and R. Morandotti, "Excitation of a high-Q subradiant resonance mode in mirrored single-gap asymmetric split ring resonator terahertz metamaterials", *Appl. Phys. Lett.* Vol. 101, 071108 (2012)
- [30] J. F. O' Hara, W. Withayachumnankul, and I. Al-Naib, "A review on thin-film sensing with terahertz waves", *Journal of Infrared, Millimeter, and Terahertz Waves*, Vol. 33, pp. 245-291 (2012)
- [31] V. A. Fedotov, M. Rose, S. L. Prosvirnin, N. Papasimakis, and N. I. Zheludev, "Sharp Trapped-Mode Resonances in Planar Metamaterials with a Broken Structural Symmetry", *Physical Review Letters*, 99, 147401 (2007)
- [32] M. D. Rotaru and J. K. Sykulski, "Improved Sensitivity of Terahertz Label Free Bio-Sensing Application Through Trapped-Mode Resonances in Planar Resonators", *IEEE Transactions on magnetics*, Vol. 47, No. 5, pp. 1026-1029 (2011)
- [33] I. A. Naib, E. Hebestreit, C. Rockstuhl, F. Lederer, D. Christodoulides, T. Ozaki, and R. Morandotti, "Conductive Coupling of Split Ring Resonators: A Path to THz Metamaterials with Ultrasharp Resonances", *Physical Review Letters*, 112, 183903 (2014)
- [34] W. J. Padilla, M. T. Aronsson, C. Highstrete, M. Lee, A. J. Taylor and R. D. Averitt, "Electrically resonant terahertz metamaterials: Theoretical and experimental investigations", *Physical Review B* 75, 041102(R) (2007)
- [35] <https://www.cst.com/>

- [36] 今井玄児, 酒井健次, “塗料の研究”, pp.150 (2008)
- [37] M. Exter, Ch. Fattinger, and D. Grischkowsky, “Terahertz time-domain spectroscopy of water vapor”, *Optics Letters*, vol. 14, no. 20, pp. 1128-1130, (1989)
- [38] G-F. Yan, A. Markov, Y. Chinifooroshan, S. M. Tripathi, W. J. Bock, and M. Skorobogatiy, “Resonant THz sensor for paper quality monitoring using THz fiber Bragg gratings”, *Optics Letters*, vol. 38, issue 13, pp. 2200-2202, (2013)
- [39] T Hattori, H Kumon, H Tamazumi, “Terahertz spectroscopic characterization of paper”, *The proceedings of Infrared Millimeter and Terahertz Waves (IRMMW-THz)*, (2010)
- [40] P. Mousavi, F. Haran, D. Jez, F. Santosa, and J. S. Dodge, “Simultaneous composition and thickness measurement of paper using terahertz time-domain spectroscopy”, *Applied Optics*, vol. 48, issue 33, pp. 6541-6546, (2009)
- [41] Y-S. Jin, G-J. Kim and S-G. Jeon, “Terahertz dielectric properties of polymers”, *Journal of the Korean Physical Society*, vol. 49, no. 2, pp. 513-517, (2006)
- [42] W. Withayachumnankul, M. Naftaly, “Fundamentals of Measurement in Terahertz Time-Domain Spectroscopy”, *Journal of Infrared, Millimeter, and Terahertz Waves*, vol. 35, issue 8, pp. 610-637, (2014)
- [43] http://dl.z-thz.com/brochures/miniz_1401_lr.pdf
- [44] <http://www.ntt-electronics.com/en/products/photonics/utc-pd.html>

Chapter 5 Terahertz interferometry by applying metal meshes

Excepting for very few research works, the metal mesh was used to be studied and applied as a filter because of its unique transmission characteristic. However, I believe that further potential of such a structure shall be discussed. One approach is already illuminated in former chapter of this thesis: a transmission sensor was designed based on the mechanism of a simple type of metal mesh with square openings arrayed on thin metal substrate. We proof that it can be successfully applied for measuring the human skin samples based on its abnormal decline in transmittance spectrums, functioning as the “probe” in frequency domain.

Another approach is that with the high reflectivity of same type of metal mesh in low THz region (a few hundred gigahertz) multiple reflections can be easily aroused in between two pieces of metal meshes or one piece of metal mesh and an aluminum plate mirror. Thus a potential interferometer is proposed. This chapter is going to introduce the basic idea of such kind of interferometric setups.

5.1 Theoretical Background

5.1.1 Multiple beam interference

Conventionally interference is a phenomenon in which two waves superimpose to form a resultant wave of greater or lower amplitude. A steady interference pattern requires these two relational waves shall share the same or nearly same frequency with certain phase separation.

Any object that is not completely opaque can be considered as an oscillator to produce steady interference pattern as long as which is irradiated by proper electromagnetic wave. As precisely uncovering information of object by analyzing its transmission or reflection fringes, our civilization has been applying interference phenomenon to sensitive examination purposes for centuries. Figure 5-1 presents a

simple diagram of how thickness and refractive index of object affect the interference pattern.

As a matter of fact, the two beam interference is only a theoretic simplified model for real interaction between coherent waves in most cases. For more practical consideration, a multiple beam interference model is necessary to be discussed. Figure 5-2 presents such an interference diagram.

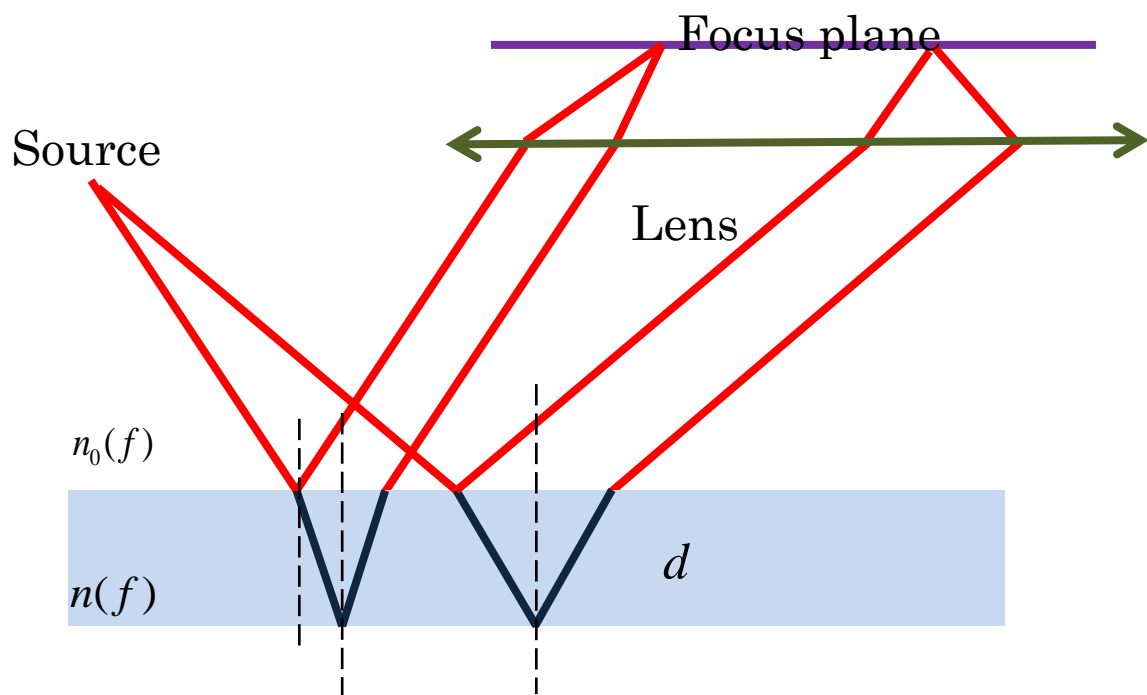


Figure 5-1. A typical two beam interference model explaining how object affects fringes

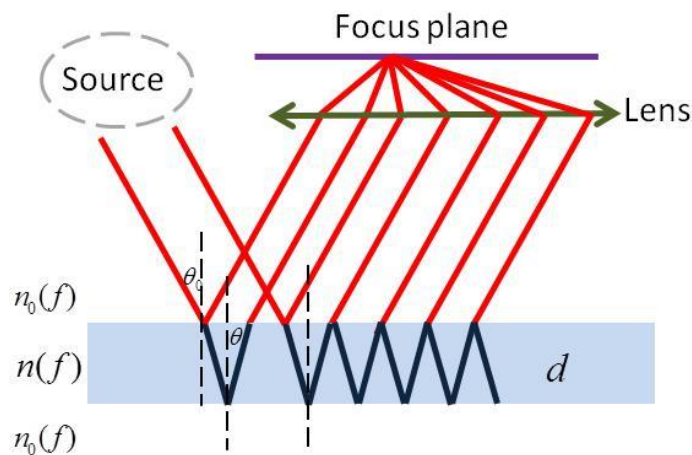


Figure 5-2. Multiple beam interference model for calculation of fringes

Considering a model displayed in Figure 5-2, the collimated beam is irradiated onto the surface of medium with the angle of incidence θ_0 . This beam refracted and reflected within the medium and the refracted angle is θ . It's not difficult to induce the formulas of reflected light and transmitted light on the case that our medium has no absorption.

We mark the reflectance from medium $n_0(f)$ to medium $n(f)$ and from medium $n(f)$ to medium $n_0(f)$ as “ r ” and “ r' ” respectively meanwhile the transmittance as “ t ” and “ t' ” in a similar way. Then we will have:

Reflected light

$$E_r = E_i[r + tt' r' e^{i\sigma} + tt'(r')^3 e^{2i\sigma} + tt'(r')^5 e^{3i\sigma} + \dots + tt'(r')^{2x-1} e^{ix\sigma} + \dots], x \geq 1, \quad (5-1)$$

Transmitted light

$$E_t = E_i tt' [1 + (r')^2 e^{i\sigma} + (r')^4 e^{2i\sigma} + (r')^6 e^{3i\sigma} + \dots + (r')^{2y} e^{iy\sigma} + \dots], y \geq 1, \quad (5-2)$$

Phase separation

$$\sigma = 2\pi \frac{\Delta L}{\lambda} = 2\pi f \frac{2n(f)d / \cos \theta - 2d \tan \theta \sin \theta_0}{c} = \frac{2\pi f}{c} 2nd \cos \theta, \quad (5-3)$$

According to “no loss assumption” and Stokes Relations, we can derive several equations as follow because wave's propagation is reversible. Reversible wave paths are shown in Figure 5-3.

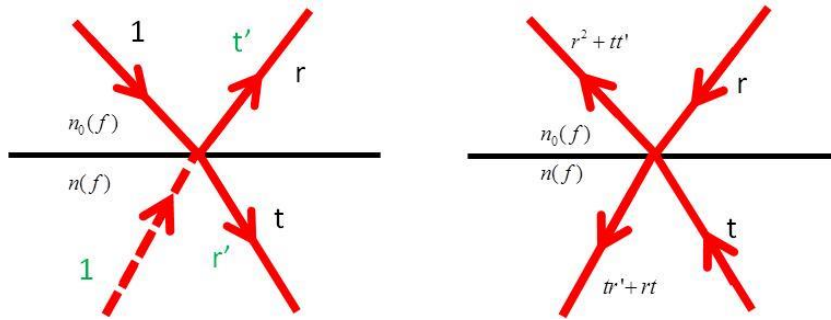


Figure 5-3. Stokes Relation is true while wave propagation is reversible

$$r^2 + tt' = 1, \quad (5-4)$$

$$tr' + tr = 1, \quad (5-5)$$

Thus, we can get

$$r = -r', \quad tt' = r^2$$

Therefore

$$R = r^2 = r'^2, T = tt', R + T = 1, \quad (5-6)$$

From formulas above, we can simplify formulas (5-1) and (5-2) as:

Reflected light

$$E_r = E_i r \left(1 - \frac{tt' e^{i\sigma}}{1 - r^2 e^{i\sigma}} \right),$$

$$E_r = E_i r \left(\frac{1 - r^2 e^{i\sigma} - tt' e^{i\sigma}}{1 - r^2 e^{i\sigma}} \right)$$

$$I_r = E_r \cdot E_r^* = E_i^2 r^2 \left(\frac{1 - e^{i\sigma}}{1 - r^2 e^{i\sigma}} \right) \left(\frac{1 - e^{-i\sigma}}{1 - r^2 e^{-i\sigma}} \right) = I_i R \frac{2(1 - \cos \sigma)}{1 + R^2 - 2R \cos \sigma},$$

$$\frac{I_r}{I_i} = \frac{4R \sin^2 \frac{\sigma}{2}}{(1 - R)^2 + 4R \sin^2 \frac{\sigma}{2}}, \quad (5-7)$$

Transmitted light

$$E_t = E_i tt' \frac{1}{1 - (r')^2 e^{i\sigma}},$$

$$\frac{I_t}{I_i} = \frac{T^2}{(1 - R)^2 + 4R \sin^2 \left(\frac{\sigma}{2} \right)}, \quad (5-8)$$

And if we let a “F” given by

$$F = \frac{4R}{(1 - R)^2},$$

Then we shall have:

$$\text{Reflectivity of the medium} = \frac{F \sin^2 \frac{\sigma}{2}}{1 + F \sin^2 \frac{\sigma}{2}},$$

$$\text{Transmittance of the medium} = \frac{1}{1 + F \sin^2 \frac{\sigma}{2}},$$

If we plot these two parameters in graph, results can be found in Figure 5-4.

From the Figure 5-4, it is easy to tell that interference fringes get sharper when the reflectance of medium get bigger (of course it's just closer to “1”, unable to surpass “1”). And along with “r” getting closer to “1” (“R” is getting closer to “1” too), F is tending to go to infinity, and makes reflectivity of the medium stays at stable value “1” (means

that influence of phase separation is greatly suppressed), which exceptions only appear when σ equal to 2π or other higher orders.

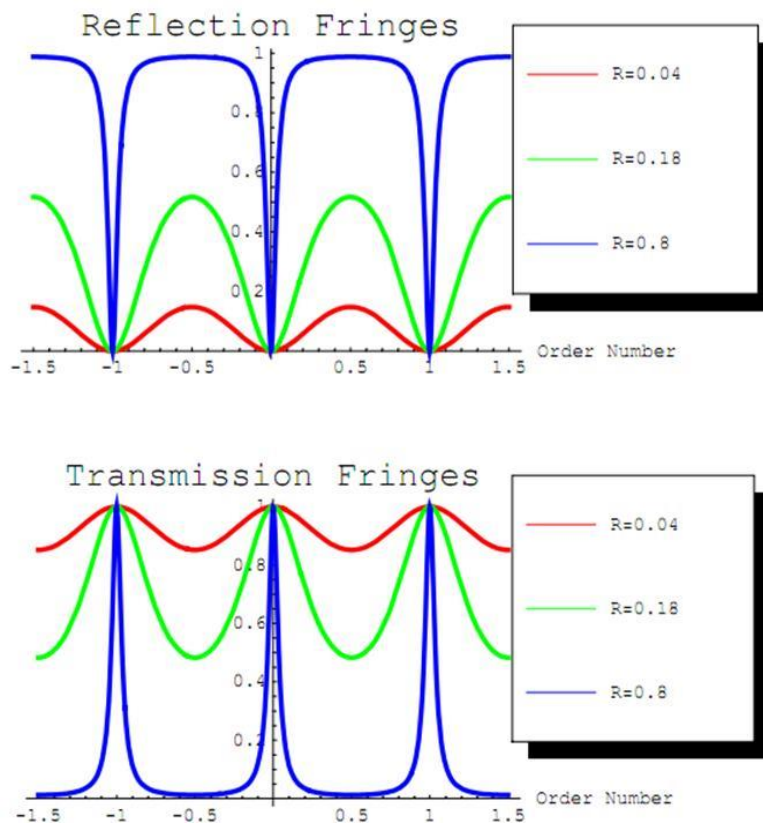


Figure 5-4. Numerical calculation results of reflectivity and transmittance of our model [1]

5.1.2 Sandwich structure of metal meshes

By using the first two THz-TDS setups with reflection geometry mentioned in Chapter 2 - Section 2.1.4, the reflectivity of metal mesh was acquired. Changing the angle between mesh grid and the polarization direction of incident beam, the appearance of reflectivity peak around 960 GHz which is complementary to “dip” in transmittance spectrum was confirmed too. Results can be found in Figure 5-5. The factor that peak is not as sharp as “dip” mentioned in Chapter 3 can be explained as which metal mesh was irradiated by focused THz beam at a glancing incident angle in our THz-TDS with reflection geometry.

High reflectivity in a few hundred GHz (lower around than 0.8 THz) is confirmed. Thus we can expect a sharp resonance in this frequency region by applying metal mesh for interferometer.

Considering the convenience of setting samples, we choose the setup of THz-TDS with reflection geometry for the measurements. Figure 5-6 shows the sandwich structure allowing THz beam to be irradiated and reflected in vertical axis.

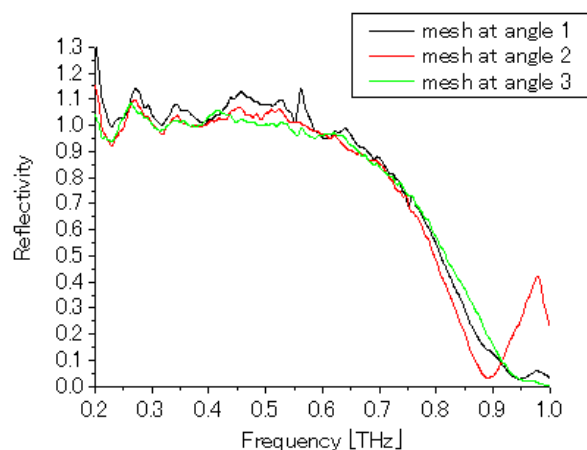


Figure 5-5. The reflectivity of metal mesh measured by THz-TDS with reflection geometry

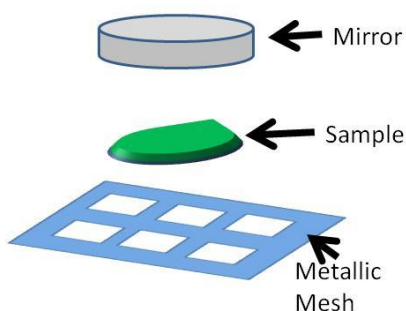
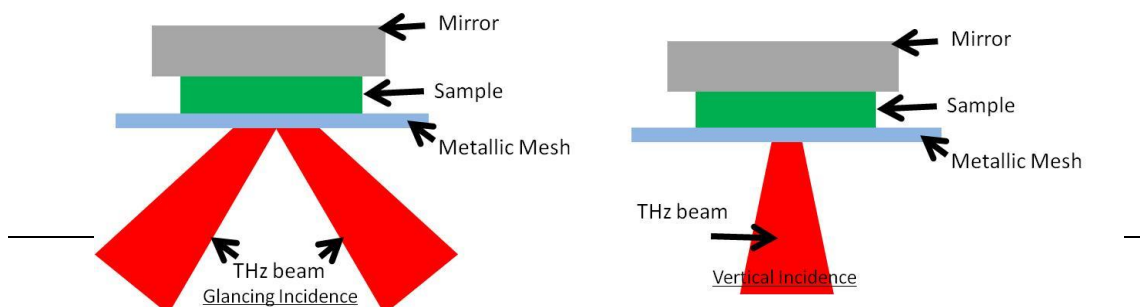


Figure 5-6. The sandwich structure of metal mesh interferometric sensor

We possess two functional THz-TDS with reflection geometry. The THz beam irradiated onto samples is focused in both of these two setups, while the incident angle is different between them as mentioned in Chapter 2. To evaluate both systems for reference, a known quartz sheet (thickness of 100 μm) was measured. Results can be found in Figure 5-7.



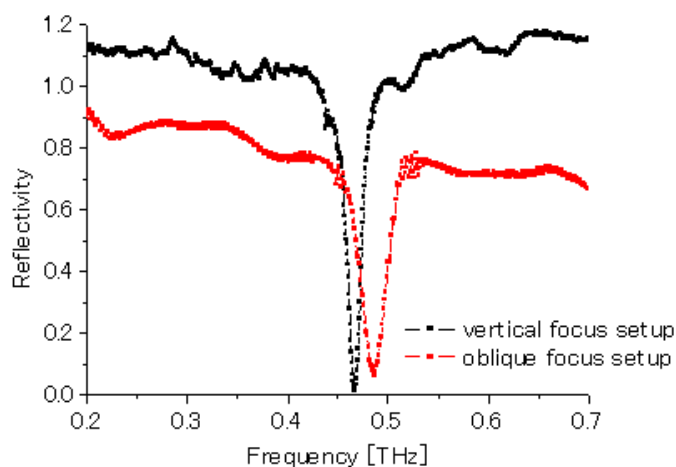


Figure 5-7. Evaluation of two THz-TDS with glancing incident beam and vertical incident beam by the measurement of quartz sheet

It's clear in Figure 5-7 that interference fringe is much sharper in the setup with THz beam vertically focused onto sample, which makes our vertical focus THz-TDS setup a better choice for the interference sensing measurements. However at the time the following study was conducted, the building of vertical focus setup was not complete yet. It still needs more adjustment for raising the SNR. Thus the measurements in following section were carried out by using obliquely focused THz-TDS setup.

5.2 Metal mesh interferometer measurements using THz-TDS

A few measurements have been carried out for roughly testing our interferometric sensor. According to the metal mesh reflection property as shown in Figure 5-5, this interferometric shall gain its best sensitivity under about 800 GHz. As mentioned in Formula (5-3), the thickness and refractive index of sample decide how many orders of interference fringe can be located in the region under 800 GHz. An example shown in Figure 5-8 is the measurement of a piece of paper with a square cut in middle.

The thickness of paper is 0.5 mm, and the square size is bigger than the diameter of THz beam, so that we could consider true material aroused interference was air. Moreover, it is easy to understand that it would be impossible to change the sample

without moving the mirror on top. So the effect of such replacement was also inspected. Result can be found in Figure 5-9.

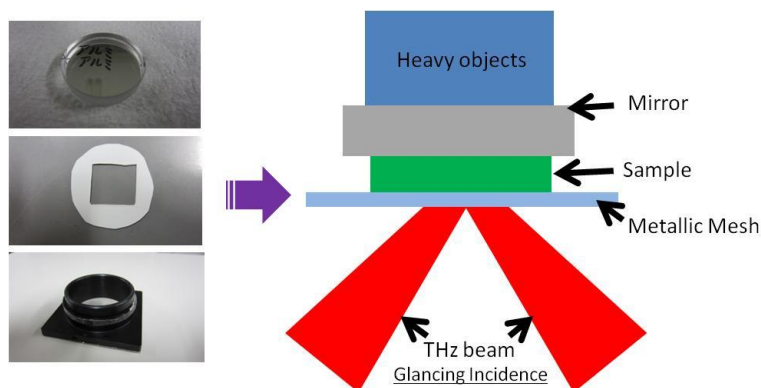


Figure 5-8. Sandwich structure of our interferometric sensor.

The heavy objects above the mirror was used to press the sample to make it flat

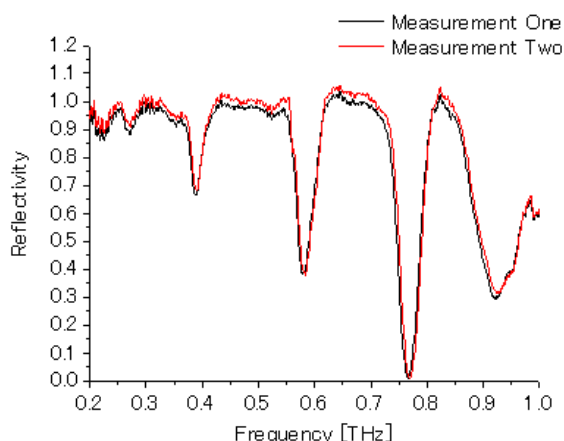


Figure 5-9. Results of hollow paper measurements

After the “measurement one”, we took out the paper by removing the mirror on top and then re-set it again. “Measurement two” was carried out to confirm the stability of such replacing action. Every order of interference fringe fits to each other nicely, meaning we acquire a good reliability of interference pattern.

Because some of the samples are quite thin or hard to be measured alone, Polypropylene Film (PP Film) as a substrate was introduced. The reference of a PP Film with the thickness of 200 μm can be found in Figure 5-10.

One factor in Figure 5-10 that should be cleared: the “dip” around 550 GHz doesn’t belong to any order of interference. It is caused by water absorption in

THz-TDS as mentioned in Chapter 2. A measurement has been carried out to support this explanation shown in Figure 5-11.

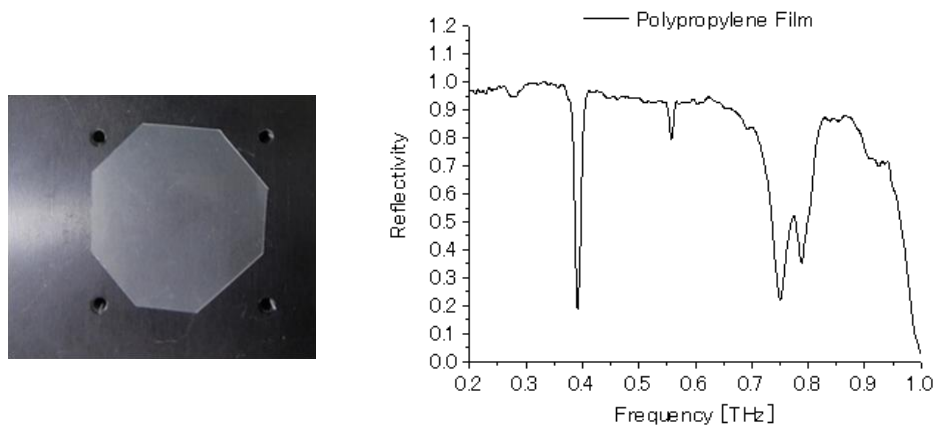


Figure 5-10. Reference fringes of PP Film with the thickness of 200 μm

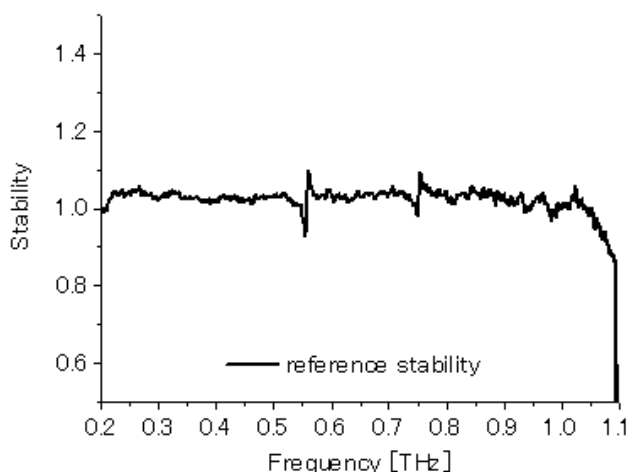


Figure 5-11. The inspection of how water absorption affect our THz-TDS with reflection geometry

This figure was acquired in the way of dividing one reference output line by another which was obtained at a different time. Water absorption lines can be observed at both around 550 and 750 GHz if we only consider the frequency lower than 1 THz.

One group of common paper (thickness is 0.095 mm) printed with different level of gray scale was measured by attach them onto the PP Film. The purpose was to check that if the tiny difference of ink thickness or density can be distinguished by our sensor. The results are shown in Figure 5-12.

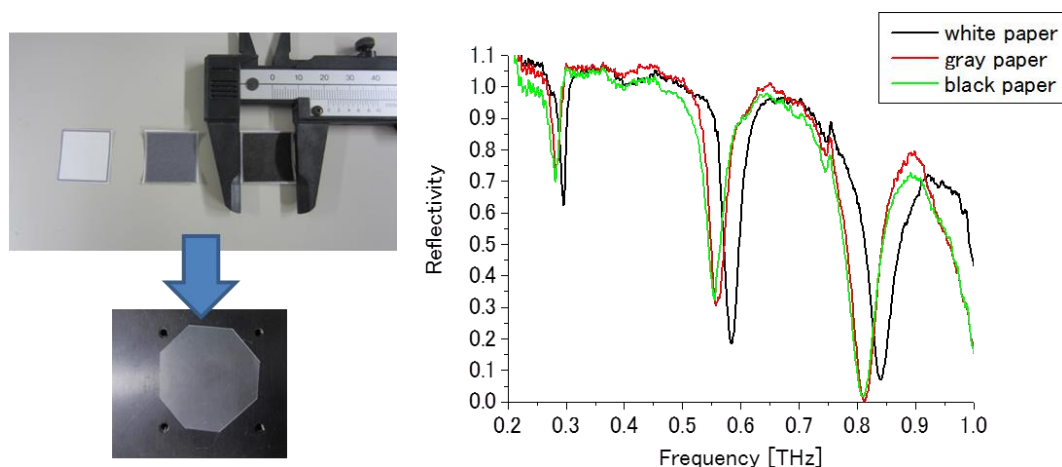


Figure 5-12. Measurement of common paper with different gray scales

The small absorption line around 750 GHz was confirmed. From this figure, we can tell that our interferometer is possible to discover the tiny difference of ink thickness which implies that our interferometric sensor has a good sensitivity.

We started to consider the feasibility of applying this approach for the bio-relevant applications. Firstly we measured the stratum corneum samples acquired by tape stripping method from forehead and arm skin. Results can be found in Figure 5-13.

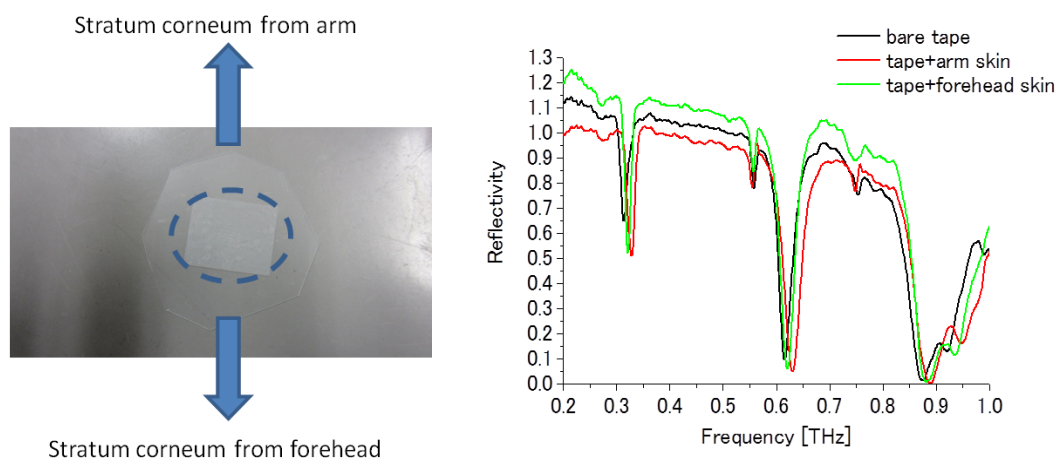


Figure 5-13. Measurements of skin sample from forehead and arm

The results in Figure 5-13 revealed a very strange phenomenon that the interference fringes shifted to high frequency as the stratum corneum samples were attached. These were opposite to what we have expected that the frequency would be

decreased while the thickness of medium was getting enlarged according to the formula (5-3). We don't have answer to this phenomenon yet, it requires further attention of more experiments with quantitative samples.

For the next step, we measured the spectrums of human fingerprint left on PP film. Results can be found in Figure 5-14.

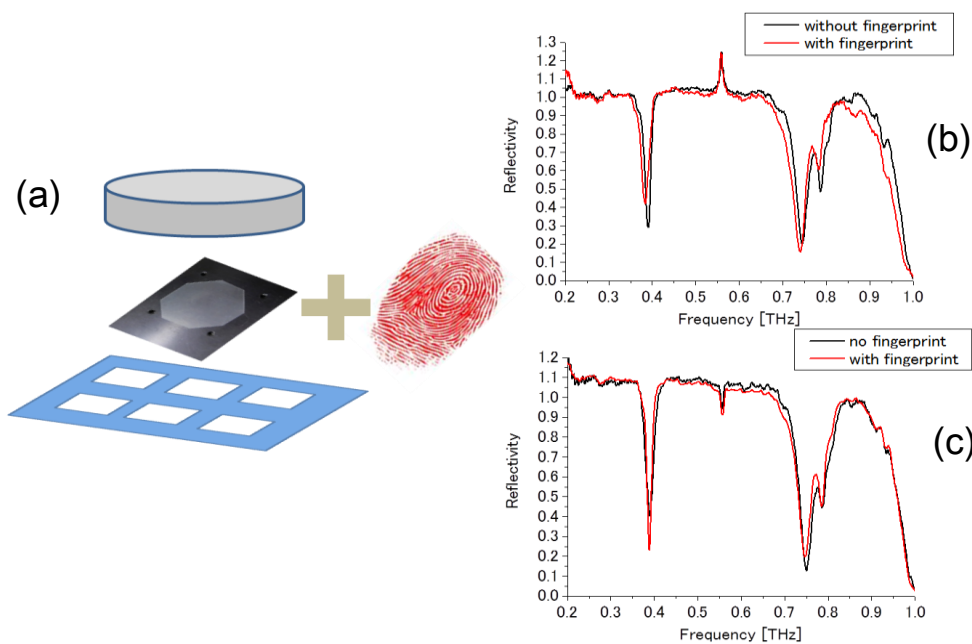


Figure 5-14. (a) Setup of measurements of fingerprint left on PP Film.

(b) Measurements results of fingerprint using our THz interferometer on day one

(c) Measurements results of fingerprint using our THz interferometer on day two

The measurements have been done twice on different days with the same PP Film as the substrate. At the beginning of experiment, the PP Film was washed by pure water carefully under the condition of both operating hands with rubber gloves on. After the reference curves were acquired (black lines in Figure 5-14(b, c)), a subject was asked to leave a complete fingerprint of his thumb onto the PP Film. Red lines in Figure 5-14 (b, c) was the result of PP Film with fingerprint. The biggest variation of fringes is no more than 7GHz (Figure 5-14 (b) at around 750 GHz), and some order of interference have no shift at all. These ambiguous results suggested that the sensitivity of our THz interferometer at present has difficulty detecting small amount of residual contained in human's fingerprint. It needs quantitative discussion later on with more experiments.

5.3 Summary

In this chapter, a new THz interferometric sensor working in the frequency band under 1 THz was proposed. A sandwich structure was chosen and proved to be reliable to form such an interferometer by the measurements of quartz. Then a few samples including PP films, fingerprint and stratum corneum stripped by tape were measured too. The experimental results suggested that the proposed sensor has the potential to be a sensitive approach for THz sensing applications. For the measurements of stratum corneum and fingerprint, more work needs to be conducted with the quantitatively defined samples.

Reference

- [1] James C. Wyan, “Multiple Beam Interference”, Chapter 7, Page 4, Opticas 505. Diffraction and Interferometry, College of Optical Sciences, the University of Arizona (2007)

Chapter 6 Summary

The research work of exploring the potential applications for terahertz radiation using metal structures, including the terahertz component analysis and terahertz identification over obstacles were presented in this paper. Measurements and their corresponding theoretic calculations were conducted and discussed to support the validity of those works. Author sincerely wishes later researchers can achieve the success and reveal the great potential of terahertz radiation.

Chapter 2 presented the experimental setup used for measurements introduced in later chapters. THz-TDS is a well-developed and widely applied approach in the terahertz research field all over the world. The work that author have contributed were mainly achieved by THz-TDS. Next, the study of cross-polarization effect of the parabolic mirror was presented. Due to the popularity of the parabolic mirror as an optical element in many experimental setups, it was urgent to aware researchers in terahertz field the imperfectness of parabolic mirror. Both theoretical calculation and measurements were conducted with their results presented in this chapter, to demonstrate the cross-polarization effect it can apply to the electromagnetic field. Advices were provided for restraining it to minim level.

Chapter 3 firstly presented the image of metal mesh that we were using, and then reports the incident angle dependence as well as polarization dependence of the abnormal decline band distinguished as “dip” in its transmission spectrum. Several theoretic hypothesis including Surface Plasmon Polariton (SPP), and the Composite Diffracted Evanescent Wave theory, that trying to explain the transmission property of metal mesh were introduced. Although there was no decisive conclusion to the explanation of transmission property especially the appearance of dip frequency, we believed that the diffracted evanescent wave theory holds the key to the answer of this task. Next, a series of measurements of human skin (stratum corneum) by applying a THz sensing method using metal mesh were introduced. We confirmed that variation of lipid content in stratum corneum sample can be observed sensitively. The protein denaturation is also traceable by using our THz sensor. As a result, we can say that our

THz sensing method using metal mesh is a practicable and sensitive spectral analysis for human skin measurements, which may leads to many bio-relevant applications.

Chapter 4 explored the application of identification over obstacles using terahertz tags/barcodes. Firstly, the surface metal antenna array (metafilm) was considered for encoding the information. A “clock” shaped mode has been designed and demonstrated in the section 2, along with the measurements and simulations to support its validity. The shift of resonance frequency in spectrum could be considered in proportion to the intersection angle between two metal bars connecting outer ring and inner circle of the “clock” shaped structure. This fact showed the simplification of our design for encoding the information. However, the high cost and inconvenience in manufacture of such metal structure hold back its potential for the application. Next, a double-side printed barcode structure was proposed and measured for the applications in remote identification through a package material (EMS envelope). The favorable performance of proposed structure was acquired by comparing it to a simple single-side printed barcode using THz-TDS. With the theoretic analysis, we proved the validity of such fully printable barcode structure for the application in real field.

Chapter 5 proposed a new THz interferometric sensor working in the frequency band under 1 THz. A sandwich structure was chosen and proved to be reliable to form such an interferometer by the measurements of quartz. Then a few samples including PP films, fingerprint and stratum corneum stripped by tape were measured too. The experimental results suggest that the proposed sensor has the potential to be a sensitive approach for THz sensing applications. For the measurements of stratum corneum and fingerprint, more work need to be repeated with the quantitatively defined samples.

Presentation and Publication

• Original Paper

- [1] Yu Guan, Koji Mizukoshi, Koji Suizu and Kodo Kawase, "THz techniques for human skin measurement", Proceedings of SPIE, Optical Interactions with Tissue and Cells XXII, Vol. 7897, 78970D, pp. 1-6, 2011.
- [2] Yu Guan, Koji Mizukoshi, Kazuki Yonekura, Kei Takeya and Kodo Kawase, "THz techniques using metal mesh sensor for human skin measurement", Terahertz Science and Technology, Vol.4, No.3, 128-131, 2011
- [3] Koji Mizukoshi, Kazuki Yonekura, Hidehiro Ogura, Yu Guan and Kodo Kawase, "Terahertz wave techniques using a metal mesh for evaluating the components of the stratum corneum", Skin Research and Technology, Vol. 19, Issue 1, pp. e383-e389, 2013
- [4] Yu Guan, Manabu Yamamoto, Toshiyuki Kitazawa, Saroj R. Tripathi, Kei Takeya & Kodo Kawase, "A Concealed Barcode Identification System Using Terahertz Time-domain Spectroscopy", Journal of Infrared, Millimeter, and Terahertz Waves, Vol. 36, No. 3, pp. 298-311 (2015)

• Presentation at International Conference

- [1] Y. Guan, K. Mizukoshi, K. Suizu, and K. Kawase, "THz techniques for human skin measurement", SPIE 2011 Photonics West, Optical Interactions with Tissue and Cells XXII, January 21-26, San Francisco, California (USA), (2011).
- [2] Y. Guan, K. Mizukoshi, K. Suizu, K. Kawase, "THz techniques using metal mesh sensor for human skin measurement", Microwave/Terahertz Science and Applications (MTSA 2011), P-30 (Poster Session), June 19-22, Nanjing University, Nanjing (China), (2011)
- [3] Y. Guan, M. Yamamoto, T. Kitazawa, S. R. Tripathi, K. Takeya and K. Kawase, "Development of THz barcode for security applications", Mar. 8-13, Optical Terahertz Science & Technology Conference, San Diego (USA), (2015)

- [4] H. Okano, T. Minami, Y. Guan, S. R. Tripathi, K. Takeya, M. Tani and Kodo Kawase, “High power Cherenkov phase-matched terahertz wave generation from a LiNbO₃ ridge waveguide”, Mar. 8-13, Optical Terahertz Science & Technology Conference, San Diego (USA), (2015)

• **Presentation at Domestic Conference**

- [1] 管宇, 水越興治, 米倉和輝, 竹家啓, 川瀬晃道, “メタルメッシュセンサを用いたテラヘルツ波分光による皮膚計測に関する研究”, 第 72 回応用物理学学会学術講演会, 1p-B-7, 山形大学, August, 2011
- [2] Yu Guan, Shu-zhen Fan, Kei Takeya, Kodo Kawase, "Study of beam polarization rotation affected by parabolic mirrors in THz spectroscopic setup", 応用物理学学会テラヘルツ電磁波技術研究主催・研究討論会「テラヘルツセンシング及びシミュレーション技術の進展」, 東京, Mar. 4, 2013
- [3] 管宇, “Study of polarization for THz engineering”, 日本学術会議第 3 回先端フォトニクス, 東京, Apr. 26, 2013
- [4] Yu Guan, Shu-zhen Fan, Kei Takeya, and Kodo Kawase, “Study of cross polarization effect of parabolic mirrors in THz spectroscopic setup”, テラヘルツ秋の学校 2013, 仙台, Nov. 21, 2013

• **Award**

- [1] Yu Guan, Koji Mizukoshi, Kei Takeya, and Kodo Kawase, “THz techniques using metal mesh sensor for human skin measurement”, Microwave/Terahertz Science and Applications (MTSA 2011), Best Poster Award, June 19–22 (2011).

Acknowledgment

This research work was carried out at Kawase Laboratory, Graduate school of Engineering, Nagoya University, with great help and kindness from many staff and friends. Hereby I would like to give them my sincerely gratitude.

Attracted by the interesting research undergoing at Prof. Kawase's group in THz science and technology, I decided to come to Nagoya University for seeking of master and doctor degree as an international student in the year of 2009. And it's proud to say that I had the honor to be accepted by Prof. Kawase to join his laboratory as I have wished. Prof. Kawase has been a wonderful seniority and guider to lead me entering the field of science. I shall always show my gratitude and respect to him for his encouragement and kind consideration. Additionally, I also would like to thank three reviewers for this thesis: Prof. Nakazato, Prof. Nishizawa, and Associate Prof. Ogawa for their precious comments and kind help.

The elder students in Kawase Laboratory have lent the helping hand to me in need. Especially I would like to mention Ms. Iwasaki as my tutor and Mr. Nakagomi for his introducing of metal mesh research. I can't count how many times that the present students of Kawase Laboratory has shown their generosity to me. I shall give you all my heartfelt thanks. And since the beginning of my master course, I am so lucky to have Mr. Ogura, Mr. Katori, Mr. Hayashi and Mr. Fujida for such fullness of two years. Additionally, I would like to thank Miss. Okano and our secretary Ms. Ito in our lab for their enthusiastic support. This research couldn't be carried out without those valued assistance from all staffs and students in Kawase Lab. I am very sincerely grateful to the help of Associate Prof. Suizu, Assistant Prof. Takeya, and Dr. Tripathi, Dr. Fan, Dr. Smirnova, Dr. Ishai, and Mr. Yamazaki for their selfless guiding and treasured time. And also I would like to appreciate the wonderful discussion by graduated students: Mr. Odamura, Mr. Taira, Mr. Seto; master course's students: Mr. Murate, Mr. Miyada, Mr. Imayama, Mr. Minami, Mr. Takahashi and junior students: Mr. Kitazawa, Mr. Sugiyama, Mr. Kato. Additionally, I also want to thank the researchers Mr. Mizukoshi, Mr. Yonekura from POLA Chemical Industries, Inc. and Mr. Yamamoto from DNP. Co. Ltd. At last, I shall give my great respect to my parents living in China for their continuous encouragement and mental support. May I will never let them down.